NAS CR 121001

TRW ER-7592

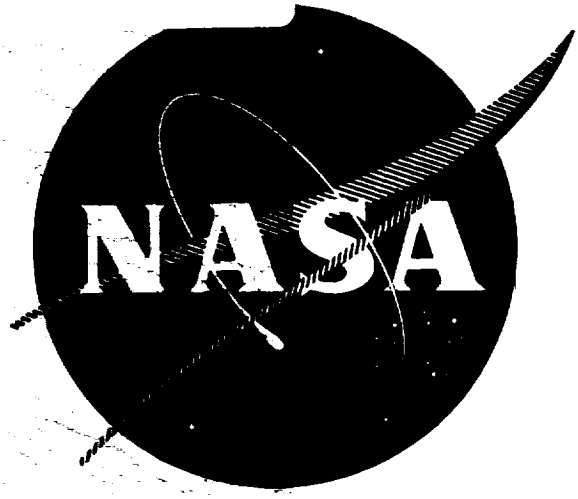

INFLUENCE OF CREEP DAMAGE ON THE LOW CYCLE THERMAL-MECHANICAL FATIGUE BEHAVIOR OF TWO TANTALUM-BASE ALLOYS

FINAL REPORT

Prepared for

NATIONAL AERONAUTICS AND SPACE ADMINISTRATION
LEWIS RESEARCH CENTER
UNDER CONTRACT NAS 3-13228

TRW MATERIALS TECHNOLOGY LABORATORIES
CLEVELAND, OHIO

Request for copies of this report should be referred to

National Aeronautics and Space Administration
Office of Scientific and Technical Information
Attention: AFSS-A
Washington, D. C. 20546

TRW ER-7592

NASA-CR-121001

FINAL REPORT

CONTRACT NAS-3-13228

3 July 1969 to 2 April 1972

INFLUENCE OF CREEP DAMAGE ON THE LOW CYCLE THERMAL-MECHANICAL FATIGUE BEHAVIOR OF TWO TANTALUM BASE ALLOYS

K. D. Sheffler
G. S. Doble

1 May 1972

Technical Management:

P. E. Moorhead
A. J. Nachtigall
National Aeronautics and Space Administration
Lewis Research Center
Materials and Structures Division

Materials Technology Laboratory
TRW Equipment
23555 Euclid Avenue
Cleveland, Ohio 44117

FOREWORD

The work described in this report was performed in the Materials Technology Laboratory of TRW Inc. under the sponsorship of the National Aeronautics and Space Administration, Contract NAS-3-13228. The purpose of the study was to obtain low cycle thermal fatigue life data on refractory alloys for use in designing space electric power systems. The program was administered for TRW Inc. by Dr. E. A. Steigerwald and Mr. J. A. Alexander, Program Managers. The principal investigators were Dr. K. D. Sheffler and Dr. G. S. Doble, with technical assistance provided by Mr. J. W. Sweeney. The NASA Technical Managers were Mr. P. E. Moorhead and Mr. A. J. Nachtigall of the Materials and Structures Division.

Prepared by: K. D. Sheffler
K. D. Sheffler
Principal Engineer

G. S. Doble
Principal Engineer

Reviewed by: H. E. Collins
H. E. Collins
Principal Engineer

Approved by: John A. Alexander
J. A. Alexander
Manager
Materials Research Department

ABSTRACT

Low cycle fatigue tests have been performed on the tantalum base alloys T-111 and ASTAR 811C with synchronized, independently programmed temperature and strain cycling. The thermal-mechanical cycles applied fell into three basic categories: these were isothermal cycling, in-phase thermal cycling, and out-of-phase thermal cycling. In-phase cycling was defined as tensile deformation associated with high temperature and compressive deformation with low temperature, while out-of-phase thermal cycling was defined as the reverse case. The in-phase thermal cycling had a pronounced detrimental influence on the fatigue life of both alloys, with the life reduction being greater in the solid solution strengthened T-111 alloy than in the carbide strengthened ASTAR 811C alloy. As an example of this effect, tests conducted on T-111 alloy at a total diametral mechanical strain range of 0.8% showed a fatigue life of 796 cycles when tested isothermally at 2100°F (1422°K), as compared to a life of only 35 cycles when the temperature was cycled from 2100°F to 400°F (1422/478°K) in-phase with the mechanical strain (heating with tension, cooling with compression). The out-of-phase tests also showed pronounced effects on the fatigue life of both alloys, although not so dramatic as the first example. Metallographic examination of tested samples showed that the in-phase life reduction was caused by massive grain boundary decohesion which resulted from unreversed grain boundary sliding in the tensile half of the thermal-mechanical fatigue cycle. The out-of-phase life changes were found to be associated with geometric instabilities developed in the hourglass test specimens. The results of this study were significant because they showed that the mechanism for thermal-cycled life reductions was a general one which may be found in other high temperature materials such as iron and nickel-base superalloys.

TABLE OF CONTENTS

TABLE OF CONTENTS (continued)

SUMMARY

The low cycle fatigue resistance of the two tantalum alloys T-111 (Ta-9%W-2%Re) and ASTAR 811C (Ta-8%W-1%Re-0.7%Hf-0.025%C) has been evaluated using completely reversed diametral strain controlled push-pull fatigue tests performed on hourglass specimens heated by direct resistance. Tests were conducted with twelve specific synchronized, independently programmed temperature and strain cycles which fell into three basic categories depending on the phasing of the temperature and strain. The first category was isothermal cycling, while the second and third basic cycle types involved in-phase and out-of-phase thermal cycling. In-phase cycling was defined as tension associated with high temperature and compression with low temperature, while out-of-phase cycling was the reverse case.

The in-phase thermal cycling caused a severe reduction of fatigue life for both materials with respect to isothermal cycling at the peak temperature of the thermal cycle. The life reduction was greater in the solid solution strengthened T-111 alloy than in the carbide strengthened ASTAR 811C alloy. Metallographic examination of the tested samples showed that the cause of the in-phase life reduction was massive grain boundary decohesion which resulted from the occurrence of tensile grain boundary sliding at high temperature that was not reversed by cold plastic flow in the compressive (low temperature) half cycle. The ASTAR 811C was less susceptable to this effect because of the presence of a grain boundary carbide precipitate which reduced the rate of grain boundary sliding in this material.

The out-of-phase thermal cycling caused both decreases and increases in fatigue life with respect to isothermal cycling, depending on the test material and the strain amplitude. For the ASTAR 811C alloy the out-of-phase results were consistently below the isothermal data, while in the T-111 alloy the out-of-phase lives were above the isothermal results at low strain amplitudes and below them at higher strains. The out-of-phase life variations were found to be associated with geometric instabilities associated with the hourglass specimen configuration rather than with microstructural damage.

The fatigue results from the ASTAR 811C alloy were analyzed by the method of partitioned strain ranges. Predictions made by this method showed excellent agreement with experimental results for the out-of-phase cycled tests, with the agreement being somewhat poorer for the in-phase results.

The results of this program are significant because they indicate that the observed thermal cycled life reduction may be a general effect applicable to all high temperature materials. The controlling mechanism for this effect was shown to be unreversed grain boundary sliding, which was not associated with any unique property of the tantalum alloys, and would occur in any material where the service temperature is cycled through the equicohesive temperature in-phase with a mechanical strain. Significant fatigue life reductions may thus be anticipated in any material which is exposed to this type of thermal fatigue cycling.

I INTRODUCTION

Thermal fatigue is a primary mode of failure in components and structures such as gas turbine vanes, steam piping, nuclear pressure vessels, multiple firing rocket engines, and power generating systems. An analysis of material requirements for a specific application is difficult because service conditions involve an elastic-plastic response to stress and appreciable creep deformation. This material response is usually determined by a complex time-stress-temperature history plus transient, non-uniform temperature and stress profiles imposed by the heating and geometry of the structure. Analysis is also complicated by the metallurgical characteristics of a real alloy which may be anisotropic, and have a structure which may be altered by exposure to service temperatures.

Although the most reliable method of establishing thermal fatigue behavior is service testing of the structure this approach is extremely expensive and time consuming. A need exists to develop improved laboratory or simple simulated component tests along with meaningful methods of analysis which will allow laboratory results to be used to predict more complex component performance.

The proposed use of the tantalum base alloys T-111 (Ta-8%W-2%Hf) and ASTAR 811C (Ta-8%W-1%Re-0.7%Hf-0.025%C) in space electric power systems has generated a need for thermal fatigue data on these materials in a hard vacuum environment. The present study was therefore undertaken to characterize the thermal fatigue behavior of T-111 and ASTAR 811C in vacuum using independently programmed strain and temperature cycles in the range of 400 to 2100°F (478 to 1422°K).

The program was performed in three phases. The first phase involved the procurement and characterization of test materials. The second phase comprised the design and construction of a low cycle thermal fatigue apparatus capable of testing with synchronized independently programmable temperature and strain cycles in an ultrahigh vacuum environment of less than 1×10^{-7} torr. The third phase involved the actual fatigue testing of the T-111 and ASTAR 811C alloys. The following final report will provide a detailed description of each of these three phases of this program.

II PHASE I - PROCUREMENT AND CHARACTERIZATION OF TEST MATERIALS

The two alloys evaluated, T-111 and ASTAR 811C, were obtained in the form of 0.65 inch thick plate cold rolled and recrystallized 1 hour at 3000°F (1922°K). Scanning electron micrographs of both materials in the as-received condition are shown in Figures 1 and 2. Chemical analyses are presented in Table 1. While these two alloys are similar in composition, the high temperature strengthening mechanisms differ in that T-111 is a single phase solid solution strengthened alloy, while ASTAR 811C is strengthened by a combination of solid solution and precipitation hardening, the latter provided by the tantalum carbide precipitate which is clearly visible in Figure 2. Both alloys recrystallized at about 2600°F (1700°K) and were tested in the recrystallized condition, thereby providing a metallurgically stable structure in the anticipated range of service temperatures. Because of the relatively low homologous temperatures involved (~0.44 at 2100°F) (1422°K), creep effects were anticipated only near the upper end of the service temperature cycle. Previous work has shown that both test materials exhibit creep at temperatures as low as 1500°F (1089°K); however, because of the added carbide strengthening, creep effects at this temperature are less significant in the ASTAR 811C than in the T-111 alloy (1,2).

Thermal expansion, elastic modulus, and Poisson's ratio were measured for each material to provide data for the separation of elastic and plastic longitudinal and diametral strain components, while elevated temperature tensile properties were obtained for analysis of the thermal fatigue results by the method of universal slopes (3). Thermal expansion, elastic modulus, and Poisson's ratio measurements were conducted at temperatures between ambient and 2600°F (1700°K) in a 10^{-8} torr vacuum furnace equipped with a tungsten mesh resistance heating element. Thermal expansion measurements were made at 200F° (111K°) intervals on a specimen having a 2" (5.1 cm) gauge length using an optical cathetometer having a precision of ±50 μ-inch (±1.27 microns) Both longitudinal and shear modulus (E and G) were determined by a pulse-echo technique in which the transit time of an extensional or torsional elastic wave was measured in a 1/4 inch (6.35 mm) diameter rod of known length ℓ and density ρ. A commercial system, the Panatherm Model 5010, manufactured by Parametrics Inc., was used for these measurements. The system consisted of a standard longitudinal and custom made shear transducer for generating and detecting the elastic wave, together with the electronics required for measurement and display of the transit time t on a digital readout. The elastic modulii were calculated from this information using the formulae

$$\text{wave velocity} = \sqrt{\frac{\text{modulus}}{\text{density}}}$$

or

$$\text{modulus} = \frac{4\ell^2}{t^2}\rho$$

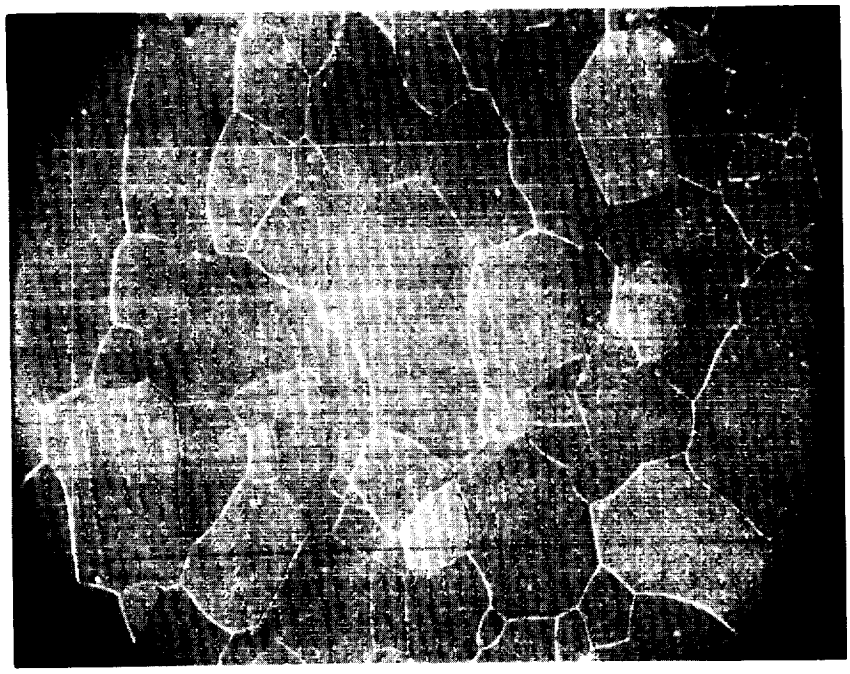

(a) 500X

(b) 2000X

Figure 1. Microstructure of T-111 alloy annealed 1 hour at 3000°F (1922°K).

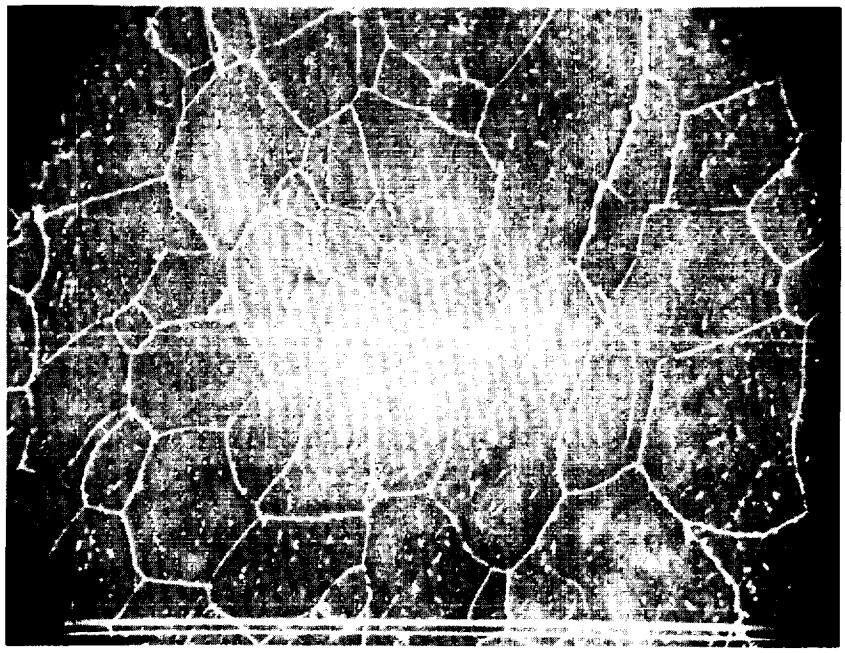

(a) 500X

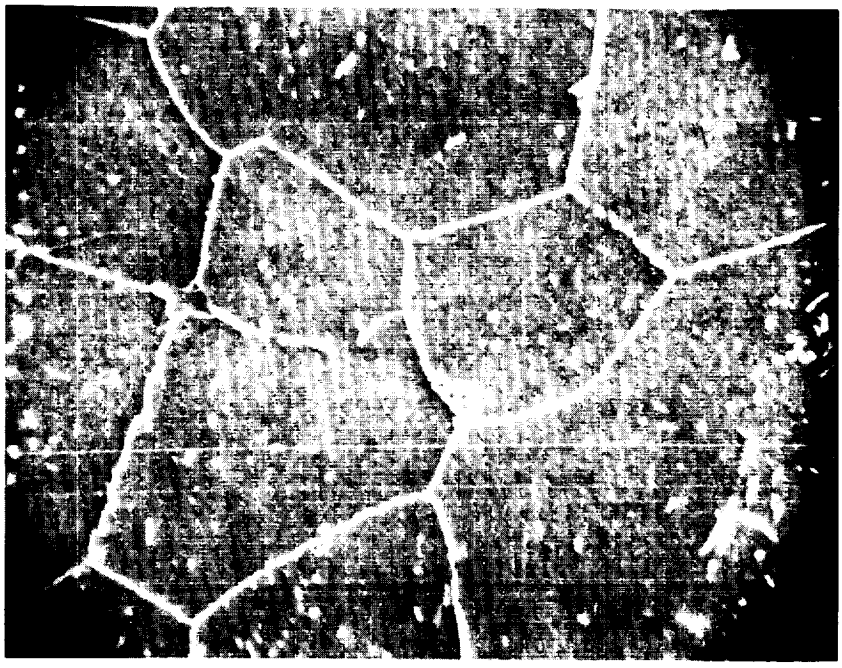

(b) 2000X

Figure 2. Microstructure of ASTAR 811C alloy annealed 1 hour at 3000°F (1922°K).

Table I

Chemical Analysis of As-Received Test Materials

	Element						
	Percent			PPM			
	W	Hf	Re	C	O	N	H
T-111 Alloy							
Nominal Composition							
Minimum	7.0	1.8	-	-	-	-	-
Maximum	9.0	2.4	-	50	100	50	10
Vendor Analysis	8.1	1.9	-	<30	<50	17	1.3
TRW Analysis	8.0	2.2	-	80	33	35	5
ASTAR 811C Alloy							
Nominal Composition							
Minimum	7.5	0.7	1.0	200	-	-	-
Maximum	8.5	1.1	1.5	300	100	50	10
Vendor Analysis	7.8	0.83	0.91	230	100	12	1.4
TRW Analysis	7.8	0.94	0.98	290	22	9	3

with both length and density being corrected for thermal expansion using the previously measured expansion coefficient. Poisson's ratio υ was calculated from the measured values of E and G using the formula

$$\upsilon = (E/2G)-1 \quad \text{(assuming isotropic properties)}$$

Results of these tests are presented in Tables 2-5 and in Figures 3 and 4 where each of the physical properties measured is plotted versus temperature.

The ultimate strength, 0.2% offset yield strength, elongation, and reduction of area were measured at temperatures between ambient and 2600°F (1700°K) in a Brew vacuum furnace at pressures below 1×10^{-5} torr. Bar type specimens with a 0.113" (2.89mm) diameter by 0.450" (11.5mm) long gauge section were tested at a constant crosshead speed corresponding to an initial strain rate of .0045 in/in/min (7.5×10^{-5} mm/mm/sec.). Results of these tests (Tables 6 and 7, Figures 5 and 6) show a significant dynamic strain aging effect in the 1200 to 2000°F (922 to 1366°K) temperature range for both alloys. This effect is very pronounced in the T-111 alloy, and is also noted in the ASTAR 811C alloy.

Table 2

Thermal Expansion of T-111 Alloy
Annealed 1 Hour at 3000°F (1922K)

Temperature		Specimen Length		Thermal Expansion μ in/in (mm/mmx10^6)
F	K	in	mm	
75	297	1.99638	50.7081	-
310	428	1.99785	50.7454	736
510	539	1.99940	50.7848	1513
710	650	2.00113	50.8287	2379
770	683	2.00155	50.8394	2590
1005	814	2.00305	50.8775	3341
1200	922	2.00465	50.9181	4142
1400	1033	2.00610	50.9549	4869
1600	1144	2.00770	50.9956	5670
1800	1255	2.00943	51.0395	6537
2000	1366	2.01105	51.0807	7348
2200	1477	2.01304	51.1312	8345
2400	1589	2.01463	51.1716	9142
2600	1700	2.01630	51.2140	9978

Table 3

Thermal Expansion of ASTAR 811C Alloy
Annealed 1 Hour at 3000°F (1922K)

Temperature		Specimen Length		Thermal Expansion μ in/in (mm/mmx10^6)
F	K	in	mm	
75	297	1.99580	50.6933	-
253	396	1.99725	50.7302	727
522	546	1.99905	50.7759	1628
817	708	2.00110	50.8279	2656
1040	833	2.00265	50.8673	3432
1209	927	2.00410	50.9041	4159
1400	1033	2.00533	50.9354	4775
1600	1144	2.00703	50.9786	5627
1800	1255	2.00863	51.0192	6428
2000	1366	2.01030	51.0616	7265
2200	1477	2.01210	51.1073	8167
2400	1589	2.01380	51.1505	9019
2600	1700	2.01563	51.1970	9936

Table 4

Physical Property Data for T-111 Alloy
Annealed 1 Hour at 3000°F (1922K)

Test Temperature		Modulus of Elasticity				Calculated Poisson's Ratio
		Longitudinal		Shear		
F	K	psix10^{-6}	mn/m^{2}x10^{-3}	psix10^{-6}	mn/m^{2}x10^{-3}	
Room Temperature		26.5	182.6	10.6	73.0	.26
500	533	25.4	175.0	10.2	70.3	.25
1000	811	24.4	168.1	9.9	68.2	.24
1500	1089	23.5	161.9	9.5	65.5	.24
1800	1255	23.1	159.2	9.3	64.1	.24
2000	1366	22.9	157.8	9.1	62.7	.25
2200	1478	22.6	155.7	9.0	62.0	.26
2400	1589	22.5	155.0	8.8	60.6	.28
2600	1700	22.3	153.6	8.5	58.6	.30

Table 5

Physical Property Data for ASTAR 811C Alloy
Annealed 1 Hour at 3000°F (1922°K)

Test Temperature		Modulus of Elasticity				Calculated Poisson's Ratio
		Longitudinal		Shear		
F	K	$psix10^{-6}$	mn/m^2x10^{-3}	$psix10^{-6}$	mn/m^2x10^{-3}	
Room Temperature		27.9	192.2	10.3	71.0	.34
1000	811	26.2	180.5	9.8	67.5	.34
1500	1089	25.2	173.6	9.6	66.1	.32
1800	1255	24.7	169.5	9.5	65.5	.31
2000	1366	24.4	168.1	9.4	64.8	.30
2200	1478	24.1	166.0	9.3	64.1	.30
2400	1589	23.8	164.0	9.3	64.1	.28
2600	1700	23.4	161.2	9.3	64.1	.26

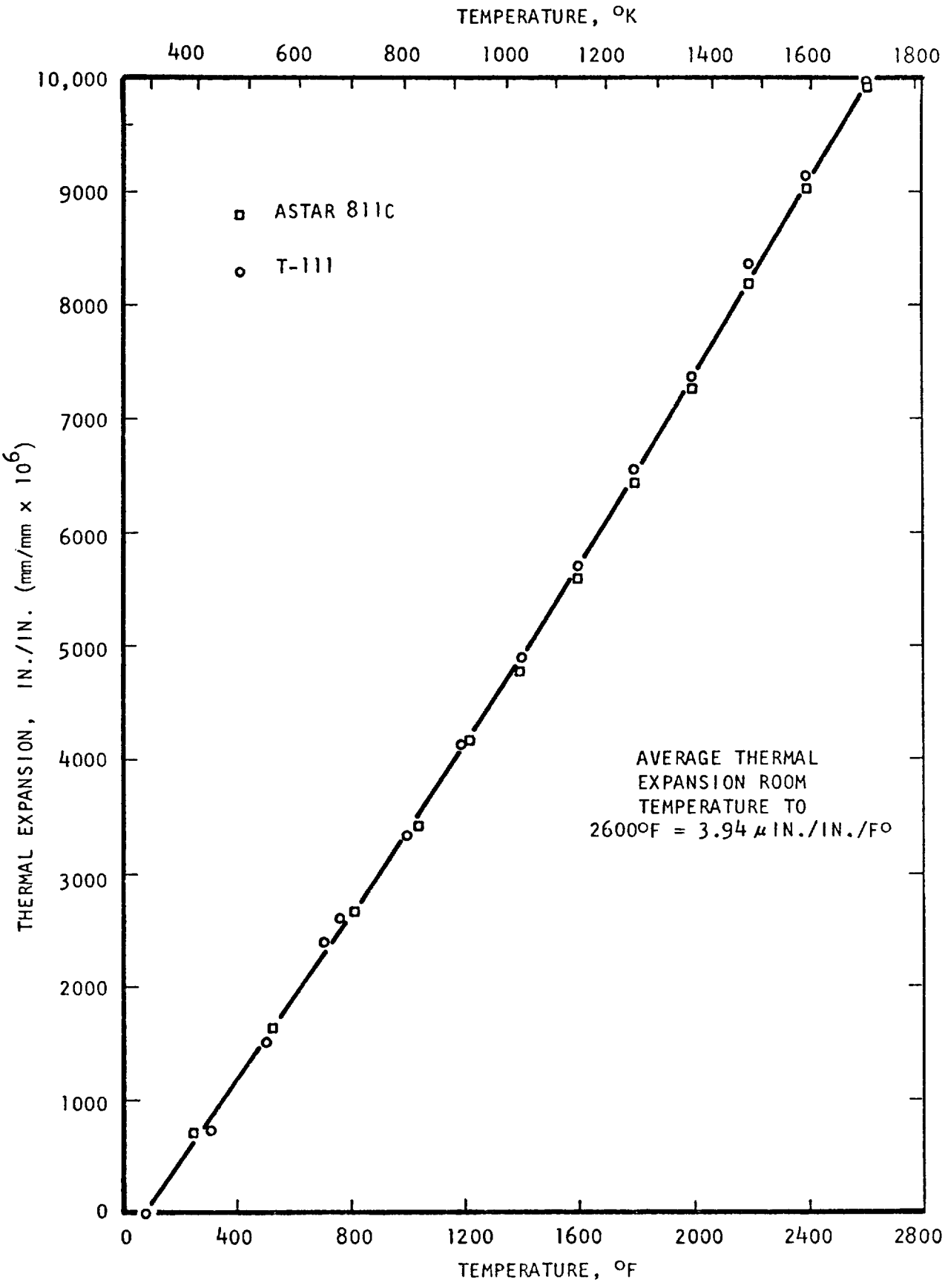

Figure 3. Thermal expansion of T-111 and ASTAR 811C alloys.

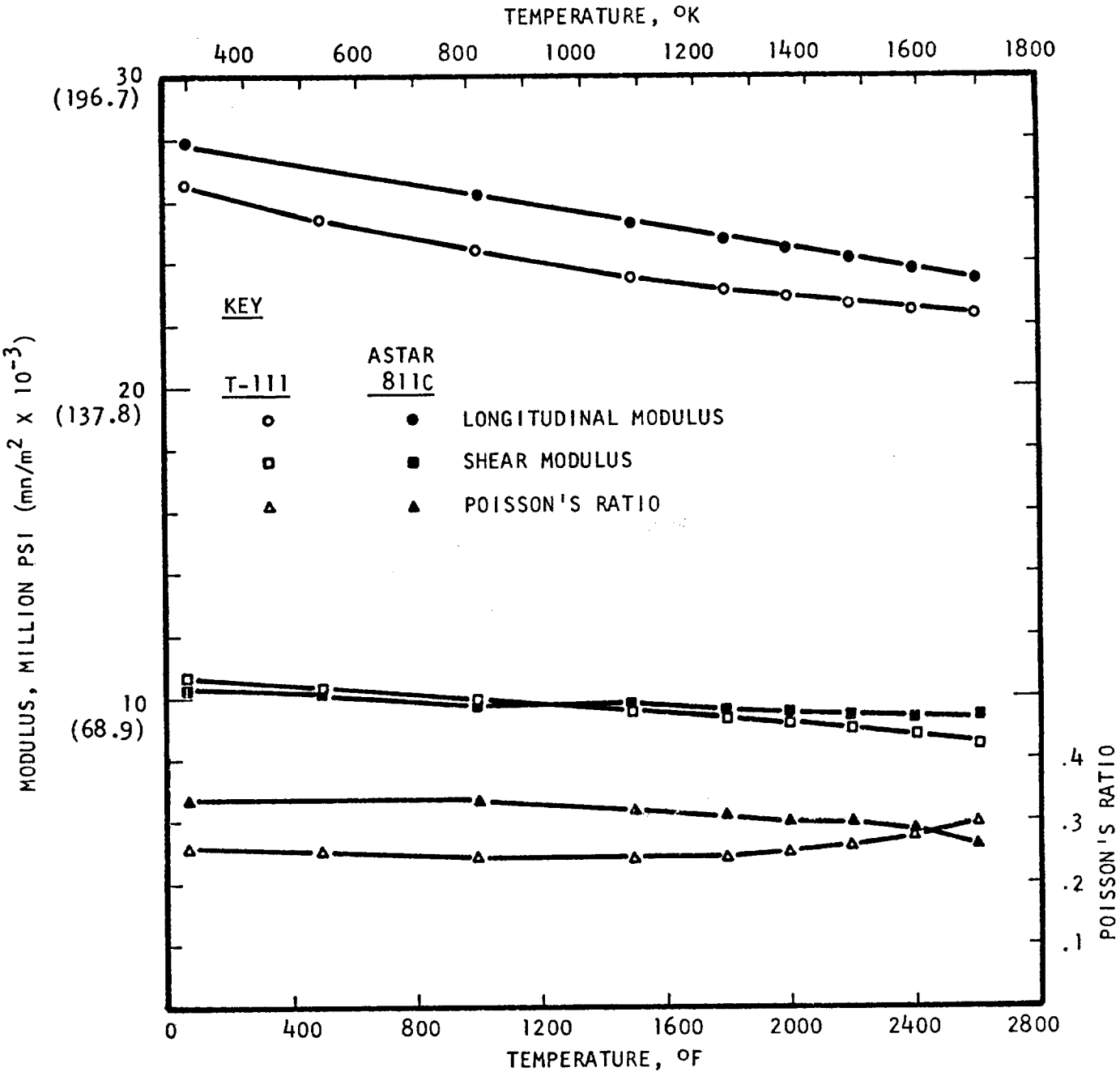

Figure 4. Influence of temperature on modulus and Poisson's Ratio of T-111 and ASTAR 811C alloys.

Table 6

Tensile Properties of
T-111 Alloy Annealed 1 Hour at 3000°F (1922°K)

Test Temperature °F	Test Temperature °K	Ultimate Tensile Strength ksi	Ultimate Tensile Strength mn/m²	0.2% Offset Yield Strength ksi	0.2% Offset Yield Strength mn/m²	Elongation % in 4D	Percent Reduction of Area
Room Temperature		87.2	600.8	72.9	502.3	31	59
Room Temperature		87.4	602.2	75.0	516.8	35	74
500	533	74.5	513.3	57.1	393.4	40	86
1000	811	60.3	415.5	55.6	383.1	30	89
1500	1089	65.1	448.5	33.9	233.6	34	67
1800	1255	59.7	407.2	26.7	184.0	29	56
2000	1366	50.1	345.2	31.5	217.0	29	54
2200	1478	39.6	272.8	27.8	191.5	39	61
2400	1589	33.9	233.6	26.0	179.1	36	69
2600	1700	25.9	178.5	20.8	143.3	48	73

Table 7

Tensile Properties of ASTAR 811C Alloy Annealed 1 Hour at 3000°F (1922°K)

Test Temperature °F	Test Temperature °K	Ultimate Tensile Strength ksi	Ultimate Tensile Strength mn/m^2	0.2% Offset Yield Strength ksi	0.2% Offset Yield Strength mn/m^2	Elongation % in 4D	Percent Reduction of Area
Room Temperature		105.6	727.6	81.2	559.5	20	26
Room Temperature		106.2	731.7	83.0	571.9	19	19
500	533	82.9	571.2	57.4	395.5	15	27
1000	811	80.9	557.4	52.4	361.0	19	59
1500	1089	80.8	556.7	43.7	301.1	24	63
1800	1255	68.6	472.7	37.0	254.9	29	69
2000	1366	58.0	399.6	38.6	266.0	24	74
2200	1478	41.5	285.9	32.0	220.5	21	76
2400	1589	38.3	263.9	35.1	241.8	32	78
2600	1700	31.9	219.8	28.7	197.7	30	80

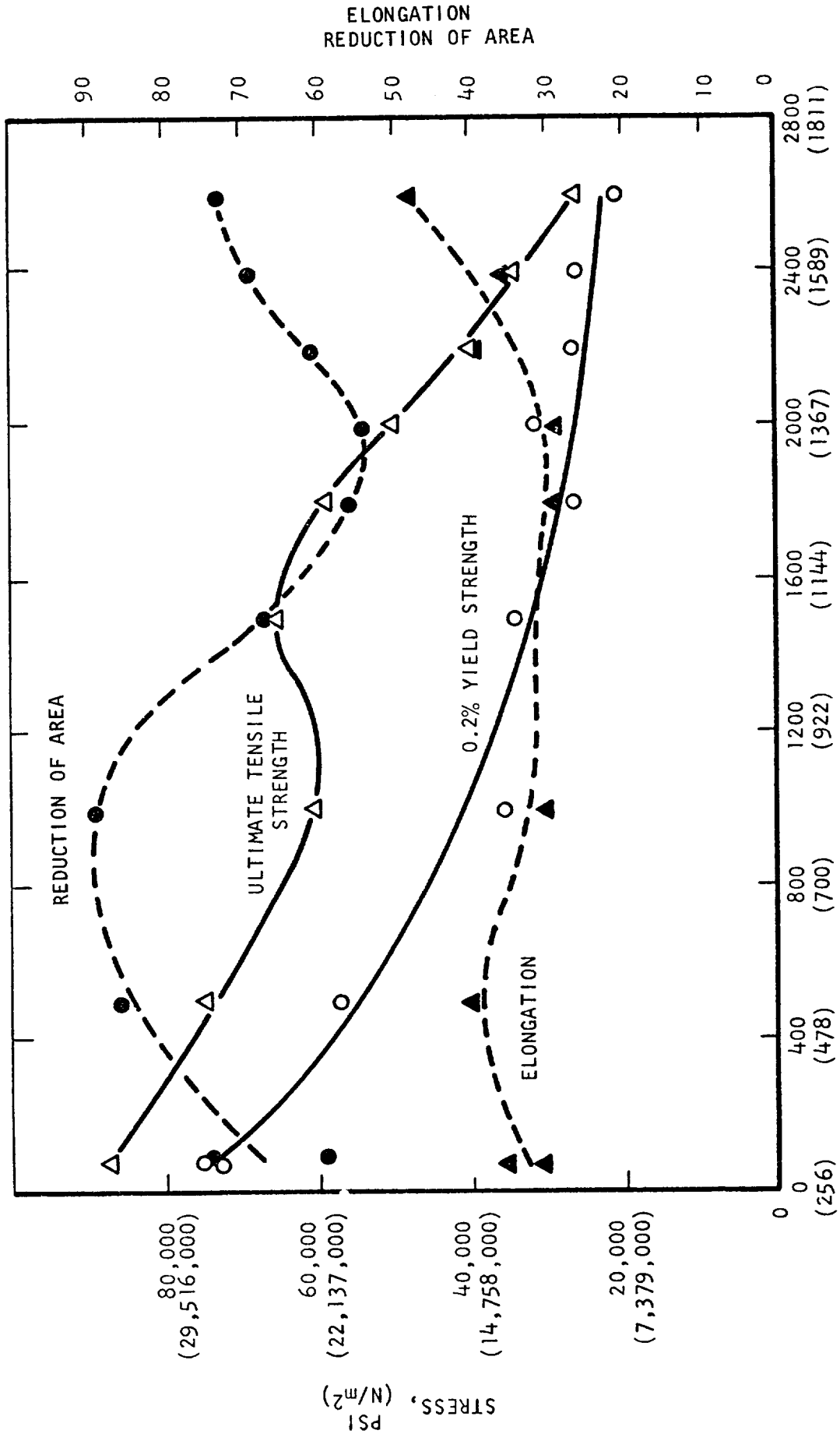

Figure 5. Tensile properties of T-111 alloy.

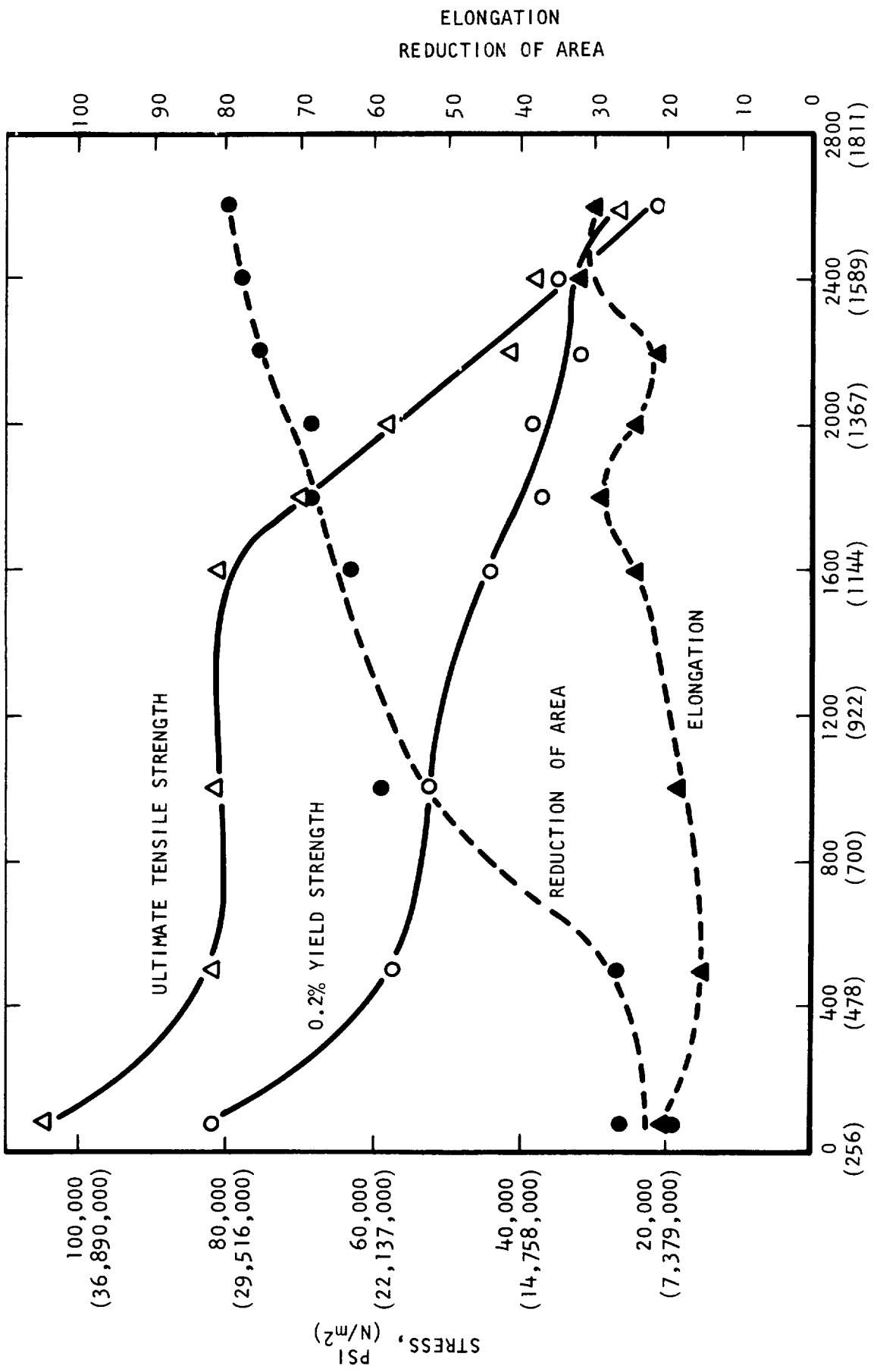

Figure 6. Tensile properties of ASTAR 811C alloy.

III PHASE II - DESCRIPTION OF THE THERMAL FATIGUE TEST APPARATUS

The test apparatus was designed to conduct completely reversed push-pull fatigue tests in ultrahigh vacuum on hourglass type specimens using independently programmed temperature and strain cycles. Temperature was programmed using a thyratron-controlled 50 KV AC power transformer for direct resistance heating of the specimen, while diametral strain was controlled directly using an LVDT type extensometer coupled to a programmable closed loop electro-hydrualic servo system. A photograph of the test system is shown in Figure 7, while a detailed description of each component of the system follows.

A. Mechanical Test System

1. Test Frame

The test frame consisted of two 3" (6.9 cm) steel plattens assembled to four 4" (10.2 cm) diameter threaded upright columns with locking nuts above and below each platten. A double acting 50,000 pound (223,000 N) hydraulic cylinder attached below the lower platten was equipped with an adjustable 0.6" (15.3 mm) range LVDT for measurement and/or direct feed back servocontrol of ram (crosshead) position. The space between the two plattens contained the fatigue load train together with the controlled environment test chamber (Figure 8).

2. Load Train

The upper half of the load train (Figure 9) was threaded to the upper platten, with a 7" (17.8 cm) diameter by 3" (7.6 cm) thick brace being used to preload the joint and prevent backlash in the threads under conditions of reversed loading. The upper load train also incorporated a load cell together with fixturing for the attachment of cooling water and low voltage, high current electrical power to the upper pull bar. The pull bar penetrated the test chamber through a stainless steel bellows assembly below the electrical and water attachments so that it was not necessary to provide separate feed throughs for power or cooling water. The upper flange of the bellows assembly was sealed with a viton "O" ring to provide electrical insulation between the upper electrical connector and the test chamber. This insulation was necessary to prevent direct shorting of the heating current through the chamber. All other flanges in the load train were sealed with crushable copper gaskets, following ordinary UHV practice.

The lower (movable) half of the load train (Figure 10) was similar to the upper half but had no load cell in the pull bar, and was electrically insulated at the mechanical joint between the lower pull bar and the hydraulic actuator to prevent shorting of the heating current through the test frame.

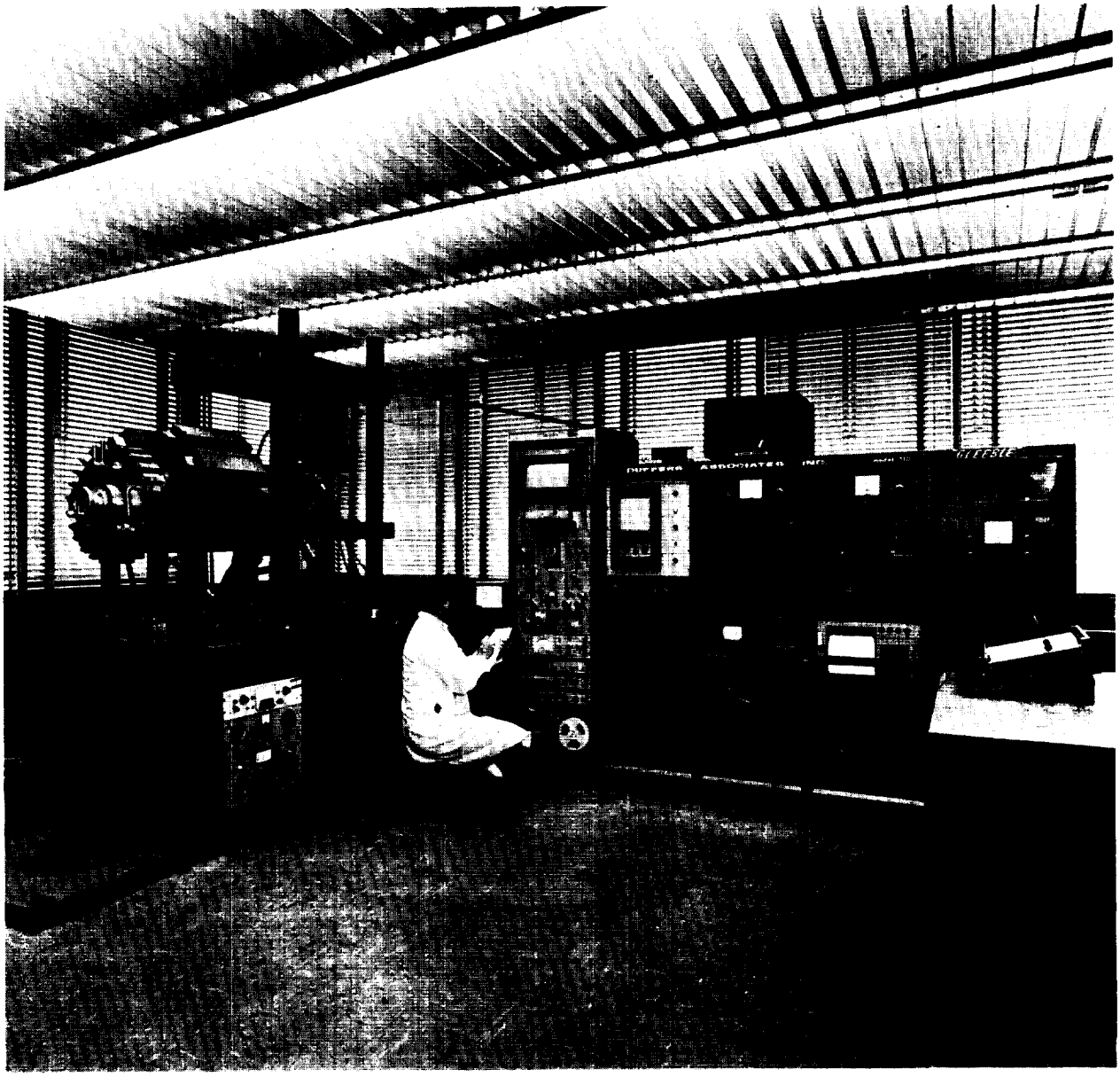

Figure 7. Thermal mechanical fatigue test system.

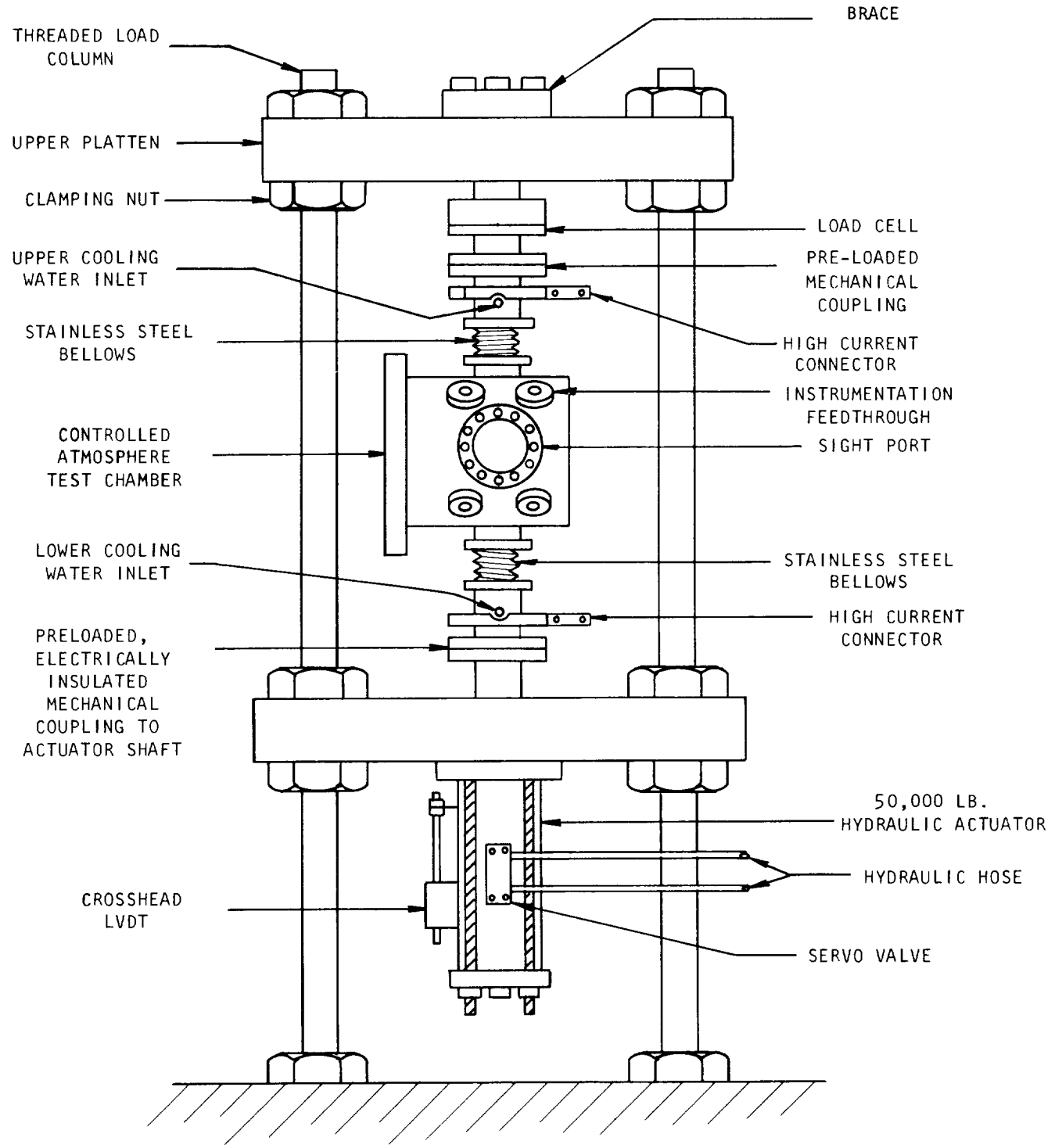

Figure 8. Schematic diagram of low cycle thermal fatigue test frame.

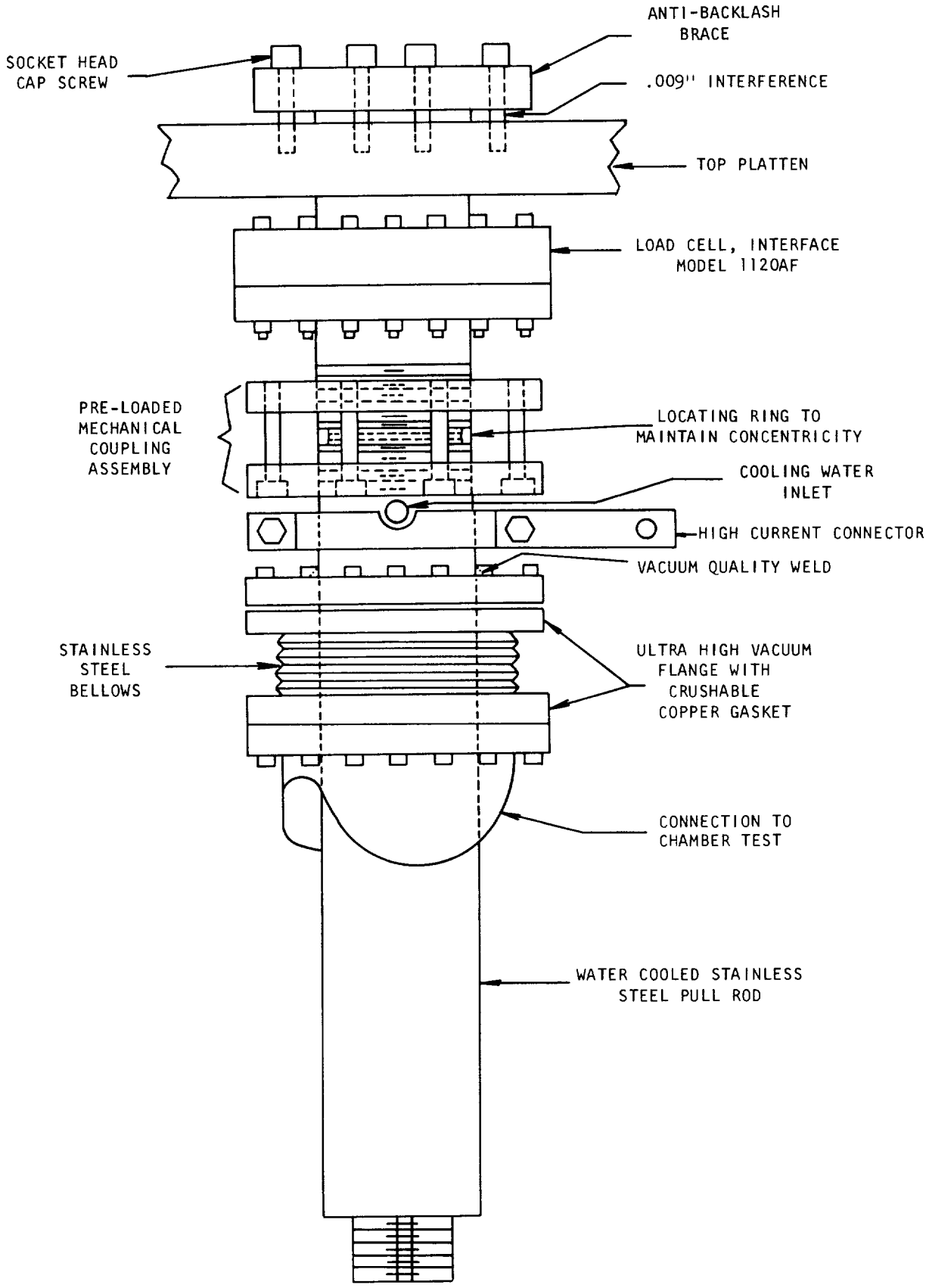

Figure 9. Low cycle thermal fatigue test load train assembly - upper half.

3384 c

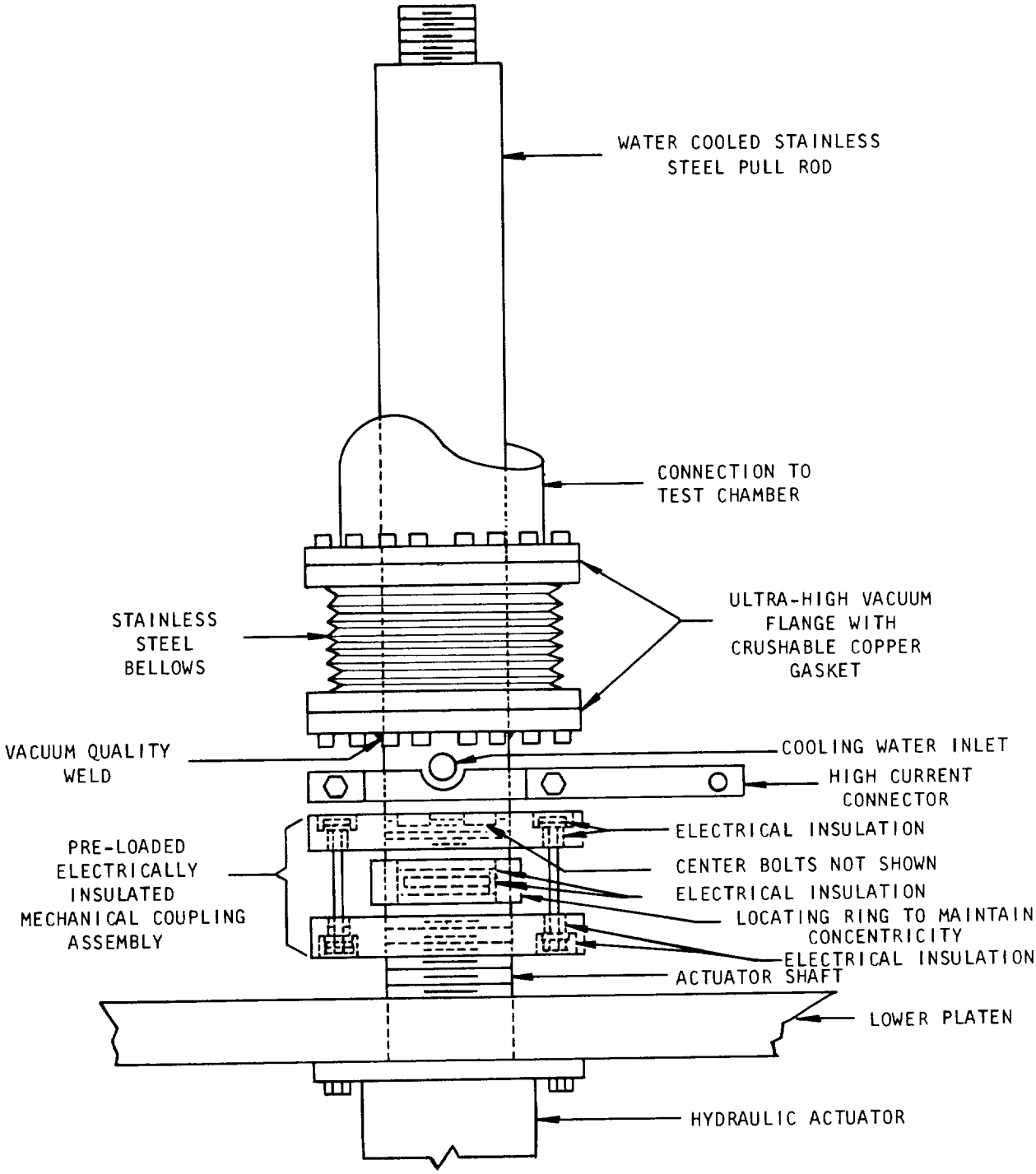

Figure 10. Low cycle thermal fatigue test load train assembly - lower half.

3386 c

One feature not shown on the illustrations was the use of cooling fans for the stainless steel bellows. Experience with the system revealed a tendency for induction heating of the bellows by the large AC fields in the vicinity of the load train, so that it was necessary to add fans to the test frame to cool the bellows during testing.

3. Specimen and Grip Assembly

The standard test specimen and grip assemblies are illustrated in Figures 11 and 12. The specimen test section had an hourglass configuration with a radius of 1.5" (3.8 cm). The notch geometry shown in Figure 11 was used for notched testing. The 20° tapered ends of the test specimen fit matching tapered holes in the upper and lower grip assemblies, which insured precise alignment of the specimen in the grip (Figure 12). A double collar arrangement was used to clamp the threaded part of the specimen to each grip with sufficient preload to prevent backlash under reversed loading conditions. The grip itself was made of TZM alloy for improved thermal conductivity, and was seated to the pull bar with a copper washer to insure good thermal and electrical conductivity across the joint. The outer collar was made of invar to prevent loosening of the specimen by differential thermal expansion during testing. Another important feature of this system was the use of gas relief slots cut in all threads for application of the system in ultrahigh vacuum. Experience showed this gripping system to be satisfactory with the provision that the specimen must be installed in the grip assembly under a compressive load and the collars must be hammered tight using a spanner wrench to insure adequate preload. This same provision also applied to installation of the grip to the pull bar. The load train alignment was checked periodically by insertion of the alignment pins illustrated in Figure 13. Adjustments were made in load train alignment by slight changes in the position of the main platten.

4. Instrumentation

Instrumentation was provided to measure temperature and diametral mechanical strain during operation of the thermal-mechanical fatigue test apparatus. Temperature was measured using tungsten-3%Re/tungsten-25%Re thermocouple wires spot welded to the test specimen about 1/4" (6.35 mm) above and below the minimum diameter, thus providing redundancy in the case one thermocouple failed. The individual thermocouple wires penetrated the test chamber through standard glass-to-metal sealed ultrahigh vacuum instrumentation feedthroughs. Because of the hourglass shape, temperature was not uniform along the length of the specimen and the observed thermocouple output had to be compensated to determine the temperature at the minimum diameter (maximum stress) area. This was accomplished by measurement of specimen temperature at the hottest point using an optical pyrometer which had been previously calibrated for deviations between actual and optical temperature by the temporary attachment of thermocouples at the minimum diameter of a dummy specimen.

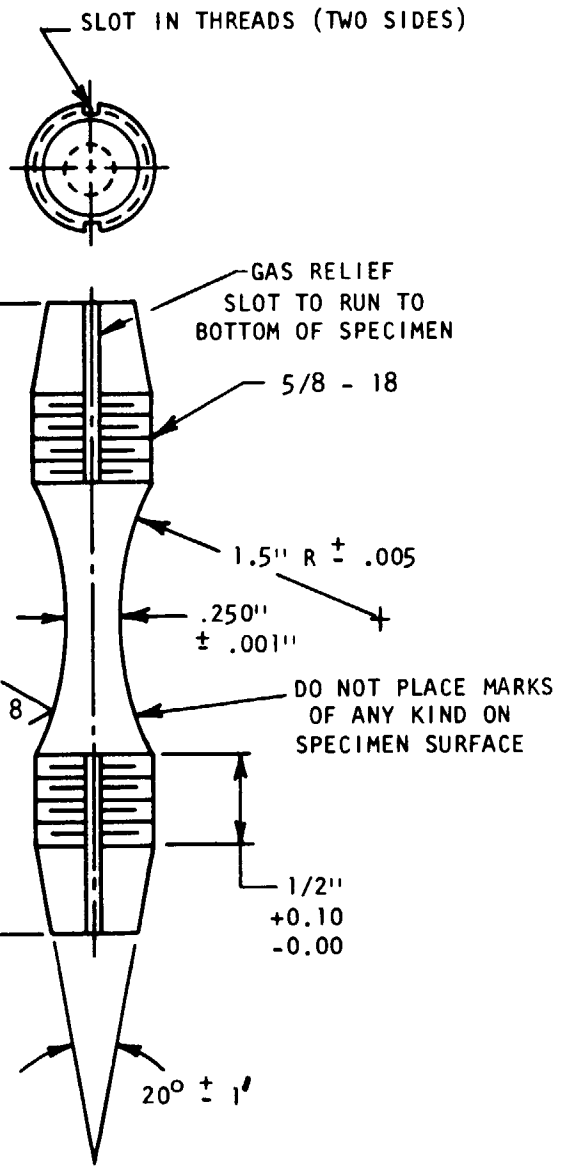

Figure 11a. Test specimen for thermal fatigue testing.

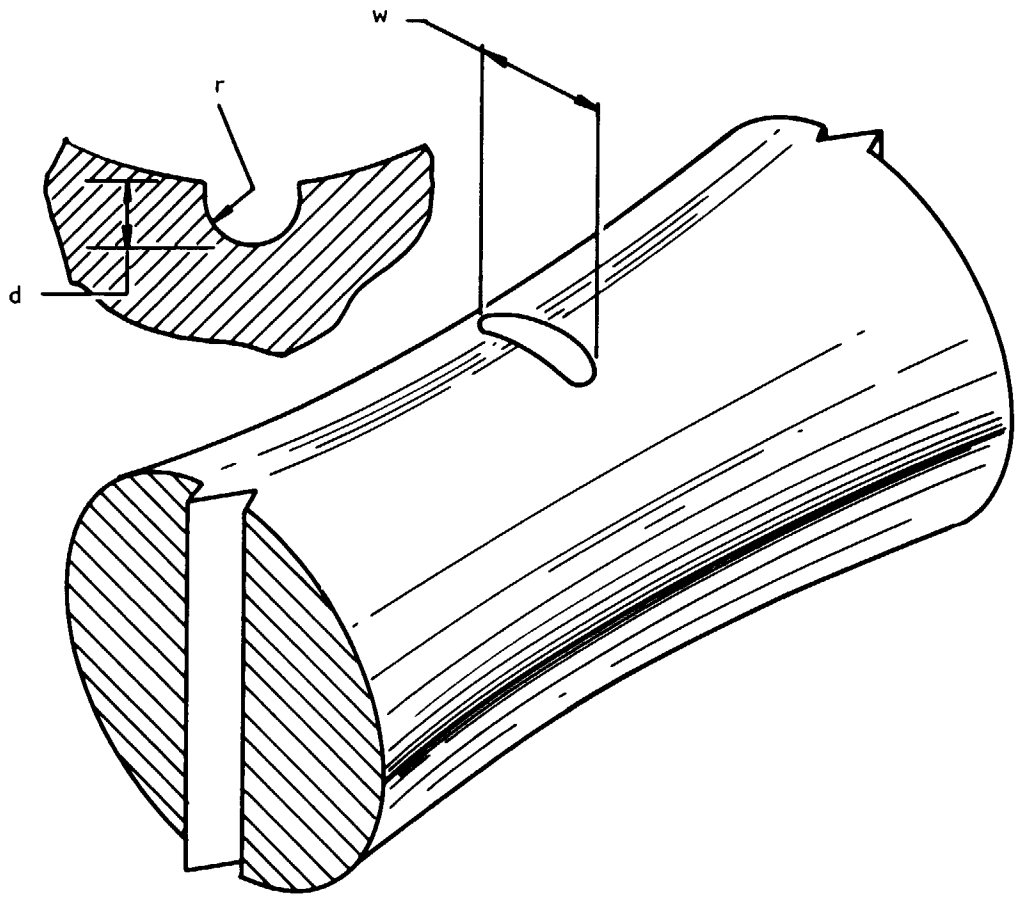

Figure 11b. Fatigue specimen notch geometry.

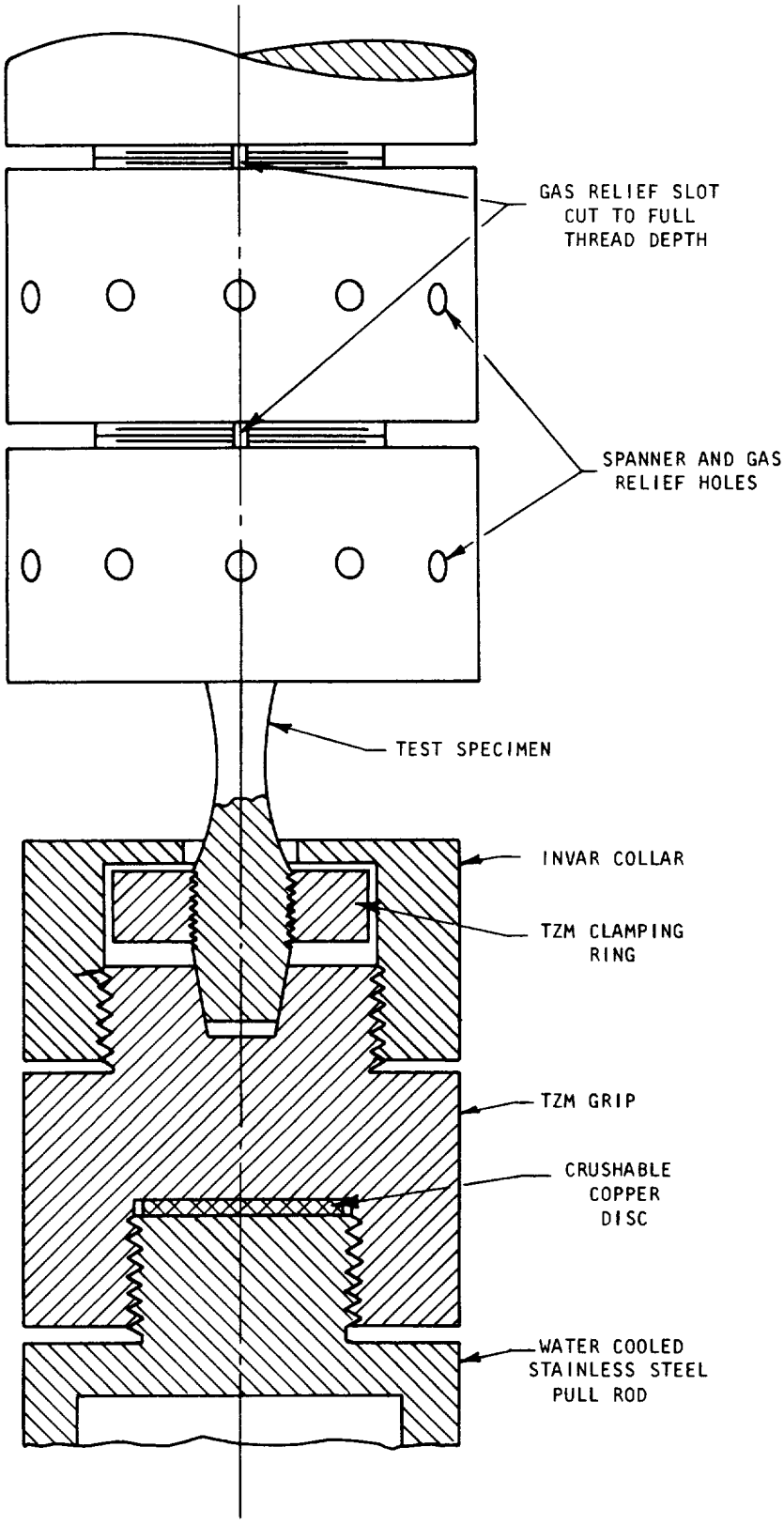

Figure 12. Low cycle thermal fatigue test specimen and grip assembly.

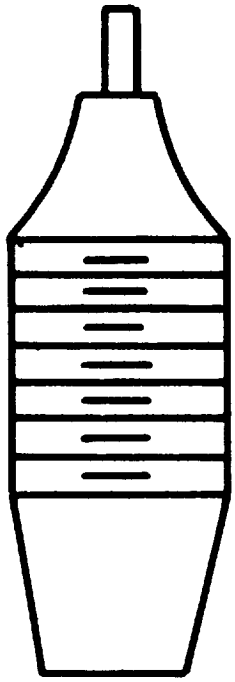

Figure 13. Low cycle thermal fatigue test load train alignment pin.

Specimen diameter was measured using a simple scissors-action LVDT type of extensometer illustrated in Figure 14. The scissors design was chosen to minimize anomalous diameter changes which could result from heating of the extensometer arms with other designs. The hinge was made of invar, while the arms were 3/8" diameter alumina tubes. The relatively large diameter of these arms allowed the extensometer to be clamped to the specimen with significant force without exerting a large pressure on the specimen. Experience indicated that the fatigue crack rarely initiated at the contact point, indicating that the contact between the extensometer and the specimen did not influence the crack initiation process.

Two springs were used to hold the extensometer to the specimen. A relatively light expansion spring was located between the rods on the LVDT side of the hinge, while a much stronger spring compressed the outside of the arms against the test specimen. This direct application of spring tension was desirable because it eliminated the possibility of part of the specimens diameter change not being translated to the LVDT because of elastic bending of the alumina rods.

The LVDT core was attached to the end of one of the alumina rods in such a way that it moved freely back and forth in the coil. The coil was welded into a vacuum tight stainless steel jacket which was attached to the end of the second alumina rod. Thus, changes of specimen diameter caused scissoring of the extensometer arms which in turn caused the LVDT core to move axially in the coil. The extensometer arms were designed to equal length on both sides of the hinge, so that the movement of the core seen by the LVDT was 1:1 with specimen diameter changes. This meant that the extensometer could be directly calibrated outside the chamber before assembly using a micrometer-type calibration device to drive the core through the coil. It was also possible to check the calibration by measuring the free thermal expansion of a material having a known coefficient of thermal expansion.

Both the core and coil of the LVDT were supported in the test chamber by thin wires which allowed freedom of movement for the extensometer to follow the specimen movements during testing. The working end of the extensometer was also provided with support wires, but these were adjusted to have slack during testing so that the weight of the working end of the extensometer was actually carried by the friction between the specimen and arms.

Electrical connections to the extensometer penetrated the stainless steel shell around the coil through an ultrahigh vacuum epoxy seal molded so as to separate and dress the bare lead wires for attachment to the conduit cable. The lead wires were of stranded, highly flexible construction and were bent slack to accomodate the freedom of movement built into the support system. The conduit which carried the signal to the outer chamber wall was a formed copper tube containing a standard individually shielded 3-pair instrumentation cable. This assembly was vacuum sealed at both ends by UHV epoxy cement, with the leads being dressed at both ends to mate with the LVDT leads and with the leads from the instrumentation feed through where the cable penetrated the main test chamber.

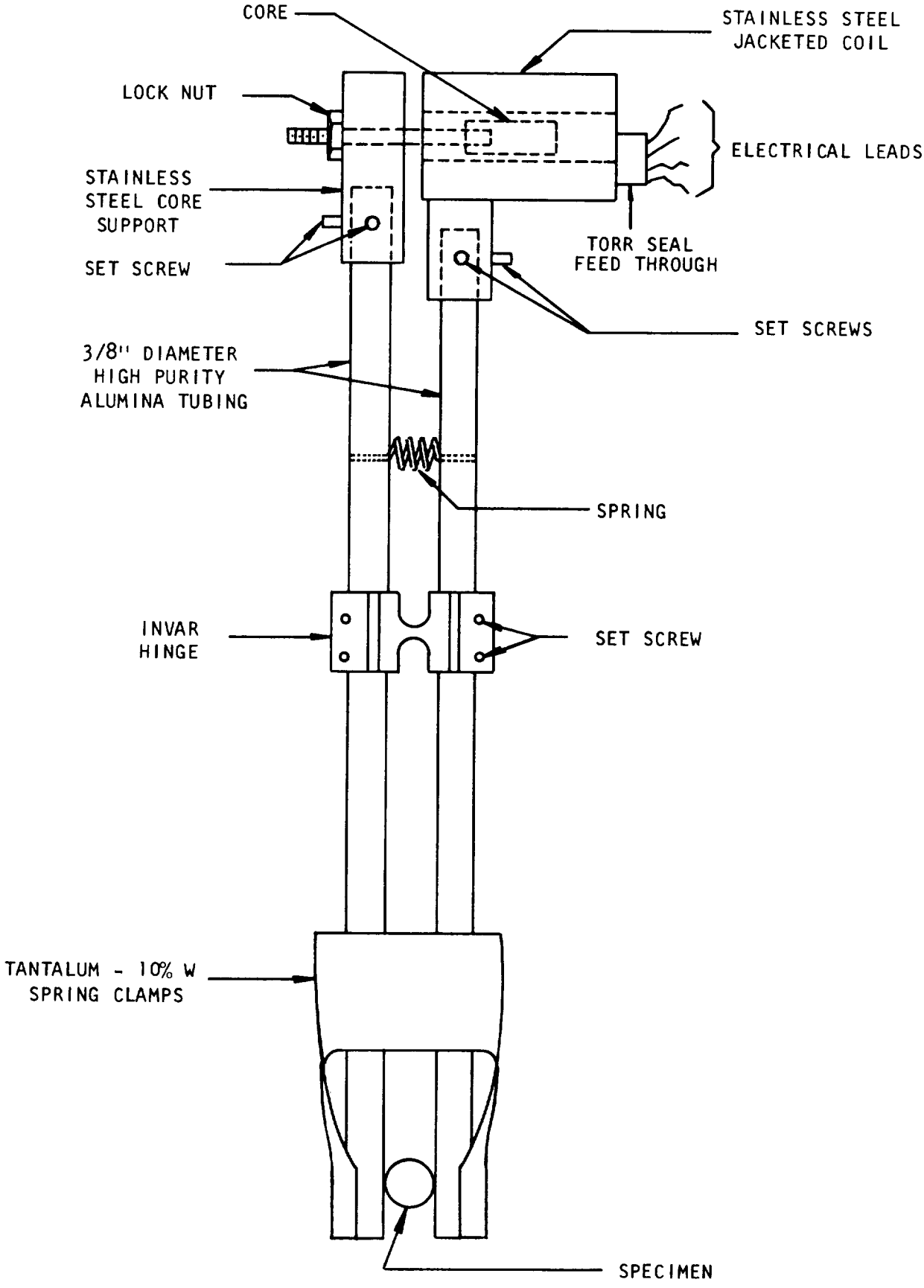

Figure 14. Extensometer used to measure specimen diameter for low cycle thermal fatigue testing.

Figure 15 shows the assembled extensometer installed in the vacuum chamber ready for testing. Experience with this system has proven the design to be satisfactory both for measurement and for direct feed back programmed servocontrol of specimen diameter. However, because of the large AC fields generated near the high current load train assembly, it was necessary to pay very careful attention to dressing and shielding of the signal leads during initial installation of this assembly. This requirement included considerable trial and error experimentation with placement and shielding of the leads before a suitably clean feed back signal could be achieved.

5. Mechanical Control System

A block diagram illustrating the main components of the closed loop servocontrol system is shown in Figure 16. Any one of the three different test parameters, load, crosshead position, or specimen diameter, could be used as the independent variable for programmed control. The basis of the control system was the servoamplifier, which electronically summed the command and feed back signals to generate an output signal which controlled the opening of the hydraulic servovalve. Ram velocity feed back was also used to damp the system and prevent an over-controlling oscillatory condition from developing. LVDT and load cell signal conditioners detected, amplified, and conditioned the respective instrument inputs to provide continuously variable servoamplifier input signals ranging from plus to minus 10 VDC for positive and negative full scale deflections of the respective sensing devices. A ±1 VDC output was also available from each module for recording purposes. The servoamplifier incorporated a thermal compensating circuit which used the specimen thermocouple signal to compensate the servoamplifier output for free thermal expansion of the specimen while varying temperature under diametral strain control. A biasing potentiometer in the servoamplifier provided the capability to bias the command input so that the independent variable could be cycled about a value other than zero.

Three sources of programmed command signal were available. The first was a simple reversible motor driven potentiometer device which provided a ±10 VDC triangular wave command signal at a fixed frequency of 0.0065 Hz. The second command source was an electrostatic curve follower which operated at a range of test frequencies and could be programmed for any desired wave shape, while the third source was an electronic function generator which provided square, triangular, or sine wave shapes from sonic frequencies to 0.01 Hz. Selection of the command source, together with overall coordination of the heating and mechanical straining functions was performed by the master controller which is described more fully in a subsequent section.

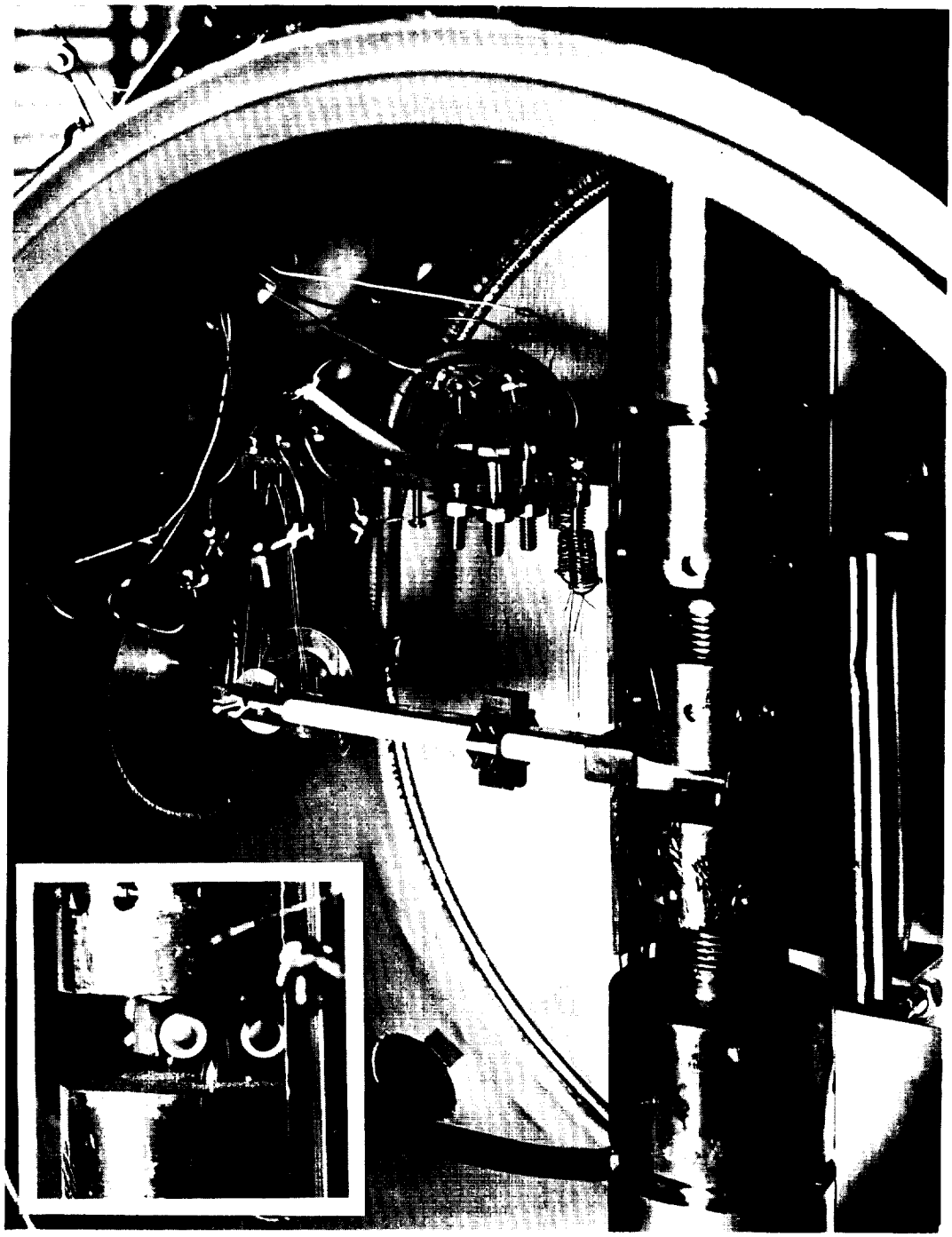

Figure 15. Extensometer assembly installed in test chamber.

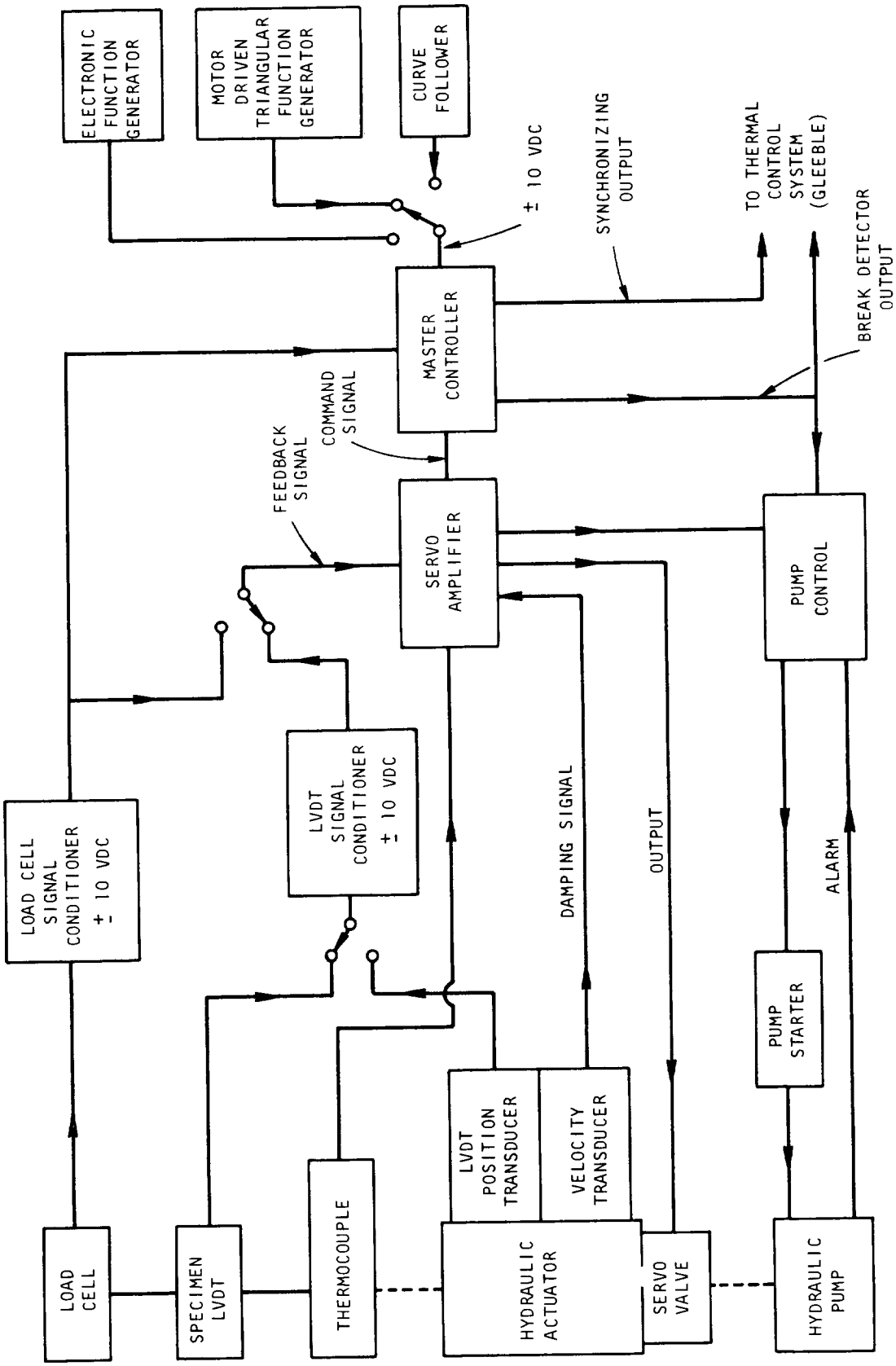

Figure 16. Block diagram of low cycle thermal fatigue mechanical control system.

B. Thermal Control and Heating System

The basis of the thermal control and heating system was a Duffer's Associates Model 510 "Gleeble" which was adapted for direct resistance heating of the low cycle fatigue test specimen. The Gleeble was originally designed to perform welding oriented research on the influence of rapid thermal cycling on the structure and properties of materials. A 50 KVA transformer provided the capability for heating at rates to 3000F°/second (1667K°/second) in metallic specimens with cross-sectional areas of 0.16 $in.^2$ (1.04 cm) or less, while a reference generator programmed the entire thermal cycle according to any desired wave shape. A temperature control feed back signal was provided by the W-Re thermocouple welded to the test specimen as described previously. A block diagram of the temperature control system is shown in Figure 17. The emf of the thermocouple was compared in the error signal network to the programmed output of the reference generator. Any deviation of the thermocouple emf from the reference generator output resulted in an error signal to the "control amplifier." This operated the thyratron power control which regulated the power supply to the step-down transformer and test specimen.

The basis of the reference generator was a motor driven continuously rotating potentiometer with multiple taps for adjustment of input potential at various points around the slide wire. Four different synchronous motors were available to drive the generator at speeds of 718, 155, 46, and 18 seconds per cycle. The drive system was modified so that it could be started and stopped on command from the master controller, described in the next section. A relay network was also added to the reference generator so that it could generate its own stopping signal. It was important that both the temperature and strain reference generator be self-terminating at the end of each cycle so that both could be re-initiated simultaneously to start another cycle in perfect synchronization on signal from the master controller. This insured that any slight deviations in the duration of the thermal and mechanical cycles would not be additive from cycle to cycle.

C. Master Control System

The master control system generated the triangular strain command signal used in the majority of cyclic fatigue tests and provided synchronizing signals for initiating cycles, data acquisition functions, hold times, etc. The basic components of the system were a reversible 72 rpm (4320 rps) synchronous motor, a 10 turn potentiometer, and a 10 position continuously adjustable cam switch. These components were linked through a gear train which provided the correct relative speeds for each component and insured exact synchronization of the various control functions. The gearing provided a fixed cycle duration of 155 seconds, to match the second speed on the Gleeble reference generator.

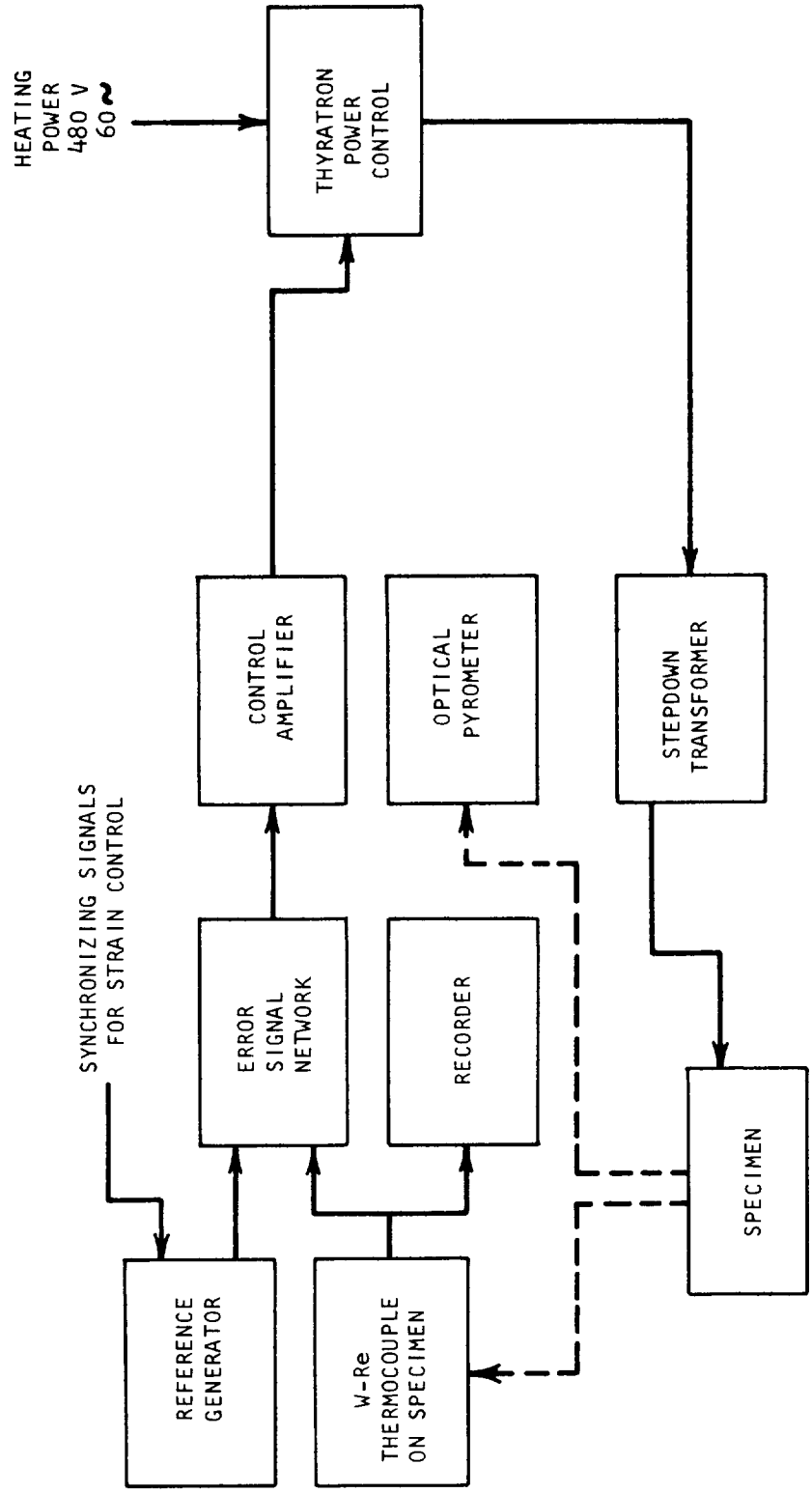

Figure 17. Block diagram of low cycle thermal fatigue thermal control system.

The control system operated by driving in one direction until the limit of travel on the 10 turn potentiometer was reached, at which point a cam was set on the cam switch to reverse the motor and drive the potentiometer to its opposite extreme, where another cam again reversed the drive motor to restart the cycle. Two delay capabilities were built into this system. First, time delay relays adjustable between 0 and 180 seconds were optionally activated at each reversal point, providing a built in short-time delay at each end of the cycle. This capability was used to provide a few seconds pause in each cycle (usually at the minimum temperature point), and operated in conjunction with the self-stopping capability of the thermal control system to insure exact starting synchronization for each cycle, as discussed previously. These delay relays were also used to interrupt the strain cycle for tests of the type where strain and temperature changed sequentially rather than simultaneously during the test cycle. This capability together with the previously described thermal expansion compensator in the servoamplifier were particularly useful for conducting "square wave" types of tests where tensile and compressive deformations were both accomplished isothermally but at two different temperatures. The meaning and interpretation of this type of test will be discussed in more detail in a subsequent section.

The second time delay capability consisted of a timer which could be triggered at any point in the cycle to simultaneously interrupt both the temperature and strain programmers for times between 5 and 150 minutes, 300 and 9000 seconds) thereby providing for longer hold times.

Synchronizing signals for triggering of the thermal cycles were provided by two separate cams on the 10 position cam switch mentioned previously. These cams operated in conjunction with a set of relays to provide switch selectable triggering impulses either just before or just after the end point of the master control cycle. This arrangement provided the flexibility to conduct tests where the temperature and strain were synchronized either in-phase, out-of-phase, or sequentially to one another.

Also incorporated into the master controller was a break detector which cut off power to the hydraulic pump and Gleeble after the test specimen fractured. This system consisted of a ±1 VDC meter relay connected to the recording output of the load cell signal conditioner. This master relay operated in conjunction with a cam on the cam switch to seek a tensile load near the end of each tensile cycle. If a tensile load was found, no action was taken by the system; if no load was found, the test was terminated.

Spare cam switches were available on the master controller to perform other miscellaneous functions as desired, such as triggering of the electrostatic curve follower or independent electronic function generator for complex strain cycling, or for performing various data sampling and acquisition functions.

D. Data Acquisition Facilities

As discussed previously, both the load cell and LVDT signal conditioners were equipped with ±1 VDC recording outputs. These signals were used to record strain versus time on a strip chart recorder, and strain versus load on an X-Y type plotter. Temperature was recorded directly from the specimen thermocouple using a standard L&N balancing type millivolt temperature recorder. An auxiliary LVDT signal conditioner was available for measurement of specimen diameter when under crosshead control.

E. Environmental Control System

The environmental control chamber was a two part, all stainless steel system consisting of test and vacuum pump mudules separated by an externally operated poppet valve (Figure 18). This two part construction was extremely important since it allowed the test specimen to be changed while maintaining the major portion of the system under hard vacuum. It also allowed the test chamber to be back-filled with a protective atmosphere while testing without the need to shut off the vacuum pumps. This not only prolonged pump life significantly, it also provided much faster turn around time for changing specimens by shortening the time required to reach acceptable vacuum levels. The two modules were joined by a 20" (50.8 cm) diameter Wheeler flange which was sealed by a crushable copper "O" ring. This flange was located in the test module adjacent to the poppet valve and provided excellent access to the interior of the chamber for changing of the specimen when the two modules were separated (Figure 19).

The test chamber was permanently mounted to the test frame and was equipped with eight standard 1-1/2" (38.1 mm) flanged openings for mounting of various types of electrical and mechanical feed-throughs. Four 6" (15.3 cm) diameter flanges were also mounted to the chamber on the top and bottom and on both sides. The load train penetrated the chamber through the top and bottom flanges, while a 4" diameter sight port was mounted on one of the side flanges. The fourth flange was not used and was blanked off with a stainless steel plate.

The test chamber was rough pumped using a mechanically backed turbomolecular pump having a blank-off pressure capability of about 1×10^{-7} torr. In practice, this roughing system would bring the test chamber from atmospheric pressure to a limit of about 1×10^{-4} torr in 15 to 30 minutes 900 to 1800 seconds). An ultrahigh vacuum bellows sealed valve was provided to seal the test chamber from the roughing system when the chamber was under hard vacuum.

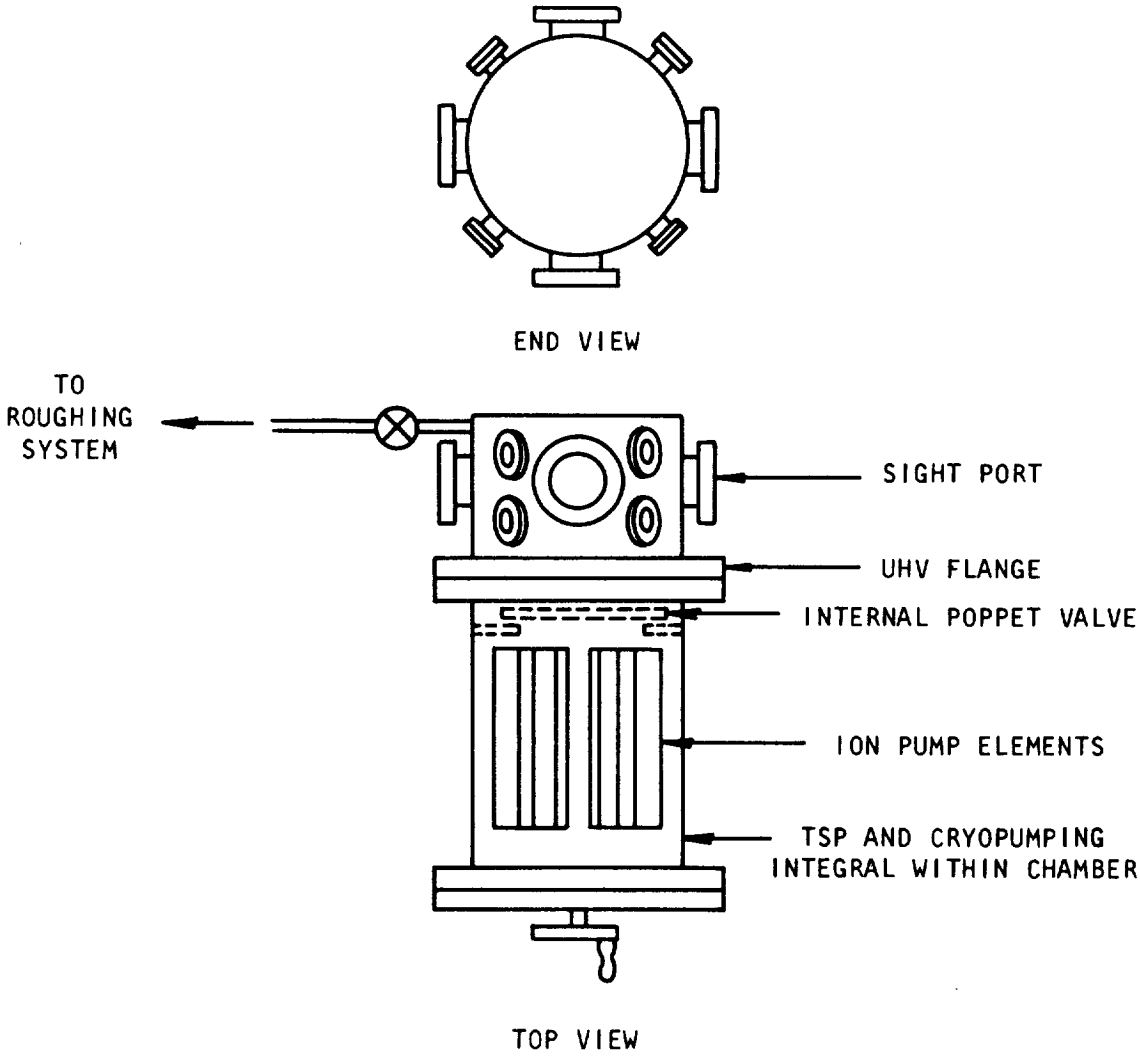

Figure 18. Schematic illustration of double chamber low cycle thermal fatigue vacuum system.

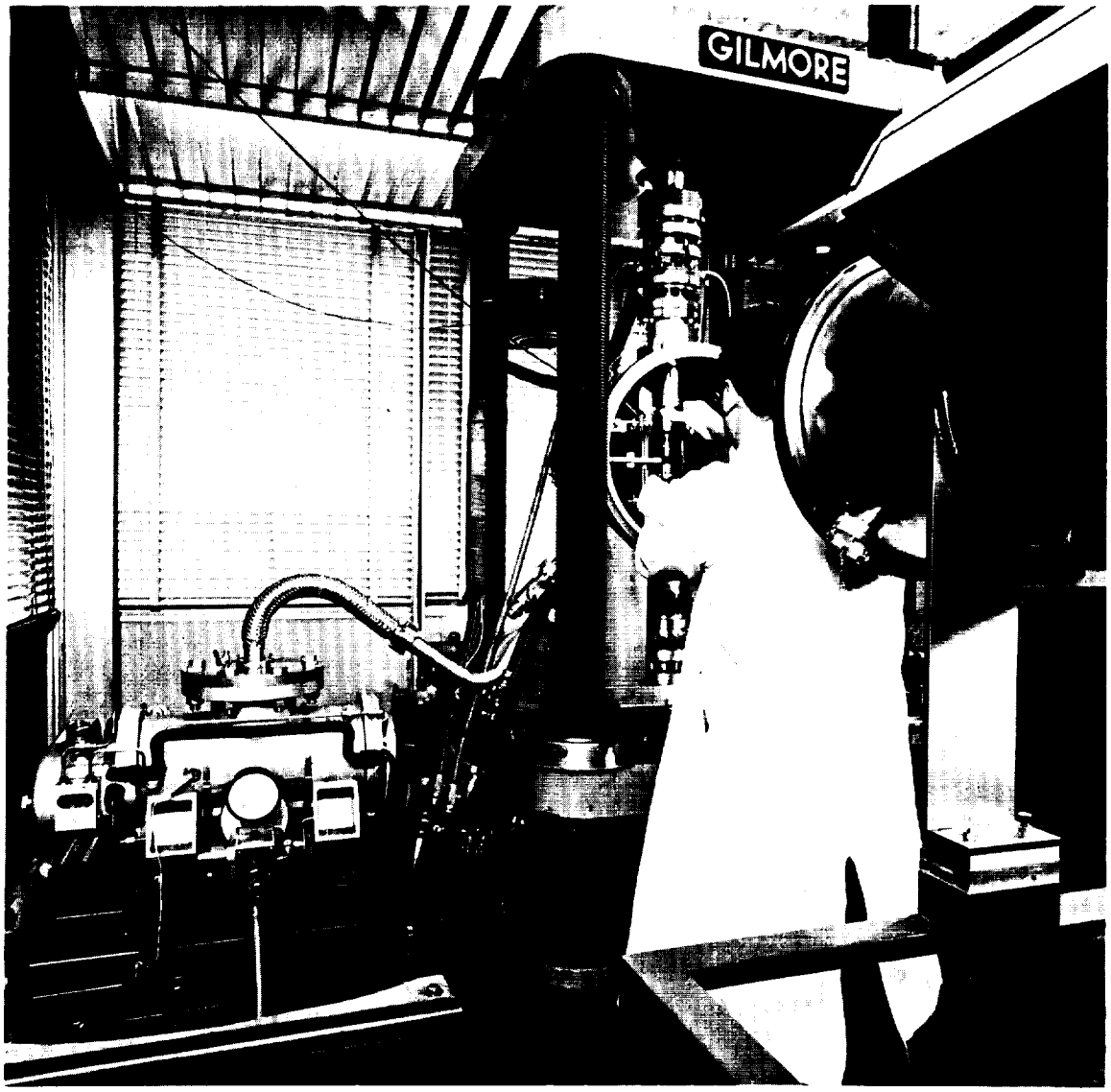

Figure 19. Showing test and pump modules separated for access to test specimen.

The pump module was supported by a movable frame which rolled on rails to facilitate alignment of the main flange during closing the unit. The instrumentation and power supply required for operation of the various pumps and gages were also mounted permanently to this frame. The pump module contained three separate pumping systems. The main system was comprised of four banks of ion pumps having a total pumping capacity of 400 l/second, which was supplemented by titanium sublimation pumping (TSP). The TSP filaments were arranged in three groups of three filaments each, with each set being mounted on a standard 1-1/2" (3.81 mm) UHV flange for convenience in changing filaments. The pump module was also equipped with cryopumping capability, which was not used in this program.

Two vacuum gages were installed on the vacuum system. The first was the ion pumping system itself, which may be used as a relatively crude vacuum gage by measurement of pump current. The second gage was an ionization type gage mounted to the test chamber. Instrumentation for this gage was mounted to the pump module frame, as indicated previously.

The experience gained in using this chamber for low cycle thermal fatigue testing proved it to be a highly satisfactory system, combining good ultimate pressure capability with fast turn around speed. As mentioned previously, the test chamber could be rough pumped to about 1×10^{-4} torr within about 1/2 hour (1800 seconds) after the main flange was torqued closed. This pressure was about one decade lower than can normally be achieved by the more common cryo-sorption type of roughing pump. The mechanically backed turbomolecular roughing system had the additional advantage that it pumped all gasses at more or less the same speed, as opposed to the sorption pump which selectively pumps the more reactive species such as oxygen and nitrogen, leaving the inert gasses relatively enriched in the unpumped residual. Because ion and TSP pumping are also relatively less efficient at pumping inert gasses, selective enrichment of the inerts by sorption pumping significantly reduces subsequent pumping speeds in the high and ultrahigh vacuum ranges.

After roughing to 10^{-4} torr and isolation of the test chamber from the roughing system, the pressure in the test chamber could be dropped almost instantaneously to the low 10^{-6} range by opening of the poppet valve. Working vacuums in the 10^{-8} torr range could be achieved with about 1 to 2 hours of combined ion and TSP pumping, while ultimate pressures in the low 10^{-9} or high 10^{-10} range could be achieved with overnight or longer campaigns. A typical leak rate curve for the 75 liter test chamber is shown in Figure 20. These data, taken from a base pressure of 2.4×10^{-8} torr, show that the leak rate decreased continuously from a value of 2×10^{-5} torr liter/second at blank-lff 3×10^{-7} torr liter/second after 1-1/2 hours (5400 seconds). This diminishing leak rate indicated that the "leak" was primarily an outgassing phenomenon rather than a true air leak, which would exhibit a constant leak rate with time. After 1-1/2 hour of outgassing the chamber approached an equilibrium condition at about 10^{-4} torr, and the leak rate at this pressure would presumably diminish to a very small value at longer times.

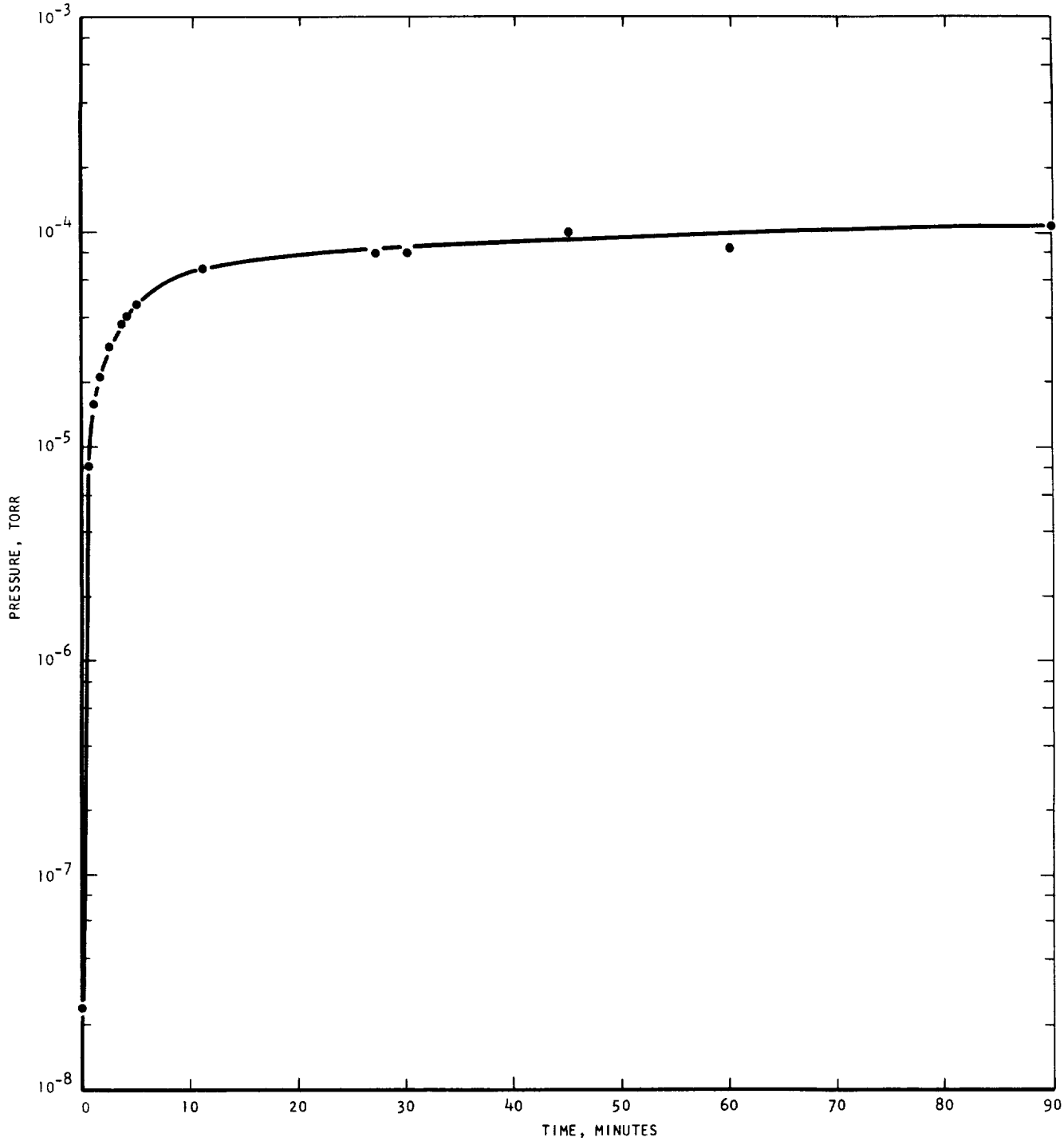

Figure 20. Typical leak-up curve for low cycle thermal fatigue test chamber.

IV PHASE III - TEST PROGRAM

A. Experimental Details

Fatigue tests were performed with closed loop diametral strain control using five basic types of synchronized, independently controlled strain and temperature cycles. The five cycle types employed were isothermal (ISOT), thermal cycled in-phase (TCIP), thermal cycled out-of-phase (TCOP), thermal cycled in-phase square wave (TCIPS) and thermal cycled out-of-phase square wave (TCOPS). In the isothermal cycle temperature was held constant throughout the test, while in the TCIP and TCOP cycles the temperature was varied simultaneously with mechanical strain. In the square wave tests, temperature and strain were changed sequentially so that the tensile and compressive portions of each cycle were executed isothermally, but at different temperatures. Strain versus time, temperature versus time, and strain versus temperature profiles are illustrated in Figure 21 for each of these five cycle types. Variations of the maximum and minimum test temperatures and the test frequency of these five basic cycles were used together with hold times to provide the twelve experimental test cycles described below.

The test program was conducted in two parts. The first part consisted of seven different isothermal, TCIP and TCOP cycles (Table 8) which were applied to both the T-111 and the ASTAR 811C alloys. The second part included five different isothermal, TCIPS and TCOPS cycles (Table 9) which were applied to the ASTAR 811C alloy to provide supplimentary data for the evaluation of thermal fatigue mechanisms. A minimum of four tests were conducted on each test material with each type of cycle to define a curve of strain range versus cycles to failure in the range of 10 to 1000 cycles. A free (zero load) thermal cycle was executed prior to the initiation of each test to measure the exact thermal output of the extensometer, which was used to compensate the strain command signal for direct control of net mechanical strain. Both specimen diameter and temperature versus time, as well as load versus diameter, were measured continuously throughout each test. These data were used together with the previously measured physical properties to calculate the longitudinal elastic and plastic strain ranges as well as the stresses associated with each test. The vacuum test chamber was equipped with a sight port situated so that the surface of the specimen could be observed with a telemicroscope during testing. While it was possible to observe cracks in the surface of the specimen with this arrangement, it was not always possible to define an end point based on crack formation since only one side of the specimen was visible during testing. Failure was therefore defined as complete separation of the specimen into two pieces. After testing, selected samples were subjected to chemical and metallographic analyses. Metallography was performed on polished and etched sections parallel to the tensile axis of the tested specimen using the scanning electron microscope. With the exception of Figure 55, which is a standard light macrograph, all of the macro and micrographs presented in this report were obtained from this instrument.

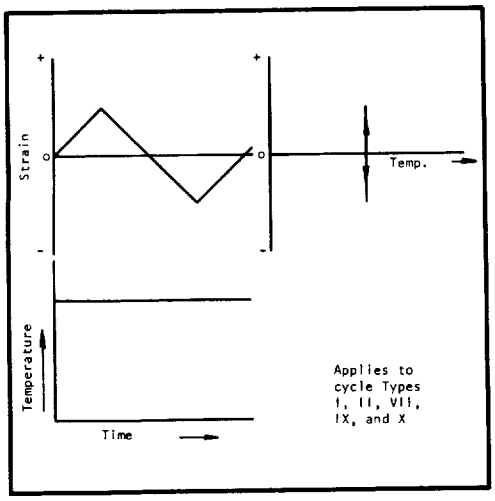

(a) Isothermal

Note: All strains shown represent Net mechanical strain, with thermal expansion subtracted out.

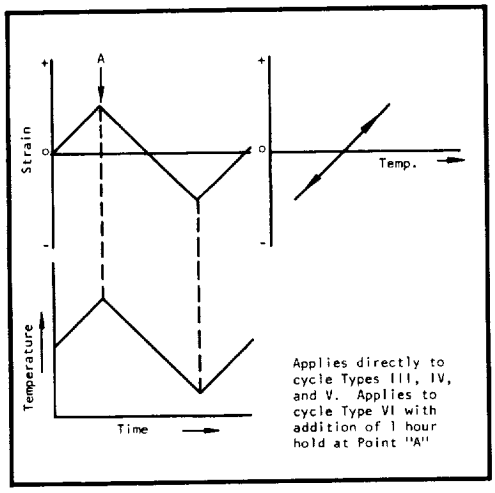

(b) TCIP

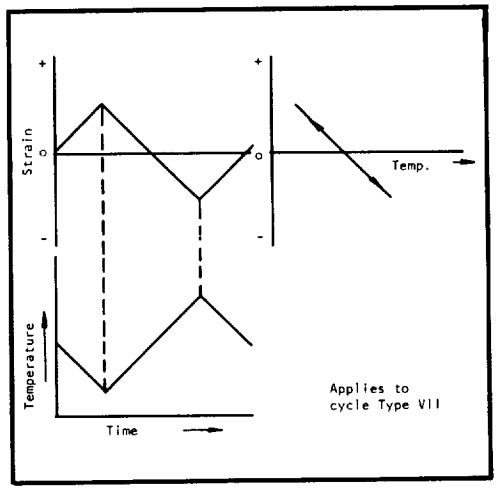

(c) TCOP

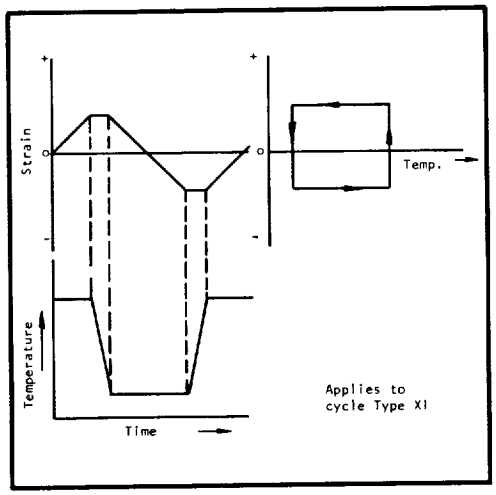

(d) TCIPS

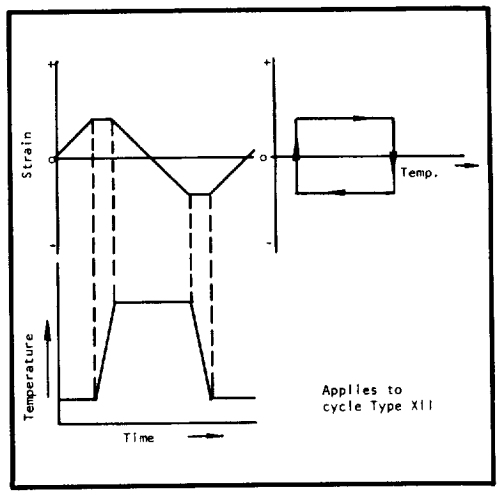

(e) TCOPS

Figure 21. Schematic representation of the five basic types of thermal-mechanical cycles applied in this study.

Table 8

Types of Synchronized Triangular Loading and Heating Cycles
Applied to T-111 and ASTAR 811C Alloys
Test Frequency = .0065 Hz

Cycle Type	Nature of Cycle
I	Isothermal at 2100°F (1422°K)
II	Isothermal at 2100°F (1422°K) with notched test sample. $K_t = 3.$
III	Strain and temperature increasing together with maximum tensile strain at maximum temperature and maximum compressive strain at minimum temperature. Temperature cycled from 400-2100°F (478-1422°K) (TCIP).
IV	As in III, but minimum temperature increased to 900°F (755°K).
V	As in III, with notched test sample, $K_t = 3.$
VI	As in III, but held one hour at 2100°F (1422°K) at maximum tensile strain each cycle. (Designated TCIPH.)
VII	As in III, but maximum compressive strain at maximum test temperature and maximum tensile strain at minimum temperature. (TCOP)

Table 9

Supplimentary Thermal Fatigue Testing of ASTAR 811C Alloy
Test Frequency = .0065 Hz Except as Noted

Cycle Type	Nature of Cycle
VIII	Isothermal at 400°F (478°K).
IX	Isothermal at 1600°F (1144°K).
X	Isothermal at 2100°F (1422°K) test frequency 0.65 Hz. (Designated IHF).
XI	Tension isothermal at 2100°F (1422°K) compression isothermal at 400°F (478°K). (TCIPS)
XII	Tension isothermal at 400°F (478°K) compression isothermal at 2100°F (1422°K). (TCOPS)

B. Test Results

Results of the thermal fatigue testing program will be presented in this section, where the stress response of T-111 and ASTAR 811C to combined temperature and strain cycling will be discussed together with the fatigue life data generated from these tests.

1. Stress Response

Both the T-111 and ASTAR 811C alloys displayed cyclic strain hardening behavior under all types of thermal-mechanical strain cycles applied. Most of the hardening occurred during the first three or four cycles, and a stable loop size was generally developed by about the 10th cycle. In the following discussions of hysteresis loop shape and S/N curves, all stress ranges shown represent the stabilized loop size for each test.

Figure 22 shows the cyclic stress response of the ASTAR 811C alloy to each of the five basic types of thermal mechanical cycles represented in Figure 21. These hysteresis loops are typical of the response observed in both test materials except for the stress levels, which were lower in the lower strength T-111 alloy. Both materials exhibited serrated yielding in the temperature range where dynamic strain aging occurred (Figures 5 and 6); however, this feature was not reproduced in Figure 22 in order to emphasize the basic stress response. Otherwise, the hysteresis loops shown represent values derived directly from the experimental record of load versus diameter for the indicated tests, with thermal expansion substracted out to show true mechanical strain on each curve.

The hysteresis loops in Figure 22 showed the significant influence of thermal cycling on the stress response to cyclic plastic strain. In the isothermal case, Figure 22a, the loop was approximately symmetrical with the peak tensile stress equal to the peak compressive stress and with both stress peaks occurring at the corresponding strain extremes. For the thermal cycled cases, Figure 22b through e, the loops were not symmetrical and the stress and strain peaks were not necessarily coincident. This behavior was the result of increasing material strength with decreasing test temperature, which caused the thermal cycled hysteresis loops to be offset toward the lower temperature portion of the cycle. In the case of the in-phase tests, the compressive stress peak was larger than the tensile peak, while in the out-of-phase tests the opposite was true.

For the square wave tests, where all of the deformation was isothermal, Figure 22d and e, both halves of the hysteresis loop had the form of an isothermal stress strain curve. Peak stress and strain were coincident at both ends of the square wave but with a higher level of peak stress on the cold half of the cycle. The only differences between the tensile and compressive halves of the cycle were the level of the stress

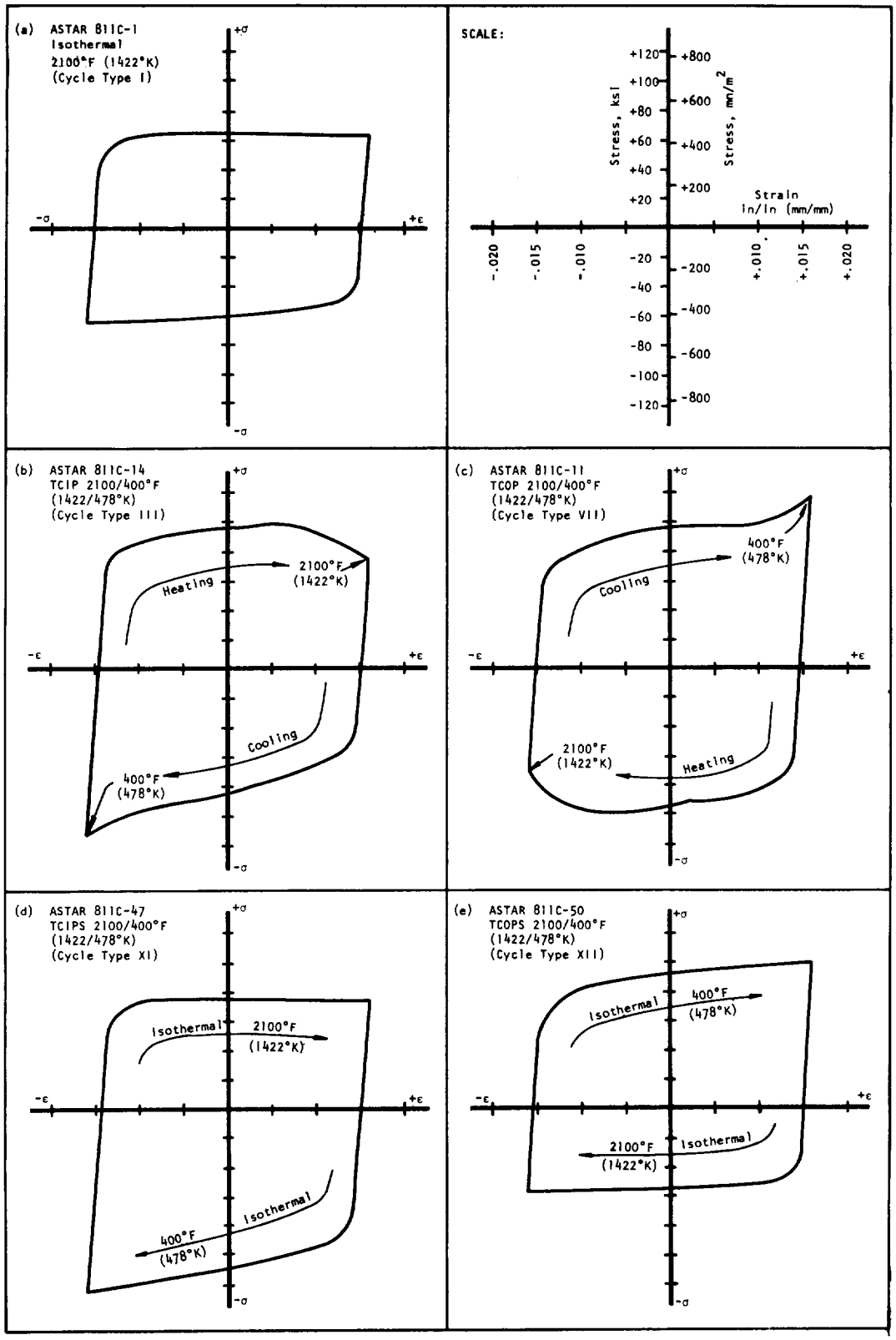

Figure 22. Experimental hysteresis loops for ASTAR 811C alloy tested at a total diametral mechanical strain range of 0.032 in/in (mm/mm) (approximately 0.066 in/in (mm/mm) longitudinal strain).

3396 c

and the amount of monotonic strain hardening (that is, the slope of the plastic portion of the curve). Monotonic hardening was observed only at the lower test temperatures, with the high temperature flow occurring at relatively constant stress levels.

For the tests where temperature was varied simultaneously with strain (TCIP and TCOP curves, Figures 22b and c) the shape of the loop reflected the effects of both monotonic hardening and changing temperature on flow stress. In the half of the cycle where the specimen was cooling, both thermal and monotonic hardening increased together so that the peak stress was coincident with the maximum strain excursion. However, for the half of the cycle where temperature was increasing, the two effects worked in opposite directions with strain hardening tending to increase the flow stress at the same time as the increasing temperature was softening the material. During the early portion of the heated half cycle strain hardening predominated, causing the flow stress to increase with the accumulation of reversed plastic strain. However, the increasing temperature eventually caused the rate of strain hardening to decrease so that during the latter portions of the heated half-cycle thermal effects predominated, causing the stress to decrease with further accumulations of plastic strain. The simultaneous operation of these two opposing effects thus caused the stress to peak in the middle rather than at the end of the heated strain excursion. The previously mentioned dynamic strain aging also had some effect on the shapes of the TCIP and TCOP hysteresis loops (in addition to the previously mentioned serrations). This effect was more pronounced in the heating than in the cooling half of the loop, and was manifest as a tendency for the curve to flatten out in the 1200-1300°F (922-978°K) temperature range, followed by an increase in stress in the 1500-1600°F (1089-1144°K) range where the dynamic aging phenomenon was most prominent. Because of this effect, the stress peak was consistently found to be in the 1500-1600°F (922-978°K) range on the heated half of all of the TCIP and TCOP tests conducted in this study.

2. Fatigue Life Data

Fatigue life results are presented in Tables 10 and 11, where cycles to failure are listed together with the stress and strain ranges and the experimental parameters for each test. Because of the assymetric nature of the thermal cycled hysteresis loops, it was necessary to tabulate both a tensile and a compressive stress component for each test. Also, both the maximum (peak) stress and the stress at the extreme strain excursion (terminal stress) were tabulated for those tests where temperature and strain were varied simultaneously because the stress and strain extremes did not coincide on the heating half of the test cycle. The peak range shown for each test was the sum of the maximum tensile and maximum compressive stress experienced in each cycle. These stress values were used for preparation of the S-N curves, while the terminal stress values were used for the separation of elastic and plastic strain components discussed below.

Table 10

T-111 Alloy Low Cycle Thermal-Mechanical Fatigue Test Results

Test No.	Specimen Geometry	Test Type	Cycle Type	Test Temperature Upper °F	Upper °K	Lower °F	Lower °K	Diametral Strain Range in/in (mm/mm) Elastic	Plastic	Total	Longitudinal Strain Range in/in (mm/mm) Elastic	Plastic	Total	Stress, psi Tensile Peak	Tensile Terminal	Compressive Peak	Compressive Terminal	Peak Range	Stress, mn/m^2 Tensile Peak	Tensile Terminal	Compressive Peak	Compressive Terminal	Peak Range	Cycles to Failure
T-17	Smooth	ISOT	I	2100	1422	-	-	.00138	.06262	.06400	.00564	.12524	.13088	-	64,100	-	64,200	128,300	-	442	-	442	884	10
T-15	Smooth	ISOT	I	2100	1422	-	-	.00117	.03083	.03200	.00476	.06166	.06642	-	54,000	-	54,300	108,300	-	372	-	374	746	41
T-14	Smooth	ISOT	I	2100	1422	-	-	.00106	.01494	.01600	.00431	.02988	.03419	-	49,000	-	49,000	98,000	-	338	-	338	675	173
T-16	Smooth	ISOT	I	2100	1422	-	-	.00100	.00700	.00800	.00410	.01400	.01810	-	46,500	-	46,700	93,200	-	320	-	322	642	796
T-19	Notched	ISOT	II	2100	1422	-	-	.00122	.03078	.03200	.00496	.06156	.06652	-	56,600	-	56,300	112,900	-	390	-	388	778	13
T-18	Notched	ISOT	II	2100	1422	-	-	.00103	.01497	.01600	.00422	.02994	.03416	-	46,900	-	49,000	95,900	-	323	-	338	661	40
T-20	Notched	ISOT	II	2100	1422	-	-	.00089	.00711	.00800	.00364	.01422	.01786	-	41,100	-	41,800	82,900	-	283	-	288	571	258
T-21	Notched	ISOT	II	2100	1422	-	-	.00075	.00325	.00400	.00305	.00650	.00955	-	34,500	-	35,000	69,500	-	238	-	241	479	900
T-22	Smooth	TCIP	III	2100	1422	400	478	.00154	.03046	.03200	.00621	.06092	.06713	74,700	57,000	-	95,000	169,700	515	393	-	655	1169	10
T-23	Smooth	TCIP	III	2100	1422	400	478	.00147	.01453	.01600	.00588	.02906	.03494	69,900	58,100	-	85,700	155,600	482	400	-	590	1072	15
T-25	Smooth	TCIP	III	2100	1422	400	478	.00136	.01064	.01200	.00547	.02128	.02675	65,000	54,600	-	78,800	143,800	448	376	-	543	991	19
T-26	Smooth	TCIP	III	2100	1422	400	478	.00130	.00670	.00800	.00523	.01340	.01863	57,700	51,500	-	76,300	134,000	398	355	-	526	923	35
T-27	Smooth	TCIP	III	2100	1422	400	478	.00122	.00278	.00400	.00487	.00556	.01053	47,200	45,200	-	74,100	121,300	325	311	-	511	836	108
T-28	Smooth	TCIP	III	2100	1422	400	478	.00118	.00082	.00200	.00476	.00164	.00640	43,000	43,000	-	73,700	116,700	296	296	-	508	804	456
T-32	Smooth	TCOP	VII	2100	1422	400	478	.00179	.06221	.06400	.00719	.12442	.13161	-	98,100	83,200	76,700	181,300	-	676	573	528	1249	4
T-33	Smooth	TCOP	VII	2100	1422	400	478	.00182	.04618	.04800	.00730	.09236	.09966	-	100,900	82,900	76,700	183,800	-	695	571	528	1266	9
T-34	Smooth	TCOP	VII	2100	1422	400	478	.00172	.03828	.04000	.00693	.07656	.08349	-	95,800	80,900	72,700	176,700	-	660	557	501	1217	21
T-29	Smooth	TCOP	VII	2100	1422	400	478	.00180	.03020	.03200	.00725	.06040	.06765	-	101,300	82,300	75,200	183,600	-	698	567	518	1265	144
T-35	Smooth	TCOP	VII	2100	1422	400	478	.00164	.02236	.02400	.00657	.04472	.05129	-	92,300	74,000	67,700	166,300	-	636	510	466	1146	256
T-30	Smooth	TCOP	VII	2100	1422	400	478	.00169	.01431	.01600	.00679	.02862	.03541	-	99,600	73,900	66,300	165,900	-	686	509	457	1143	567
T-39	Notched	TCIP	V	2100	1422	400	478	.00140	.01460	.01600	.00562	.02920	.03482	65,800	54,000	-	83,600	149,400	453	372	-	576	1029	16
T-38	Notched	TCIP	V	2100	1422	400	478	.00131	.00669	.00800	.00526	.01338	.01864	58,300	50,200	-	78,300	136,600	402	346	-	539	941	36
T-36	Notched	TCIP	V	2100	1422	400	478	.00126	.00274	.00400	.00504	.00548	.01052	50,450	48,900	-	77,400	127,850	348	337	-	533	881	86
T-37	Notched	TCIP	V	2100	1422	400	478	.00111	.00089	.00200	.00455	.00178	.00623	41,000	39,200	-	70,200	111,200	282	270	-	484	766	263
T-41	Smooth	TCIP	IV	2100	1422	900	755	.00138	.01462	.01600	.00567	.02924	.03491	67,900	60,200	-	74,300	142,200	468	415	-	512	978	15
T-40	Smooth	TCIP	IV	2100	1422	900	755	.00113	.00687	.00800	.00467	.01374	.01841	58,800	49,000	-	67,400	126,200	405	338	-	464	870	24
T-42	Smooth	TCIP	IV	2100	1422	900	755	.00117	.00283	.00400	.00483	.00566	.01049	53,300	51,400	-	63,100	116,400	367	354	-	435	802	94
T-43	Smooth	TCIP	IV	2100	1422	900	755	.00106	.00094	.00200	.00439	.00188	.00627	47,100	45,000	-	59,400	106,500	325	310	-	409	734	248
T-45	Smooth	TCIPH	VI	2100	1422	400	478	.00125	.01475	.01600	.00500	.02950*	.03450	61,700	49,800*	-	72,300	134,000	425	343	-	498	923	14
T-44	Smooth	TCIPH	VI	2100	1422	400	478	.00104	.00696	.00800	.00416	.01392*	.01808	49,300	37,000*	-	64,900	114,200	340	255	-	447	787	27
T-46	Smooth	TCIPH	VI	2100	1422	400	478	.00107	.00293	.00400	.00429	.00586*	.01015	47,200	39,000*	-	66,400	113,600	325	269	-	457	783	40
T-47	Smooth	TCIPH	VI	2100	1422	400	478	.00099	.00101	.00200	.00400	.00202*	.00602	38,900	34,800*	-	63,400	102,300	268	240	-	437	705	139

* Note: Values shown represent measured tensile stress and calculated plastic strain immediately upon termination of the fatigue cycle. Values observed after 1 hour hold at constant temperature and total strain are as follows:

Specimen No.	Longitudinal Plastic Stress in/in (mm/mm)	Creep Stress Accumulated in 1 hour in/in (mm/mm)	Tensile Stress ksi	Tensile Stress mn/m^2
T-45	.03060	.00110	24,900	172
T-44	.01464	.00072	20,600	142
T-46	.00658	.00072	22,600	156
T-47	.00260	.00058	21,700	149

Table 11

ASTAR 811C Alloy Low Cycle Thermal-Mechanical Fatigue Test Results

Test No.	Specimen Geometry	Test Type	Cycle Type	Test Temperature Upper °F	Test Temperature Upper °K	Test Temperature Lower °F	Test Temperature Lower °K	Diametral Strain Range in/in (mm/mm) Elastic	Diametral Strain Range in/in (mm/mm) Plastic	Diametral Strain Range in/in (mm/mm) Total	Longitudinal Strain Range in/in (mm/mm) Elastic	Longitudinal Strain Range in/in (mm/mm) Plastic	Longitudinal Strain Range in/in (mm/mm) Total	Stress, psi Tensile Peak	Stress, psi Tensile Terminal	Stress, psi Compressive Peak	Stress, psi Compressive Terminal	Stress, psi Peak Range	Stress, mn/m^2 Tensile Peak	Stress, mn/m^2 Tensile Terminal	Stress, mn/m^2 Compressive Peak	Stress, mn/m^2 Compressive Terminal	Stress, mn/m^2 Peak Range	Cycles to Failure
A-3	Smooth	ISOT	I	2100	1422	-	-	.00200	.12600	.12800	.00666	.25200	.25870	-	81,500	-	79,800	161,300	-	562	-	550	1111	7
A-2	Smooth	ISOT	I	2100	1422	-	-	.00181	.06219	.06400	.00604	.12438	.13042	-	73,200	-	73,300	146,500	-	504	-	505	1009	39
A-1	Smooth	ISOT	I	2100	1422	-	-	.00160	.03040	.03200	.00533	.06080	.06610	-	64,600	-	64,600	129,200	-	445	-	445	890	117
A-6	Smooth	ISOT	I	2100	1422	-	-	.00151	.01449	.01600	.00504	.02898	.03442	-	61,000	-	61,100	122,100	-	420	-	421	841	628
A-5	Notched	ISOT	II	2100	1422	-	-	.00214	.12586	.12800	.00713	.25172	.25885	-	86,500	-	86,300	172,800	-	596	-	595	1191	6
A-4	Notched	ISOT	II	2100	1422	-	-	.00178	.06222	.06400	.00592	.12444	.13036	-	71,500	-	71,800	143,300	-	493	-	495	987	25
A-7	Notched	ISOT	II	2100	1422	-	-	.00142	.03058	.03200	.00475	.06116	.06591	-	60,000	-	59,900	119,900	-	413	-	413	826	106
A-8	Notched	ISOT	II	2100	1422	-	-	.00127	.01473	.01600	.00425	.02946	.03371	-	51,500	-	51,400	102,900	-	355	-	354	709	312
A-24	Smooth	TCIP	III	2100	1422	400	478	.00255	.06145	.06400	.00788	.12290	.13078	106,800	80,600	-	131,300	238,100	736	555	-	905	1641	13
A-14	Smooth	TCIP	III	2100	1422	400	478	.00224	.02976	.03200	.00696	.05952	.06648	97,500	73,800	-	112,900	210,400	672	508	-	778	1450	32
A-15	Smooth	TCIP	III	2100	1422	400	478	.00206	.01394	.01600	.00590	.02788	.03378	88,500	67,200	-	104,400	192,900	610	463	-	719	1329	132
A-16	Smooth	TCIP	III	2100	1422	400	478	.00184	.00616	.00800	.00567	.01232	.01799	69,000	55,600	-	97,400	166,400	475	383	-	671	1146	367
A-17	Smooth	TCIP	III	2100	1422	400	478	.00153	.00247	.00400	.00465	.00494	.00959	57,400	36,000	-	91,600	149,000	395	141	-	631	1027	939
A-9	Smooth	TCOP	VII	2100	1422	400	478	.00261	.06139	.06400	.00810	.12278	.13088	-	130,700	106,900	86,400	237,600	-	901	737	595	1637	15
A-11	Smooth	TCOP	VII	2100	1422	400	478	.00225	.02975	.03200	.00697	.05950	.06647	-	116,000	98,400	71,300	214,400	-	799	678	491	1477	61
A-21	Smooth	TCOP	VII	2100	1422	400	478	.00206	.01394	.01600	.00637	.02788	.03425	-	112,000	87,200	60,200	199,200	-	772	601	415	1372	365
A-12	Smooth	TCOP	VII	2100	1422	400	478	.00185	.00615	.00800	.00569	.01230	.01799	-	98,800	68,000	59,800	166,800	-	681	469	378	1149	1012
A-18	Notched	TCIP	V	2100	1422	400	478	.00238	.06162	.06400	.00741	.12324	.13065	109,700	76,300	-	122,800	232,500	756	526	-	846	1602	8
A-19	Notched	TCIP	V	2100	1422	400	478	.00229	.02971	.03200	.00709	.05942	.06651	101,700	71,700	-	118,800	220,500	701	494	-	819	1519	19
A-23	Notched	TCIP	V	2100	1422	400	478	.00201	.01399	.01600	.00623	.02798	.03421	86,400	66,400	-	100,400	186,800	595	457	-	692	1287	82
A-22	Notched	TCIP	V	2100	1422	400	478	.00184	.00616	.00800	.00571	.01232	.01803	71,000	61,700	-	91,300	162,300	489	425	-	629	1118	284
A-20	Notched	TCIP	V	2100	1422	400	478	.00165	.00235	.00400	.00510	.00470	.00980	58,600	53,500	-	83,500	142,100	404	368	-	575	979	711
A-28	Smooth	TCIP	IV	2100	1422	900	755	.00222	.02978	.03200	.00690	.05956	.06646	98,300	74,700	-	106,900	205,200	677	515	-	737	1414	22
A-26	Smooth	TCIP	IV	2100	1422	900	755	.00197	.01403	.01600	.00612	.02806	.03418	86,400	68,500	-	92,400	178,800	595	472	-	637	1232	87
A-27	Smooth	TCIP	IV	2100	1422	900	755	.00173	.00627	.00800	.00541	.01254	.01795	69,800	60,900	-	81,100	150,900	481	420	-	559	1040	226
A-29	Smooth	TCIP	IV	2100	1422	900	755	.00172	.00228	.00400	.00538	.00456	.00994	65,600	61,600	-	79,400	145,000	452	424	-	547	999	986
A-34	Smooth	TCIPH	VI	2100	1422	400	478	.00207	.06193	.06400	.00643	.12386*	.13029	100,400	68,800*	-	103,300	204,000	692	474	-	712	1406	6
A-32	Smooth	TCIPH	VI	2100	1422	400	478	.00219	.02981	.03200	.00681	.05962*	.06643	93,400	75,900*	-	106,100	199,500	644	523	-	731	1375	27
A-33	Smooth	TCIPH	VI	2100	1422	400	478	.00167	.01433	.01600	.00515	.02866*	.03381	77,000	53,900*	-	84,300	161,300	531	371	-	581	1111	81
A-57	Smooth	TCIPH	VI	2100	1422	400	478	.00159	.00641	.00800	.00495	.01282*	.01777	76,000	54,500*	-	76,800	157,800	524	376	-	529	1087	178
A-36	Smooth	ISOT	VIII	400	478	-	-	.00301	.12499	.12800	.00886	.24998	.25884	-	135,300	-	116,200	251,500	-	932	-	801	1733	5
A-31	Smooth	ISOT	VIII	400	478	-	-	.00303	.06097	.06400	.00890	.12194	.13084	-	130,000	-	122,900	252,900	-	896	-	847	1742	26
A-35	Smooth	ISOT	VIII	400	478	-	-	.00274	.02926	.03200	.00806	.05852	.06658	-	116,000	-	113,000	229,000	-	799	-	779	1578	81
A-30	Smooth	ISOT	VIII	400	478	-	-	.00239	.01361	.01600	.00703	.02722	.03425	-	99,500	-	100,200	199,700	-	686	-	690	1376	406
A-42	Smooth	ISOT	IX	1600	1144	-	-	.00320	.12480	.12800	.01017	.24960	.25977	-	135,000	-	119,500	254,500	-	930	-	823	1754	5
A-41	Smooth	ISOT	IX	1600	1144	-	-	.00274	.06126	.06400	.00871	.12252	.13123	-	108,900	-	109,200	218,100	-	750	-	752	1503	18
A-39	Smooth	ISOT	IX	1600	1144	-	-	.00225	.02975	.03200	.00713	.05950	.06663	-	89,300	-	89,100	178,400	-	615	-	614	1229	111
A-40	Smooth	ISOT	IX	1600	1144	-	-	.00196	.01404	.01600	.00662	.02808	.03470	-	84,500	-	81,200	165,700	-	582	-	559	1142	696
A-44	Smooth	IHF	X	2100	1422	-	-	.00252	.06148	.06400	.00840	.12296	.13136	-	106,000	-	97,800	203,800	-	730	-	674	1404	40
A-43	Smooth	IHF	X	2100	1422	-	-	.00193	.03007	.03200	.00642	.06014	.06656	-	78,000	-	77,300	155,300	-	537	-	533	1070	266
A-45	Smooth	IHF	X	2100	1422	-	-	.00169	.01431	.01600	.00564	.02862	.03426	-	69,300	-	67,300	136,600	-	477	-	464	941	872
A-55	Smooth	IHF	X	2100	1422	-	-	.00144	.00656	.00800	.00479	.01312	.01791	-	57,500	-	58,800	116,000	-	396	-	405	799	1952
A-46	Smooth	IHF	X	2100	1422	-	-	.00145	.00655	.00800	.00484	.01310	.01794	-	58,400	-	58,800	117,200	-	402	-	405	808	2010
A-48	Smooth	TCIPS	XI	2100	1422	400	478	.00269	.06131	.06400	.00833	.12262	.13095	-	87,200	-	134,200	221,400	-	601	-	925	1525	6
A-47	Smooth	TCIPS	XI	2100	1422	400	478	.00242	.02958	.03200	.00748	.05916	.06664	-	75,200	-	124,600	199,800	-	518	-	858	1377	20
A-49	Smooth	TCIPS	XI	2100	1422	400	478	.00217	.01383	.01600	.00671	.02766	.03437	-	68,400	-	110,400	178,800	-	471	-	761	1232	47
A-52	Smooth	TCIPS	XI	2100	1422	400	478	.00198	.00602	.00800	.00613	.01204	.01817	-	63,700	-	99,300	163,000	-	439	-	684	1123	170
A-51	Smooth	TCIPS	XI	2100	1422	400	478	.00184	.00216	.00400	.00569	.00432	.01001	-	59,600	-	91,600	151,200	-	411	-	631	1042	335
A-53	Smooth	TCOPS	XII	2100	1422	400	478	.00206	.06194	.06400	.00633	.12388	.13021	-	111,100	-	59,400	170,500	-	765	-	409	1175	7
A-50	Smooth	TCOPS	XII	2100	1422	400	478	.00190	.03010	.03200	.00587	.06020	.06607	-	99,300	-	57,500	156,800	-	684	-	396	1080	40
A-54	Smooth	TCOPS	XII	2100	1422	400	478	.00184	.01416	.01600	.00568	.02832	.03400	-	95,300	-	56,200	151,500	-	657	-	387	1044	141
A-56	Smooth	TCOPS	XII	2100	1422	400	478	.00171	.00629	.00800	.00529	.01258	.01787	-	88,400	-	52,700	141,100	-	609	-	363	972	738

* Note: Values shown represent measured tensile stress and calculated plastic strain immediately upon termination of the fatigue cycle. Values observed after 1 hour hold at constant temperature and total strain are as follows:

Specimen No.	Longitudinal Plastic Strain in/in (mm/mm)	Creep Strain Accumulation 1 hour in/in (mm/mm)	Tensile Stress ksi	Tensile Stress mn/n^2
A-34	.12562	.00176	26,100	180
A-32	.06188	.00226	21,100	145
A-33	.03020	.00154	16,600	114
A-57	.01417	.00135	21,800	150

Six strain ranges were tabulated for each test in Tables 10 and 11. The total diametral strain range was the experimentally applied independent variable and was calculated by dividing net diameter excursion (total diameter change less the measured thermal expansion) for each test by the original specimen diameter. The other five strain ranges were calculated from the experimentally observed stress ranges as follows. The longitudinal elastic strain range was the sum of the tensile and compressive longitudinal elastic strains at the tensile and compressive strain extremes, which were calculated using the observed terminal tensile and compressive stress values together with the previously measured longitudinal elastic modulus values corresponding to the measured values of specimen temperature at two points of strain reversal (Figure 4). The diametral elastic strain range was the sum of the tensile and compressive diametral elastic strain components, which were calculated from the corresponding longitudinal elastic strain components using the previously measured value of Poisson's ratio corresponding to the temperature at each strain reversal (Figure 4). The diametral plastic strain range was calculated by direct subtraction of the calculated diametral elastic strain range from the experimentally imposed total diametral strain range. The calculated diametral plastic strain range was doubled to obtained the longitudinal plastic strain range, which was added to the previously calculated longitudinal elastic strain range to obtain the values of total longitudinal strain range shown in Tables 10 and 11. The effect of these various strain components on fatigue life will be discussed in subsequent paragraphs.

The influence of the various types of thermal-mechanical strain cycles on the fatigue life of the T-111 and ASTAR 811C alloys is shown in Figures 23-50, where fatigue life curves are drawn for each cycle type as a function of stress range, longitudinal plastic strain range, and longitudinal total strain range. The experimental data showed greater scatter when correlated with stress range than when correlated with either plastic or total strain range. This is not an unusual observation for strain controlled testing where strain is an independent variable and stress is a dependent variable. Both the plastic and total strain range correlated well with fatigue life, with no significant advantage being noted for either type of plot. The reason for this was that relatively large strain amplitudes were required to provide failure in the desired range of 10 to 1000 cycles, so that the majority of the cyclic deformation was plastic and the difference between plastic and total strain was relatively small for most of the tests conducted.

3. T-111 Alloy Behavior

The isothermal results for T-111 alloy tested at 2100°F (1422°K) are shown in Figures 23 and 24. The S-N curve for this data (Figure 23) displayed the typical concave upward shape, while both strain range plots (Figure 24) showed an essentially linear dependence of log fatigue life on log strain range. Also shown in Figure 24 are predictions of the fatigue

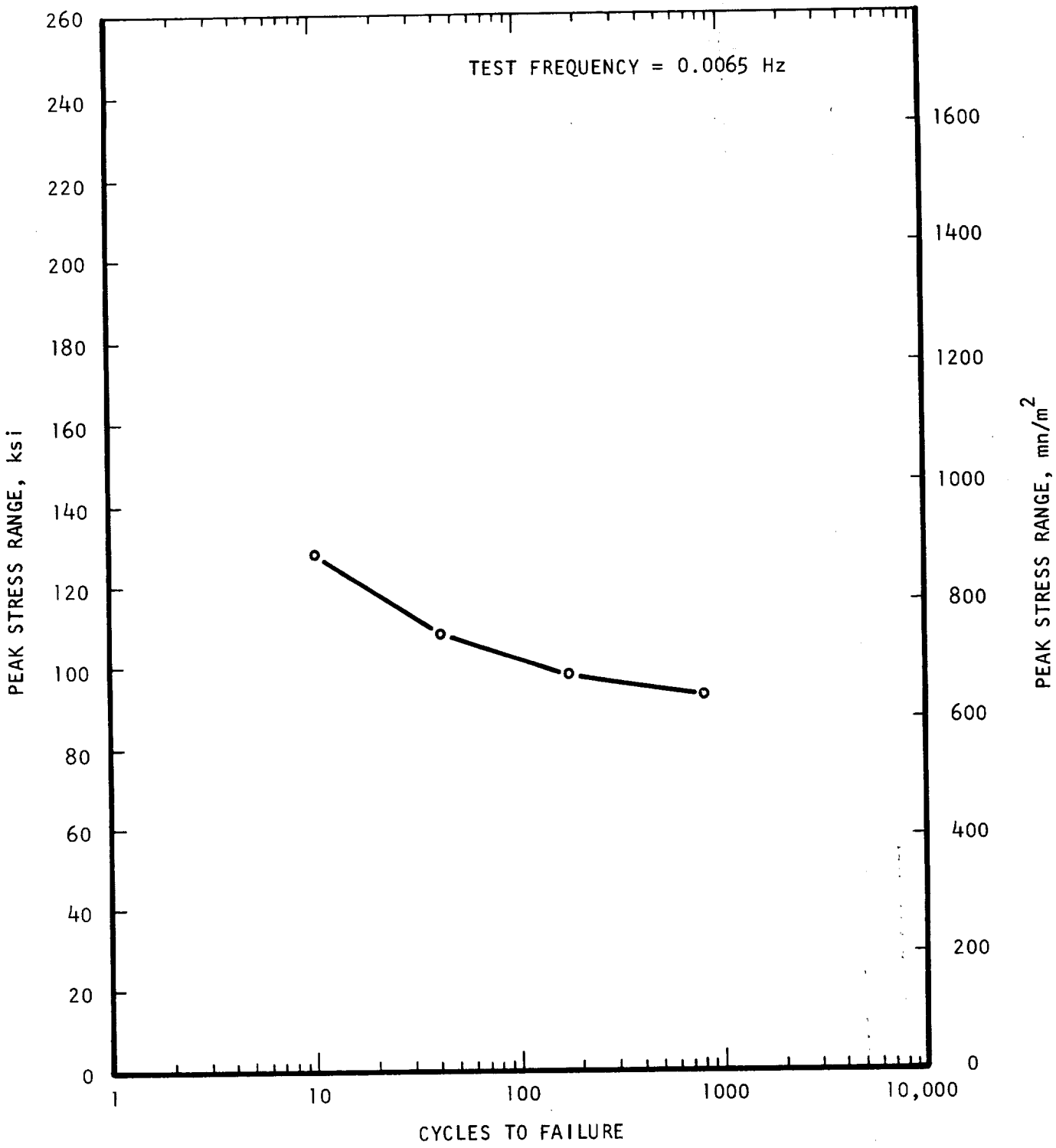

Figure 23. S/N curve for T-111 alloy tested isothermally at 2100°F (1422°K) (cycle type 1).

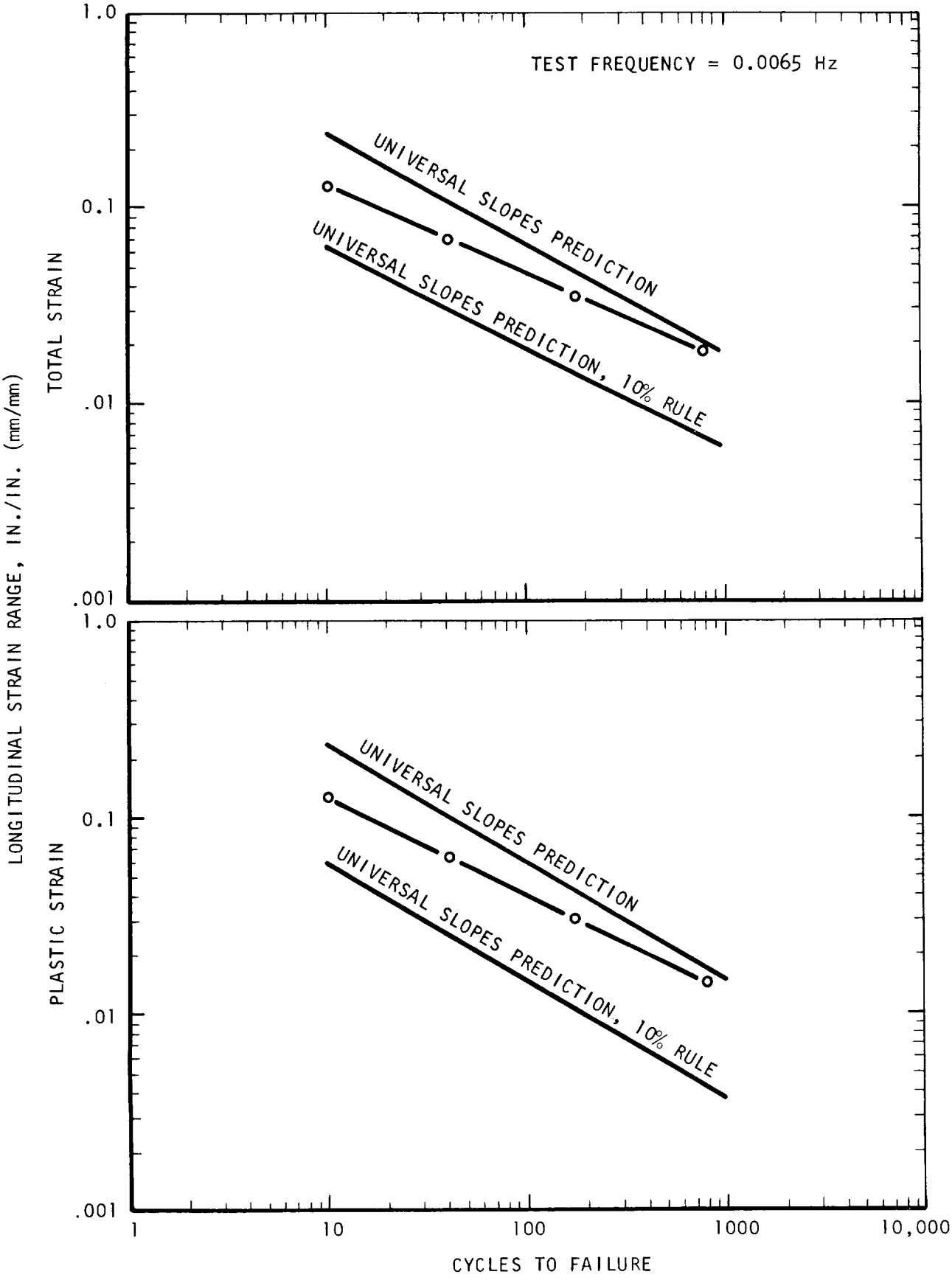

Figure 24. Influence of strain range on the fatigue life of T-111 alloy tested isothermally at 2100°F (1422°K) (cycle type 1).

life for the T-111 alloy based on the method of universal slopes. These predictions, which were calculated from the elevated temperature tensile data shown in Figure 5, bracket the experimental data within the range of applied strains. This is the expected behavior, since the direct Universal slopes prediction was developed for low temperature applications, and should provide an upper bound for high temperature data, while the 10% rule was proposed to provide a lower bound for temperature effects on fatigue life. The fact that the observed lives were consistently below the direct prediction line suggests that creep effects were involved in the isothermal fatigue process at 2100°F (1422°K).

In order to provide some perspective concerning the overall fatigue behavior of the T-111 alloy, the 2100°F (1422°K) isothermal data generated on this program were compared with 2000°F (1366°K) high cycle fatigue data generated on recrystallized T-111 alloy in ultrahigh vacuum on a previous program conducted in this laboratory (4) (Figure 25). This comparison must be interpreted with some caution, since the high frequency tests were conducted at a different temperature and with a mean stress present (A ratios ranging from .25 to .45), and at a drastically different frequency (~20kHz). However, it does provide some basis for characterization of the general level of elevated temperature fatigue resistance of the T-111 alloy over a wide range of cycles-to-failure, and would provide a good point of departure for a more detailed study of the T-111 fatigue behavior in the intermediate life range.

The influence of in-phase thermal cycling on the fatigue life of T-111 is shown in Figures 26 and 27. This type of cycle had a very pronounced detrimental influence on the fatigue life of the T-111 alloy, with the TCIP life being reduced in some cases by more than a factor of 10 over the isothermal life at the highest temperature of the thermal cycle (Figure 26). As an example of this effect, tests conducted at a total longitudinal strain range of approximately .018 (tests T-16 and T-26, Table 11) showed a fatigue life 796 cycles isothermally at 2100°F (1422°K) as compared to a life of only 35 cycles when the temperature was cycled from 2100°F (1422°K) to 400°F (478°K) in-phase with the mechanical strain (heating with tension, cooling with compression). The life reductions caused by in-phase thermal cycling were large enough to lower the TCIP curve below the Universal slopes 10% line, which is particularly important because it means that the thermal cycling effect represented a serious non-conservative strength degradation which could not have been predicted using any of the existing isothermal fatigue or creep-fatigue theories. Thus, a thorough analysis of the thermal cycled fatigue behavior is required to determine the cause of this degradation effect so that the possibility of similar strength reductions in other materials may be anticipated.

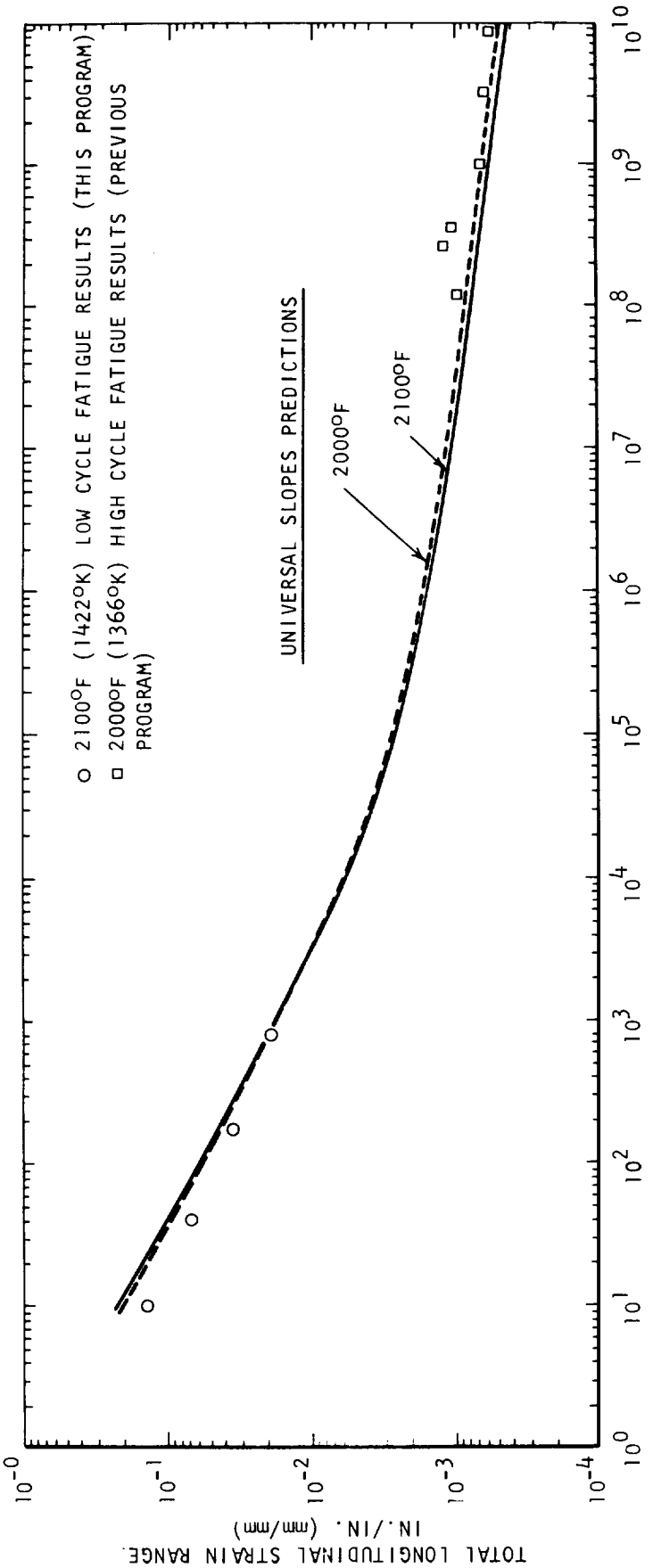

Figure 25. Comparison of low cycle and high cycle fatigue results for T-111 alloy.

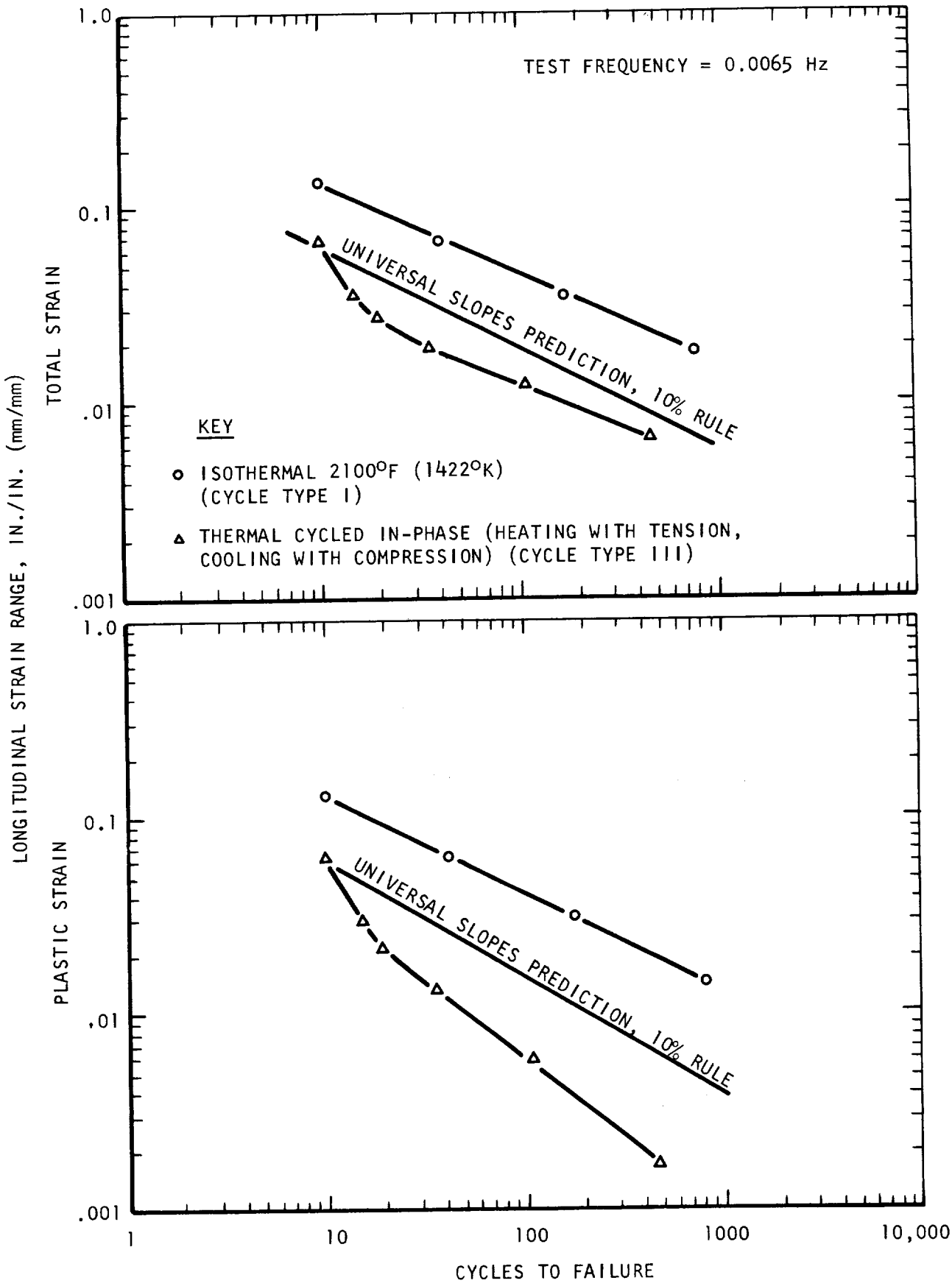

Figure 26. Influence of strain range on the fatigue life of T-111 alloy tested with the indicated types of thermal-mechanical cycling.

3398 c

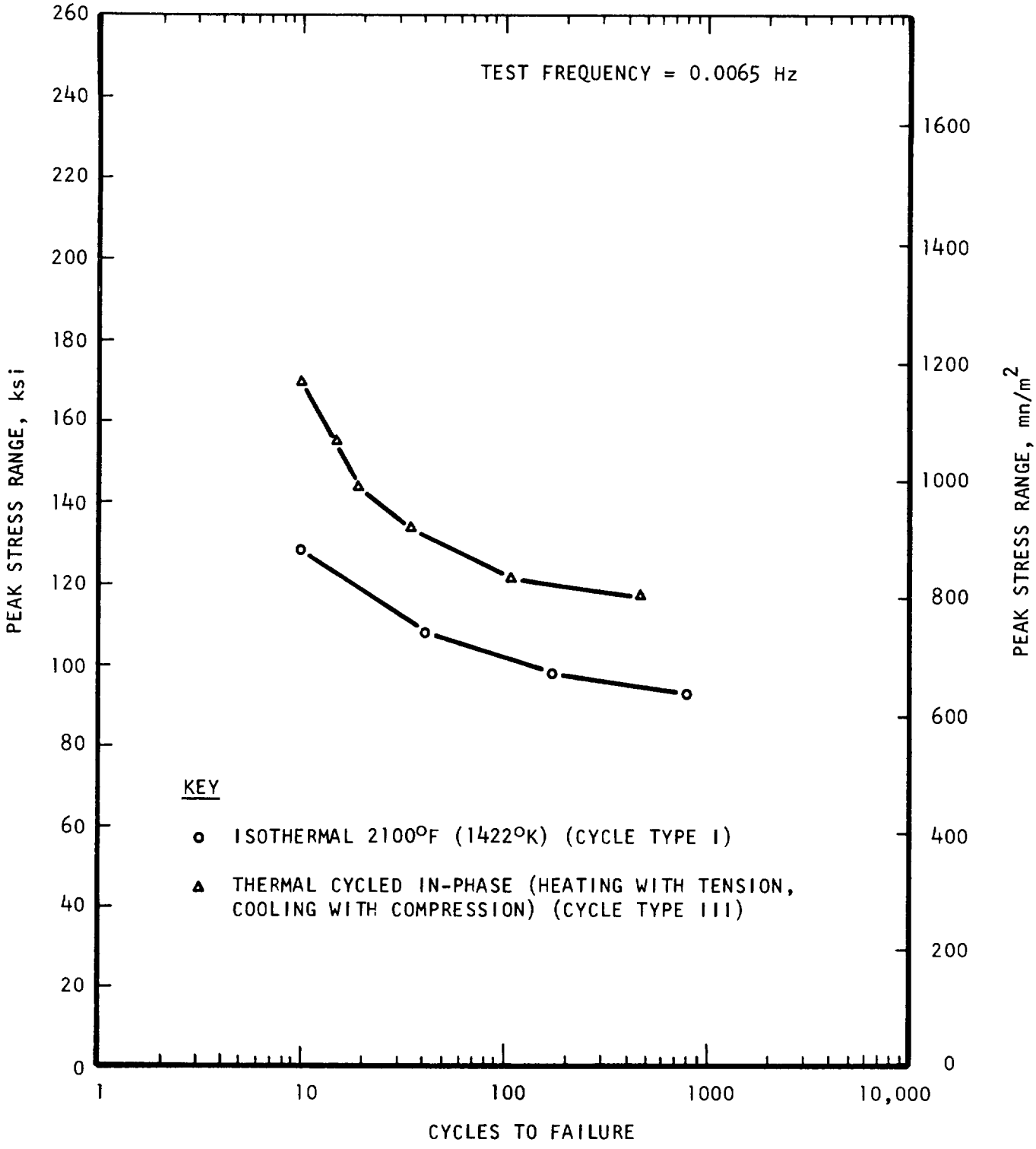

Figure 27. S/N curves for T-111 alloy tested with the indicated types of thermal-mechanical cycling.

The S-N curve for the TCIP cycle (Figure 27) showed significantly higher stresses in this type of test as a result of the higher material strength at the lower temperatures. However, the low temperature deformation caused very little additional cyclic strain hardening as shown in Figure 28, where the peak tensile stress in the 2100°F (1422°K) isothermal tests is compared with the terminal tensile stress at 2100°F (1422°K) in the TCIP type test.

The data presented in Figures 29 and 30 showed that the presence of a notch had a significant effect on the isothermal life, but only a minimal effect on the TCIP results in the T-111 alloy. Visual observation of the notched specimens during testing indicated that a fatigue crack was initiated at the notch root within the first few cycles in all of the notched tests, so that this type of test provided an effective means for separation of the initiation and propagation stages of the fatigue life. These results thus showed that the thermal cycled life degradation effect involved more than premature crack initiaion, since the TCIP results were significantly below the isothermal notched data.

The influence of changes in the cycle parameters for the T-111 TCIP type tests are shown in Figures 31 and 32. Both the increase in the minimum cycle temperature and the 1 hour hold at the peak temperature and strain decreased the fatigue life over the 2100/400°F (1422/478°K) cycle, with the 1 hour hold providing a greater reduction than the increased minimum temperature (Figure 31). Both changes reduced the stress range for a given fatigue life (Figure 32), with the 1 hour hold having a more severe effect than the temperature increase. The increased minimum temperature caused a small increase in cyclic hardening over the 2100/400°F (1455/478°K) cycle, while the 1 hour hold reduced it (Figure 33).

The above observations of reduced fatigue life with increased minimum temperature and a 1 hour hold at peak temperature are important because both of these effects increased the relative fraction of time in the cycle when the specimen was susceptable to creep damage. This increased life degradation with increased potential for creep affects implies that life reduction may be associated with increased creep damage.

A significant difference was found between the influence of in-phase and out-of-phase thermal cycling on the fatigue life of the T-111 alloy (Figures 34 and 35). The strain range-life relation for the out-of-phase T-111 tests (Figure 34) was very peculiar. The TCOP curve fell above and essentially parallel to the isothermal curve at the lower strain ranges, but crossed the isothermal curve and was significantly below it at the higher strain ranges. The out-of-phase cycle caused a significant increase of stress range over both the isothermal and TCIP cycles (Figure 35), with the S-N curve having a lower slope and being more nearly linear (within the range of experimental scatter) than for either of the other types of test. This increase in stress range was accompanied by a significant increase in the amount of cyclic strain hardening, as compared with the TCIP test which showed very little increase in cyclic strain hardening over the isothermal test (Figure 36).

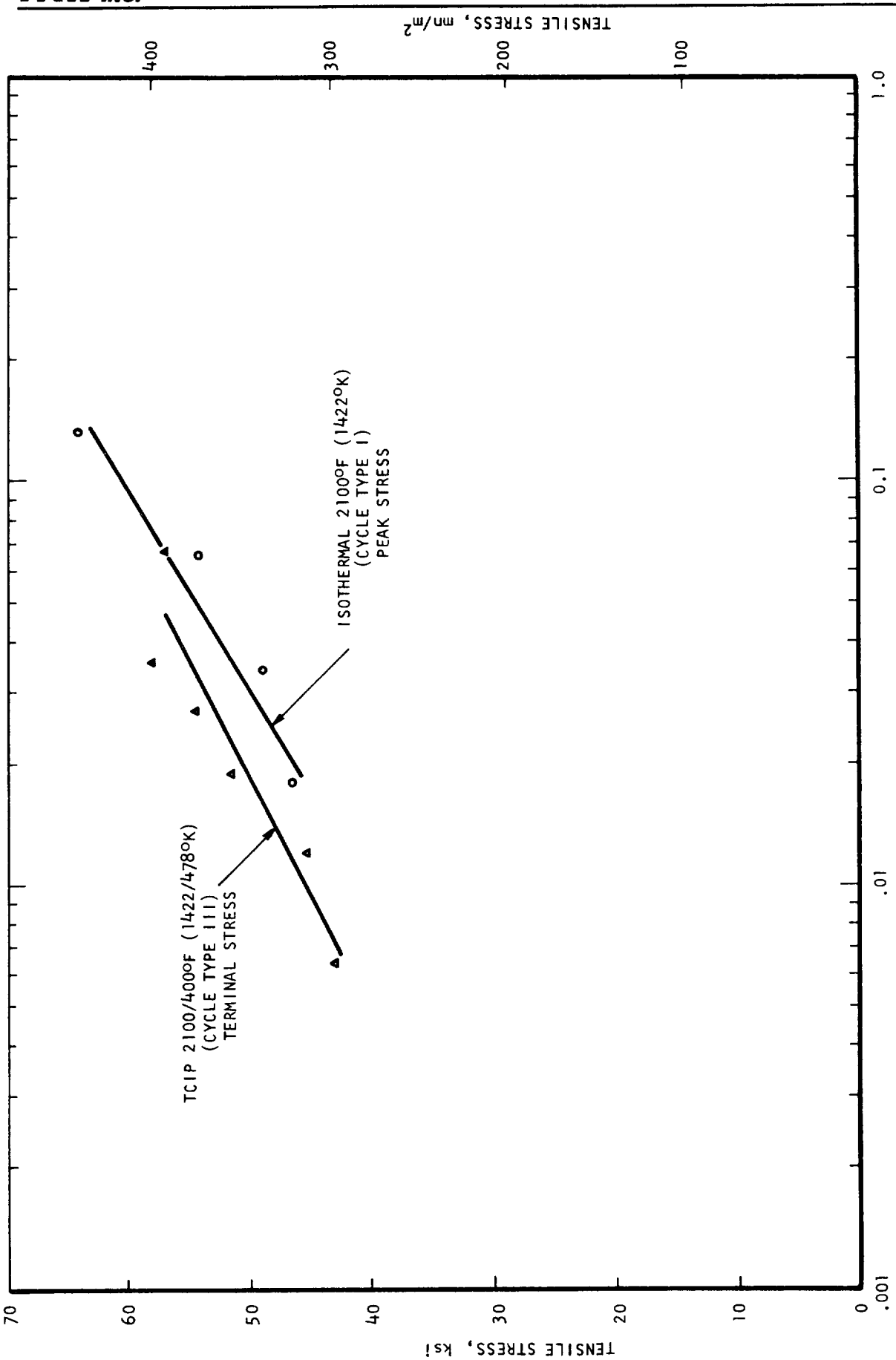

Figure 28. Comparison of tensile stress at 2100°F (1422°K) for isothermal 2100°F (1422°K) and TCIP 2100/400°F (1422/478°K) types of test on T-111 alloy.

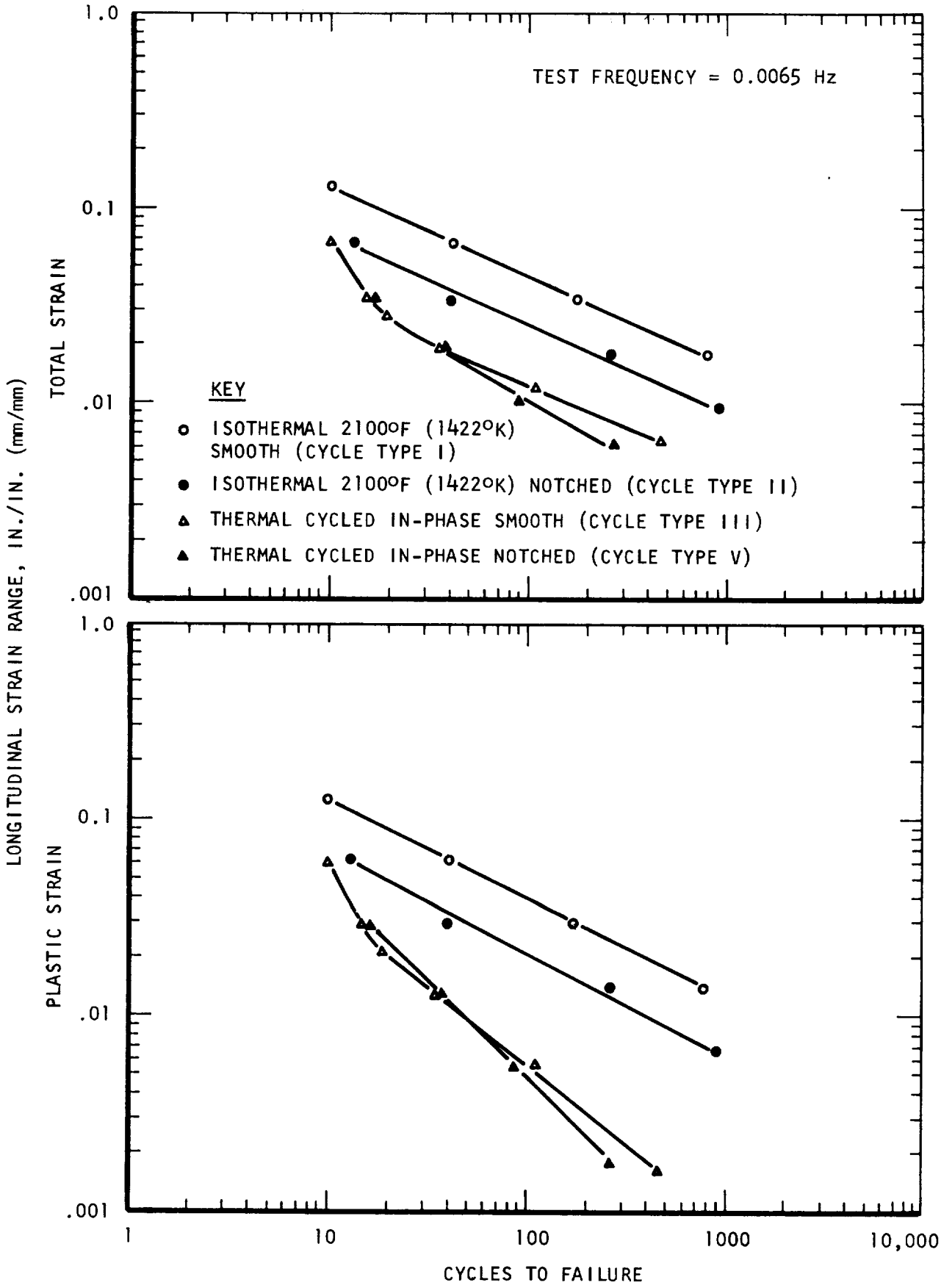

Figure 29. Influence of strain range on the fatigue life of T-111 alloy tested with the indicated types of thermal-mechanical cycling.

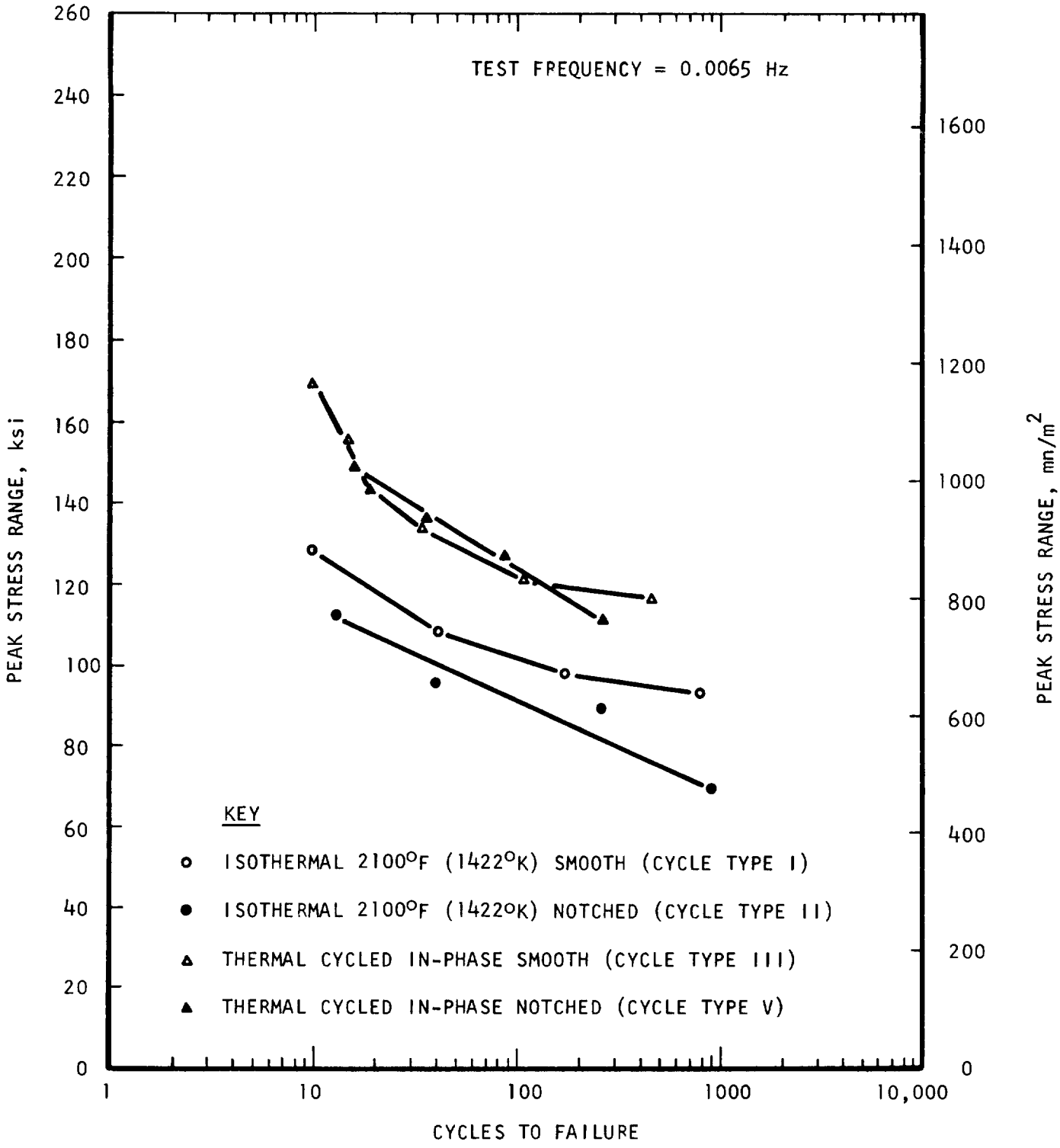

Figure 30. S/N curves for T-111 alloy tested with the indicated types of thermal-mechanical cycling.

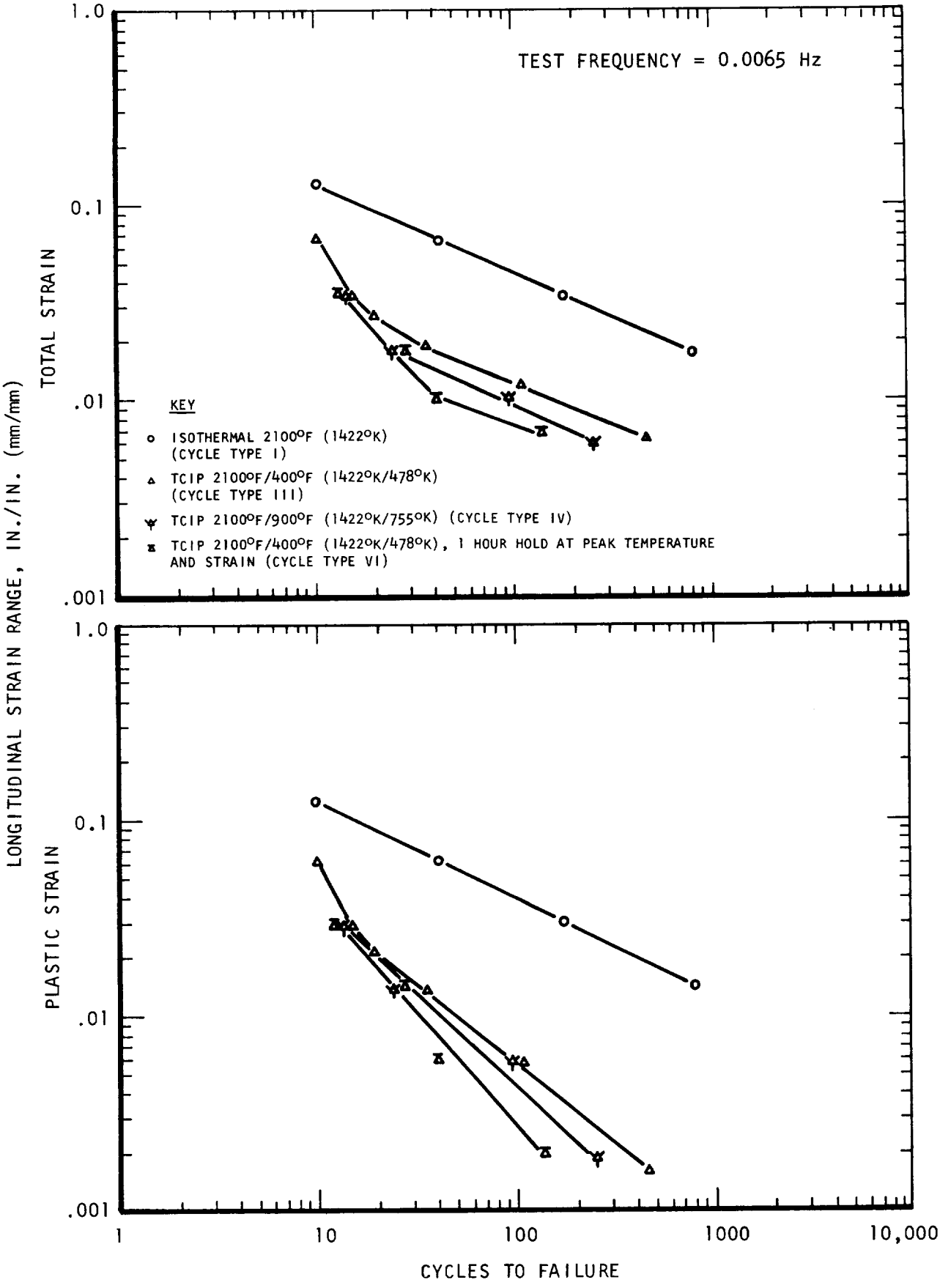

Figure 31. Influence of strain range on the fatigue life of T-111 alloy tested with the indicated types of thermal-mechanical cycling.

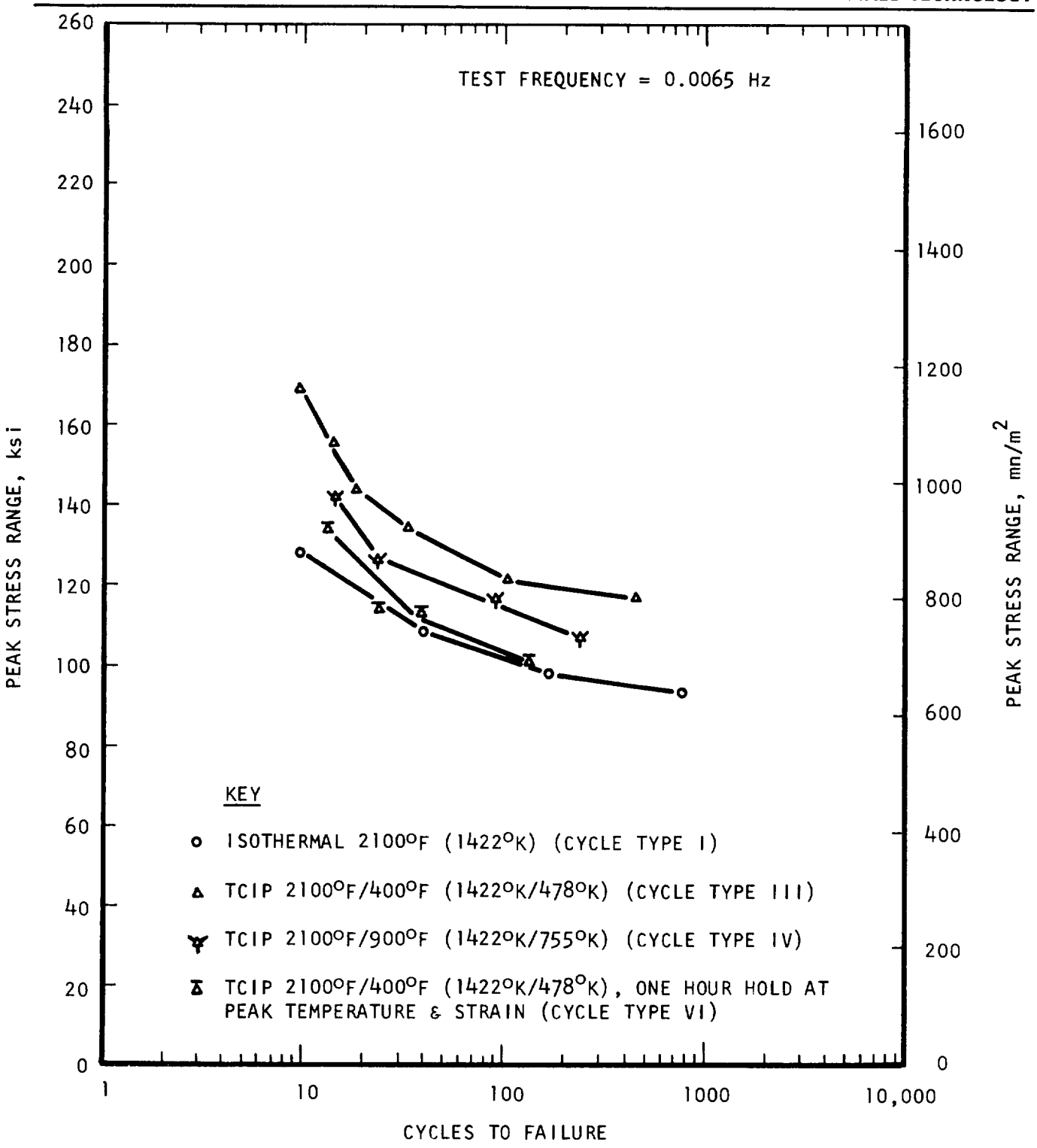

Figure 32. S/N curves for T-111 alloy tested with the indicated types of thermal-mechanical cycling.

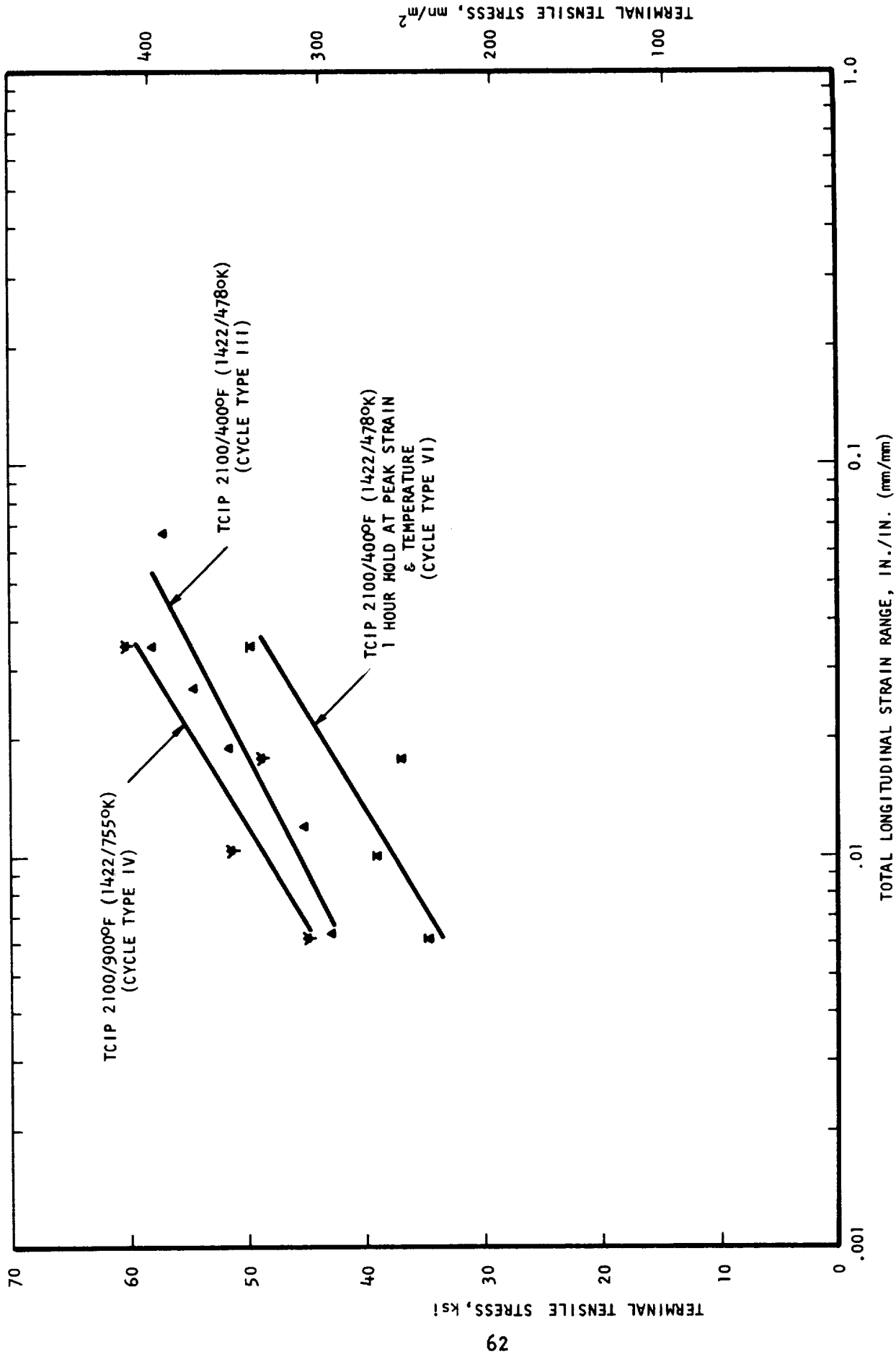

Figure 33. Influence of variations in TCIP test parameters on the 2100°F (1422°K) terminal tensile stress in T-111 alloy.

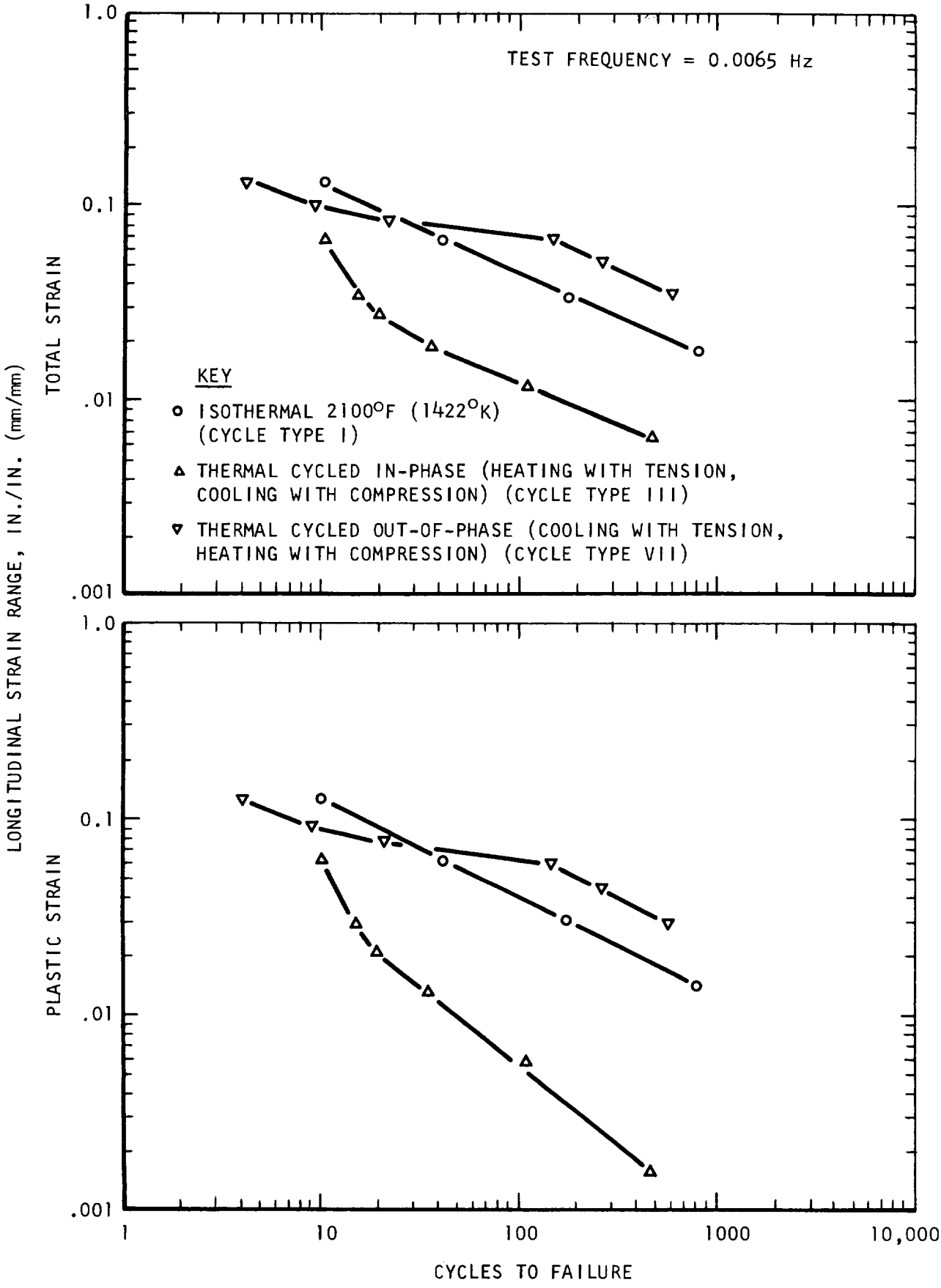

Figure 34. Influence of strain range on the fatigue life of T-111 alloy tested with the indicated types of thermal-mechanical cycling.

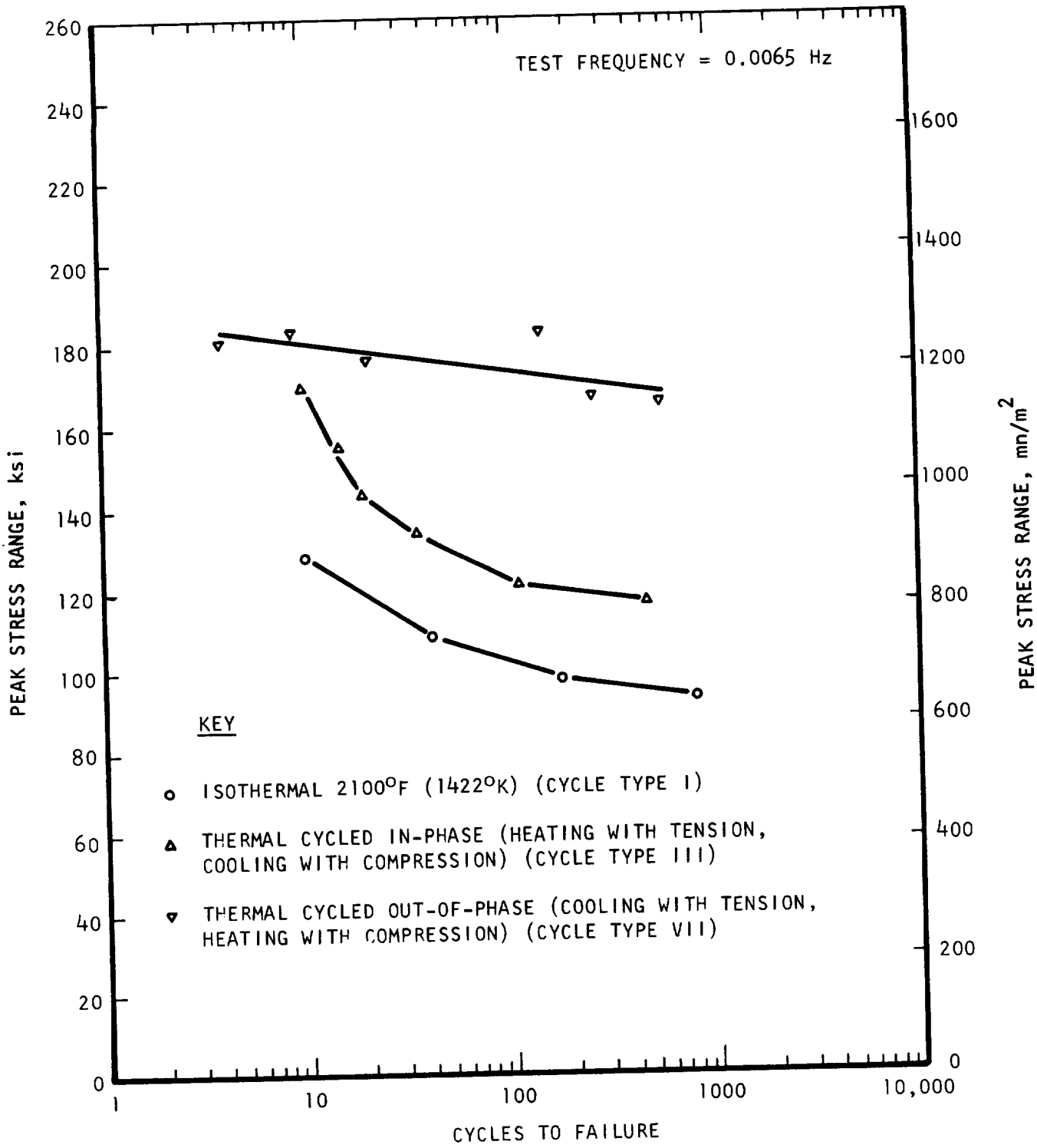

Figure 35. S/N curves for T-111 alloy tested with the indicated types of thermal-mechanical cycling.

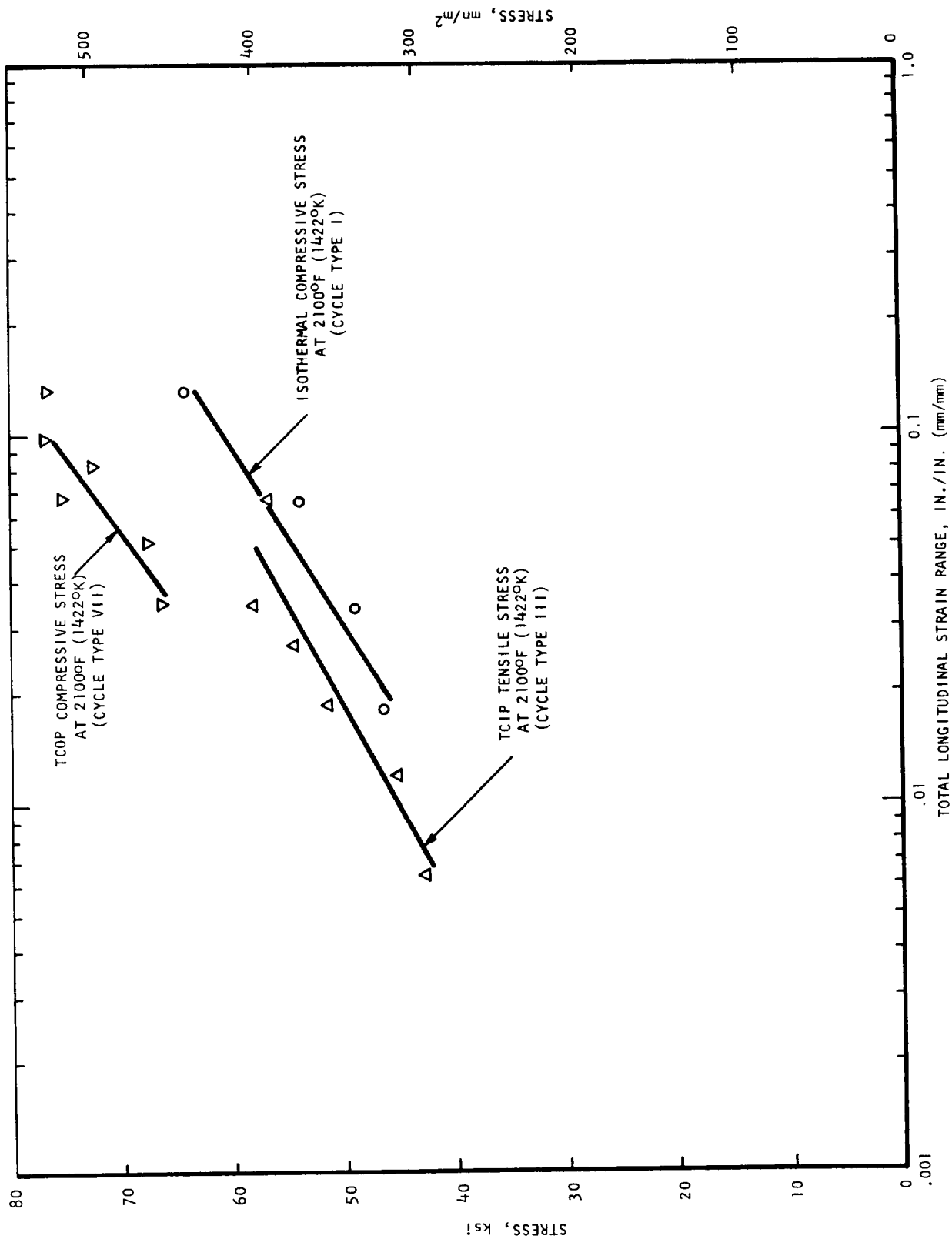

Figure 36. Comparison of cyclic strain hardening behavior for T-111 alloy tested with isothermal, TCIP, and TCOP types of thermal-mechanical cycles.

To summarize the T-111 thermal-mechanical fatigue behavior, synchronized independently controlled thermal cycling had a pronounced influence on the fatigue life of the T-111 alloy. In-phase cycling (heating with tension, cooling with compression) caused severe reductions of the fatigue life, while out-of-phase cycling (cooling with tension, heating with compression) both improved and degraded the fatigue life, depending on the strain range.

4. ASTAR 811C Alloy Behavior

Isothermal fatigue life data for the ASTAR 811C alloy are presented in Figures 37 and 38. The results of isothermal tests at 400°F (478°K), 1600°F (1144°K), and 2100°F (1422°K) were clustered in a relatively narrow band centered about the direct universal slopes predictions for 2100°F (1422°K) (Figure 37), indicating significantly less effect of creep on fatigue life of ASTAR 811C at the 2100°F (1422°K) test temperature than was observed with the T-111 alloy. The 400°F (478°K) results were parallel to and slightly below the 2100°F (1422°K) data, while the 1600°F (1144°K) line was slightly below both the 400 and 2100°F (478 and 1422°K) curves at the higher strain ranges, but cut through at a slightly lower slope and was above both curves at the lower strain ranges. The 1600°F (1144°K) results were particularly important because they demonstrated that no significant fatigue life reduction was associated with the dynamic strain aging phenomenon. The high frequency tests at 2100°F (1422°K) were difficult to rationalize. A definite frequency effect existed at 2100°F (1422°K), but the effect was not consistent over the range of strain amplitudes studied. The high frequency curve was concave downward, with the fatigue life at the three largest strain amplitudes being above the lower frequency life at 2100°F (1422°K). While a direct comparison was not possible at the lowest strain amplitude because no low frequency tests were conducted at this strain range, the high frequency data appeared to be below the extrapolated low frequency curve. This result was sufficiently puzzling that duplicate high frequency tests were conducted to confirm it, as shown in Figure 37. No satisfactory explanation was developed during the course of this study for the apparent crossover of the high and low frequency curves.

The isothermal stress response of the ASTAR 811C alloy (Figure 38) increased with decreasing test temperature, with the stress amplitude appearing to show a saturation effect in the 250-260 ksi (1723-1792 MN/m^2) range at 400°F (478°K). The 1600°F (1144°K) S-N curve exhibited a concave upward shape, while the rest of the S-N curves (with the exception of the 400°F behavior mentioned above) were essentially linear. The 2100°F (1422°K) high frequency stress amplitudes were much higher than the corresponding low frequency values at the shorter cyclic lives, but tended to merge at the longer lives.

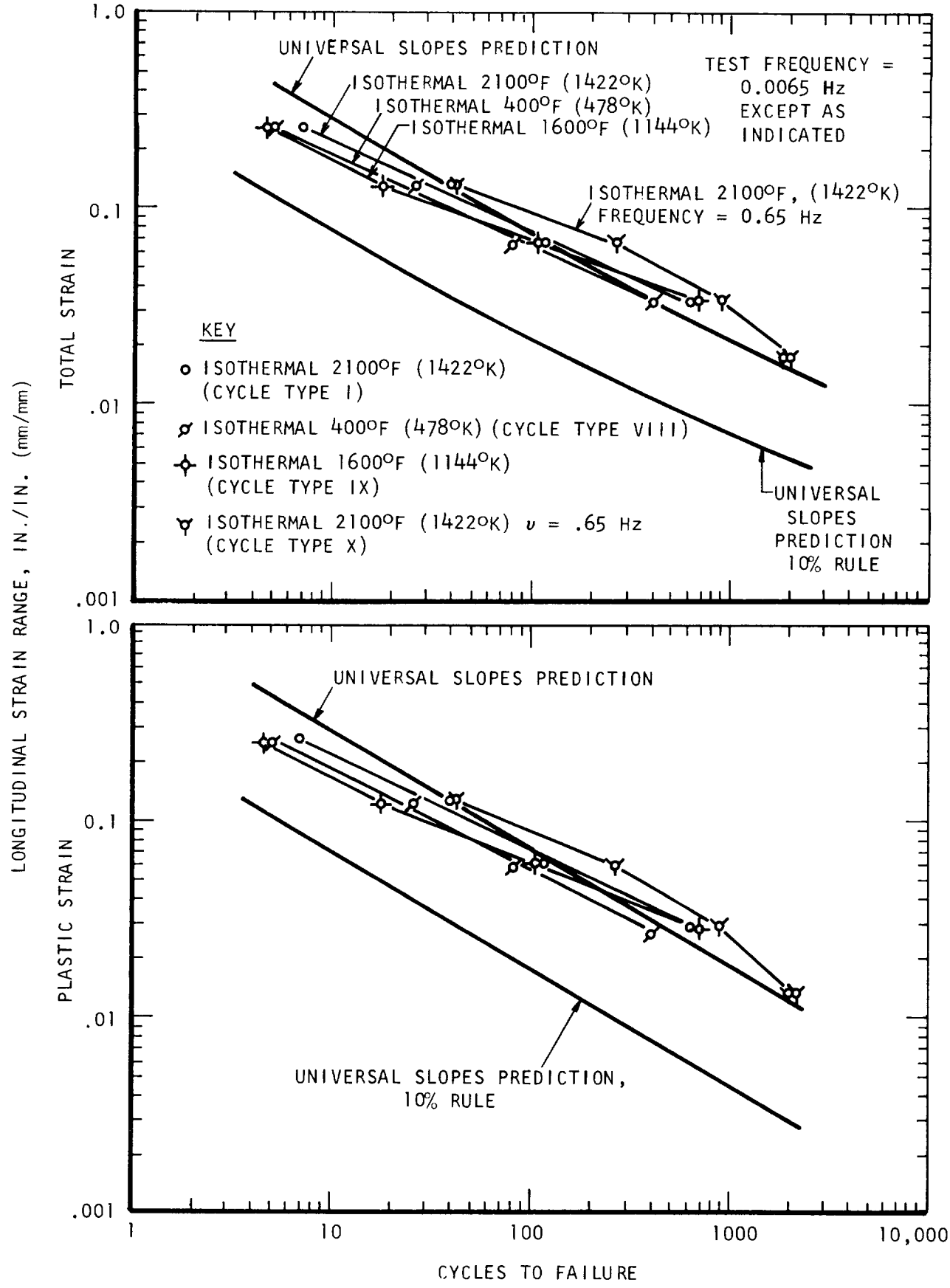

Figure 37. Influence of strain range on the fatigue life of ASTAR 811C alloy tested isothermally at the indicated temperatures.

3406 c

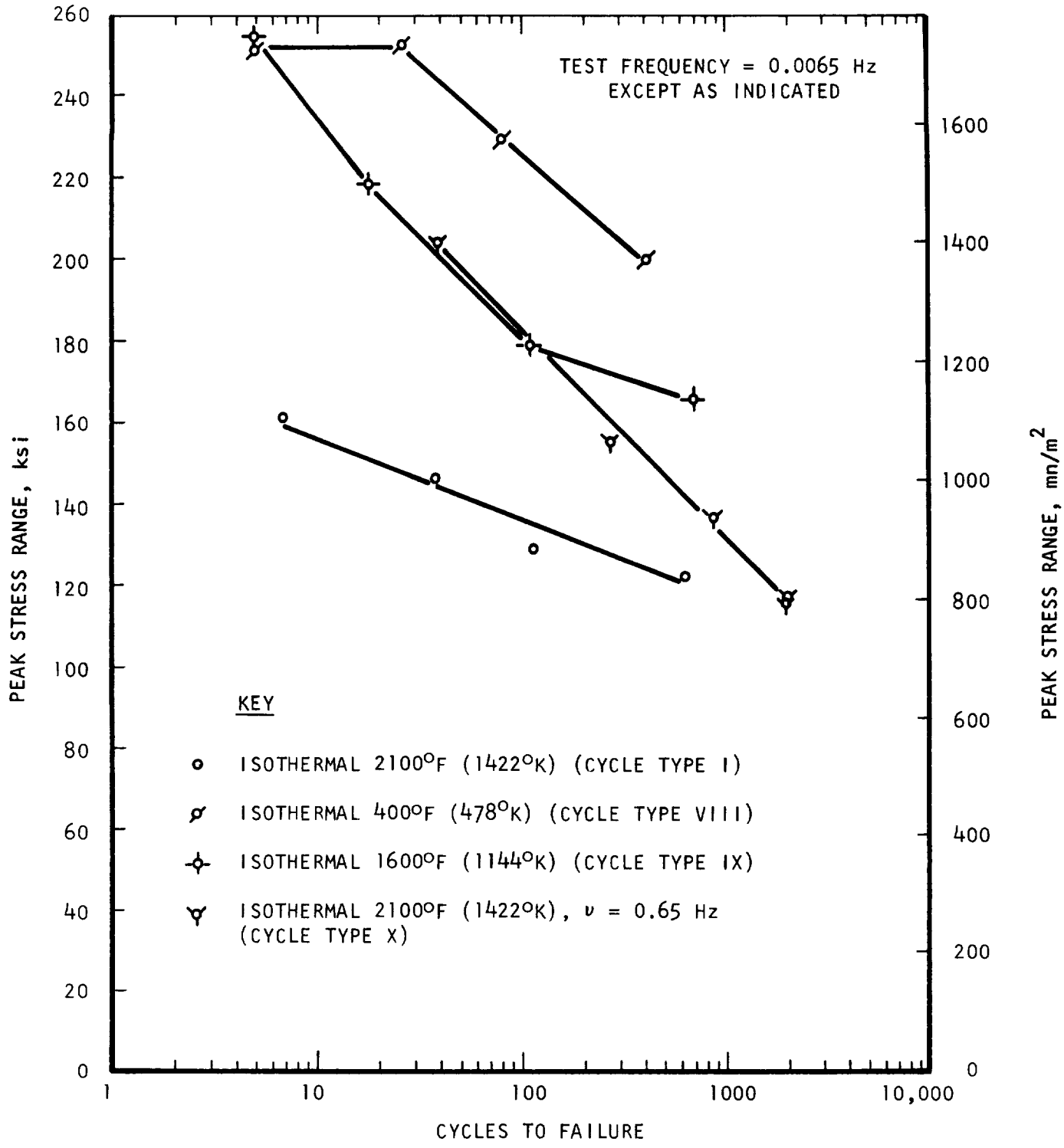

Figure 38. S/N curves for ASTAR 811C alloy tested isothermally at the indicated temperatures.

The influence of in-phase thermal cycling on the fatigue life of the ASTAR 811C alloy is shown in Figures 39 and 40. As with the T-111 alloy, the in-phase thermal cycling had a significant detrimental influence on the life of ASTAR 811C (Figure 39), with the life reduction being larger for the square wave (dual isothermal) type of cycle than for the TCIP type cycle. Reasons for this increased effect of the square wave cycling will be discussed in the subsequent section on partitioning of strain ranges. It is significant to note that the universal slopes 10% rule provided conservative life predictions with respect to the TCIP type cycling for ASTAR 811C alloy and for all but the lowest strain ranges for the TCIPS type cycles as well. The total strain range plot appeared to provide a slightly better representation of the thermal cycled life data than the plastic strain range plot, with some downward deviation from linearity being noted on the plastic strain range versus cycles to failure representation.

The stress ranges for the ASTAR 811C alloy with in-phase cycling were bracketed between the 400°F (478°K) and 2100°F (1422°K) isothermal stress ranges (Figure 40), with the TCIP results being higher than the square wave results. This was caused by the fact that the TCIP tensile stress peak occurred at a lower temperature (1600°F (1144°K)) than the TCIPS tensile stress peak, and in fact, the square wave cycle actually produced a slightly greater amount of cyclic strain hardening than the TCIP type cycle as shown in Figure 41.

The data presented in Figures 42 and 43 showed that the ASTAR 811C alloy exhibited very little notch sensitivity in both the isothermal and TCIP cycles. As with the T-111 alloy, the fact that the TCIP smooth data were below the isothermal notched results provided definite evidence that the thermal cycled life reduction was not simply a premature crack initiation effect. Stress response for the notched tests was somewhat lower than the smooth response for the TCIP cycle, but crossed the smooth curve and was much steeper in slope for the isothermal cycle (Figure 43).

Variation of the ASTAR 811C fatigue life with changes in the TCIP test parameters followed the same pattern as found in the T-111 alloy, with the increased minimum temperature and 1 hour hold both providing slight reductions of fatigue life with respect to the 2100/400°F (1422/478°K) in-phase thermal cycle (Figure 44). Both cycle changes also lowered the TCIP S-N curve (Figure 45), with the 1 hour hold providing the greater reduction. Also, as with the T-111 alloy, the increased minimum temperature provided a slight increase in cyclic strain hardening, while the 1 hour hold reduced it (Figure 46).

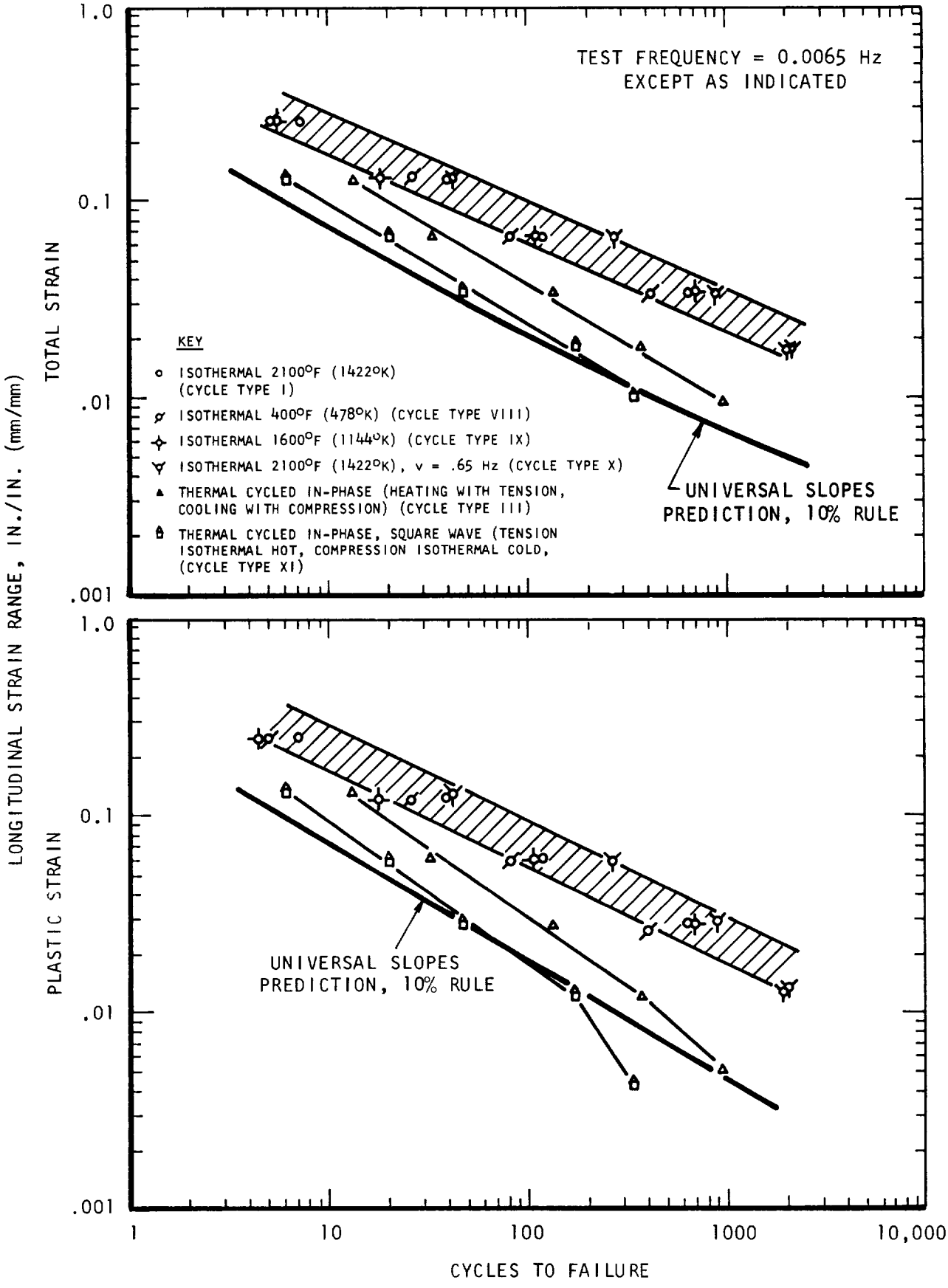

Figure 39. Influence of strain range on the fatigue life of ASTAR 811C alloy tested with the indicated types of thermal-mechanical cycling.

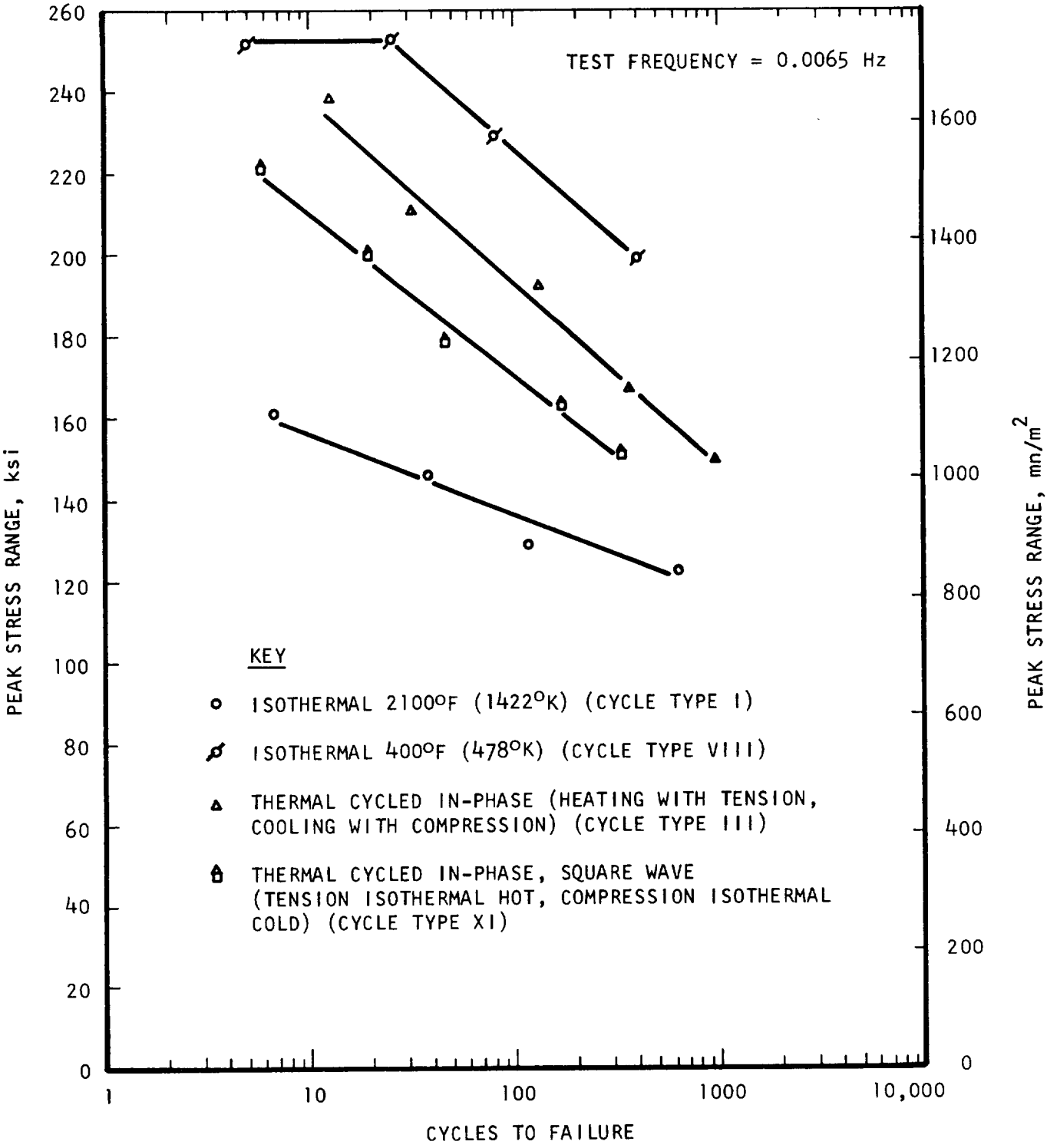

Figure 40. S/N curves for ASTAR 811C alloy tested with the indicated types of thermal-mechanical cycling.

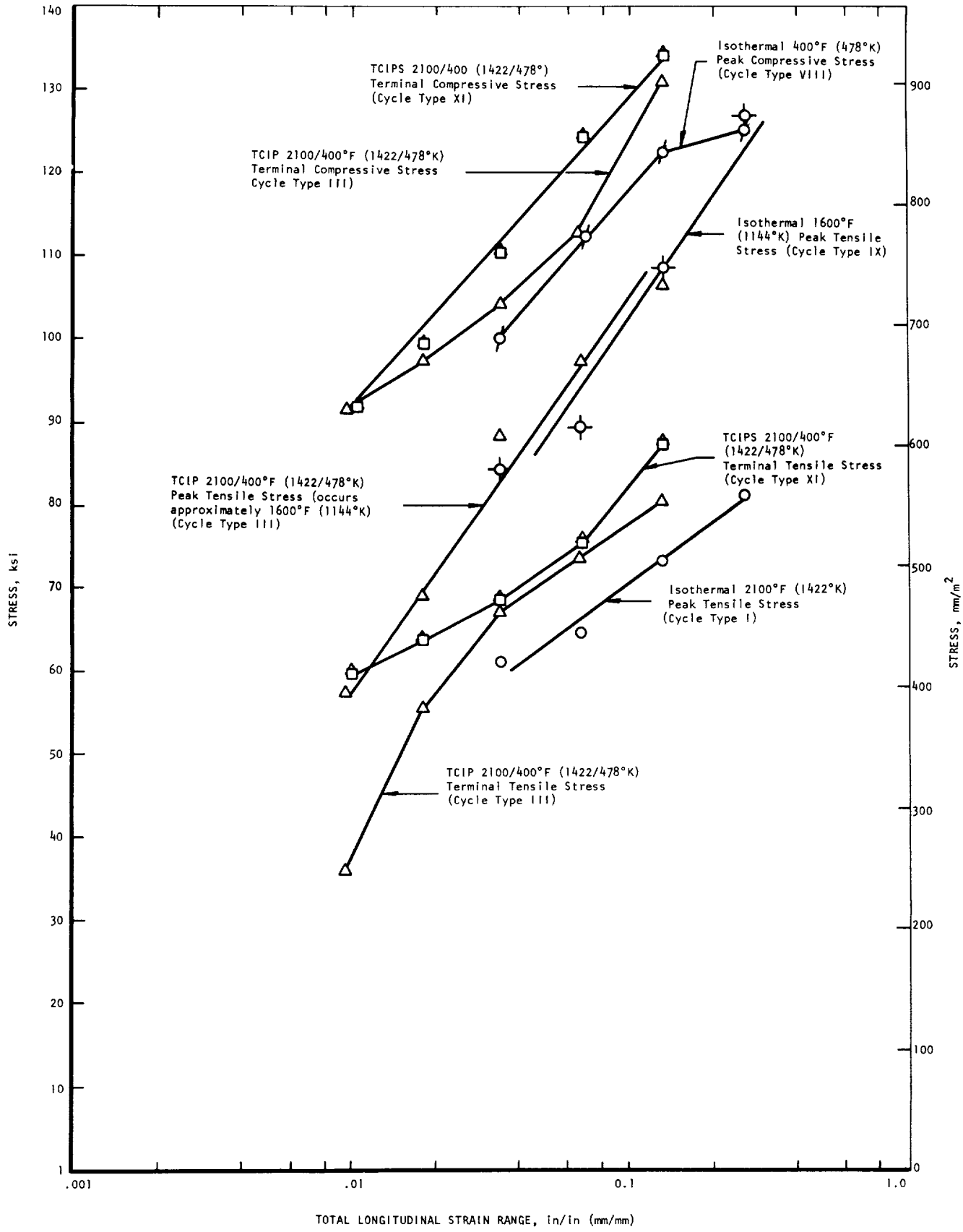

Figure 41. Comparison of cyclic strain hardening behaviors for ASTAR 811C alloy tested with isothermal, TCIP, and TCIPS types of temperature and strain cycles.

3407 c

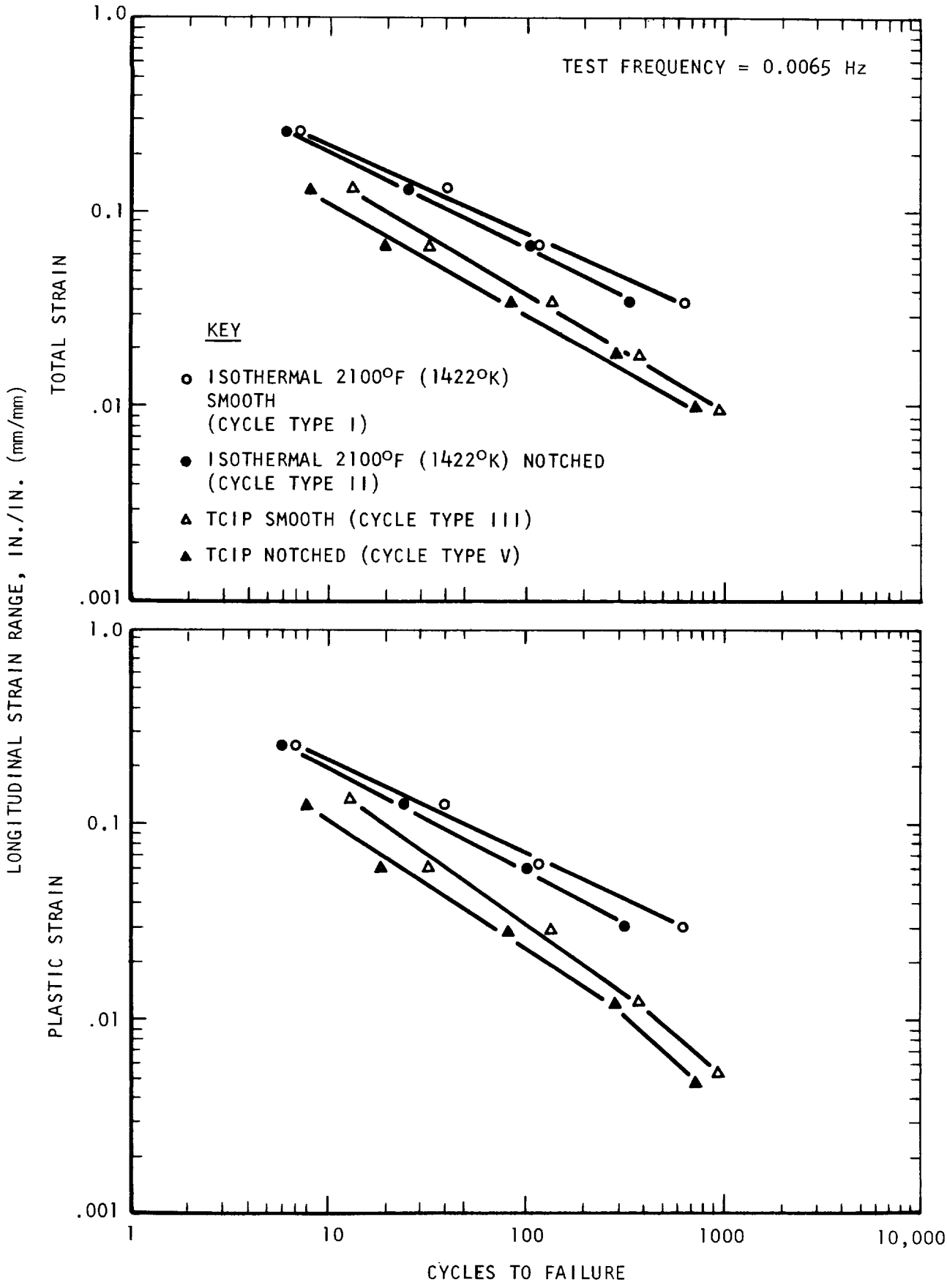

Figure 42. Influence of strain range on the fatigue life of ASTAR 811C alloy tested with the indicated types of thermal-mechanical cycling.

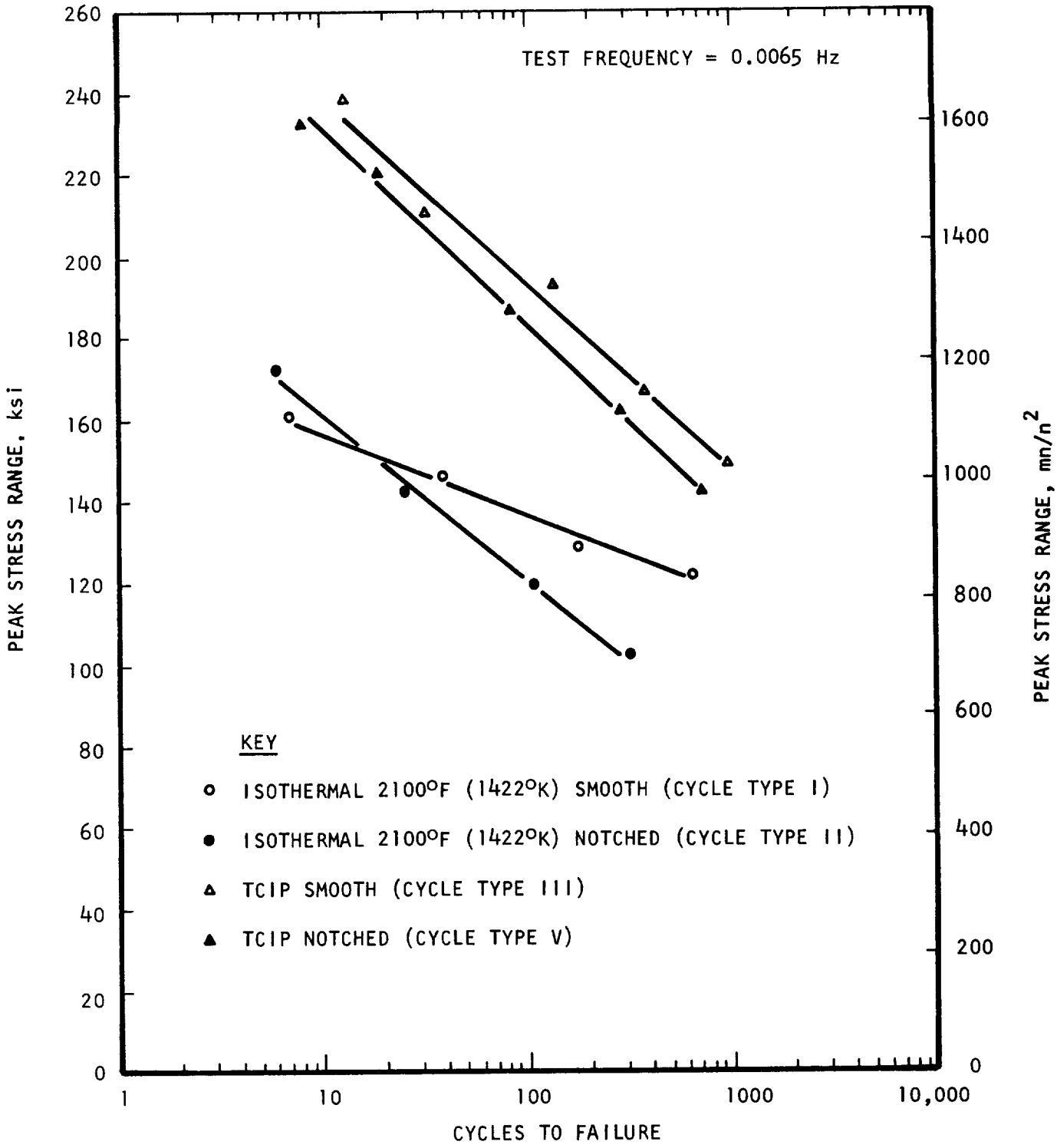

Figure 43. S/N curves for ASTAR 811C alloy tested with the indicated types of thermal-mechanical cycling.

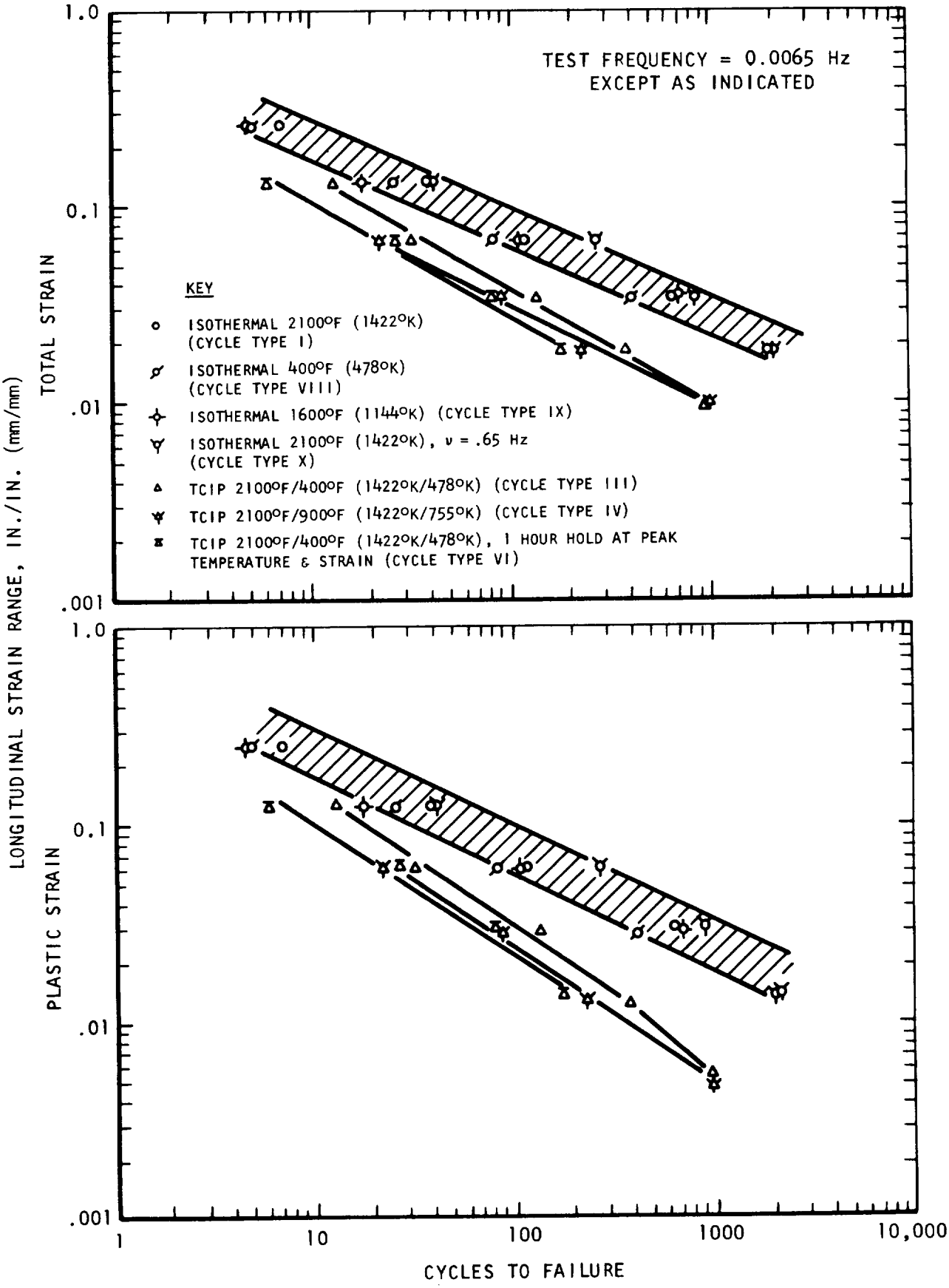

Figure 44. Influence of strain range on the fatigue life of ASTAR 811C alloy tested with the indicated types of thermal-mechanical cycling.

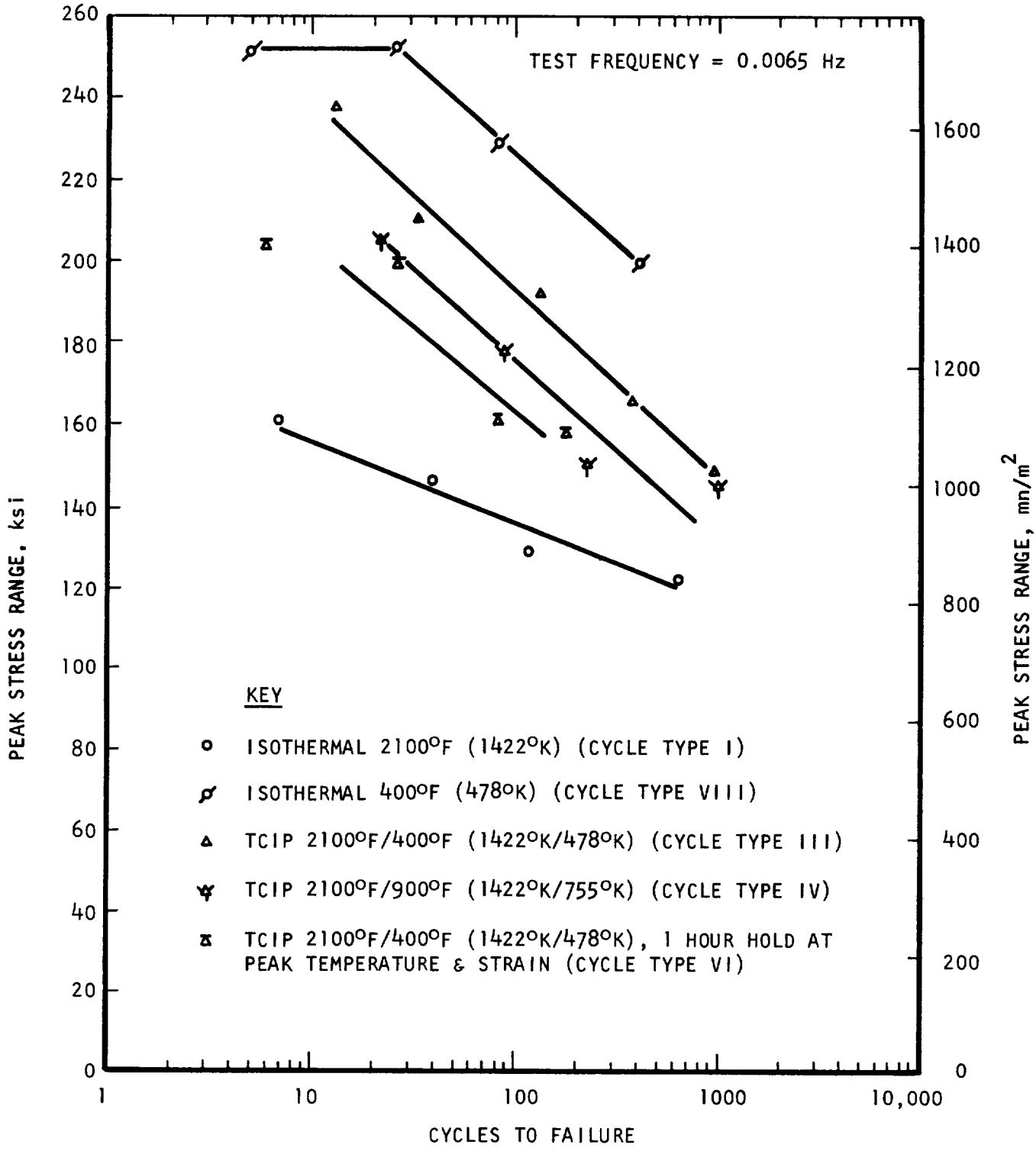

Figure 45. S/N curves for ASTAR 811C alloy tested with the indicated types of thermal-mechanical cycling.

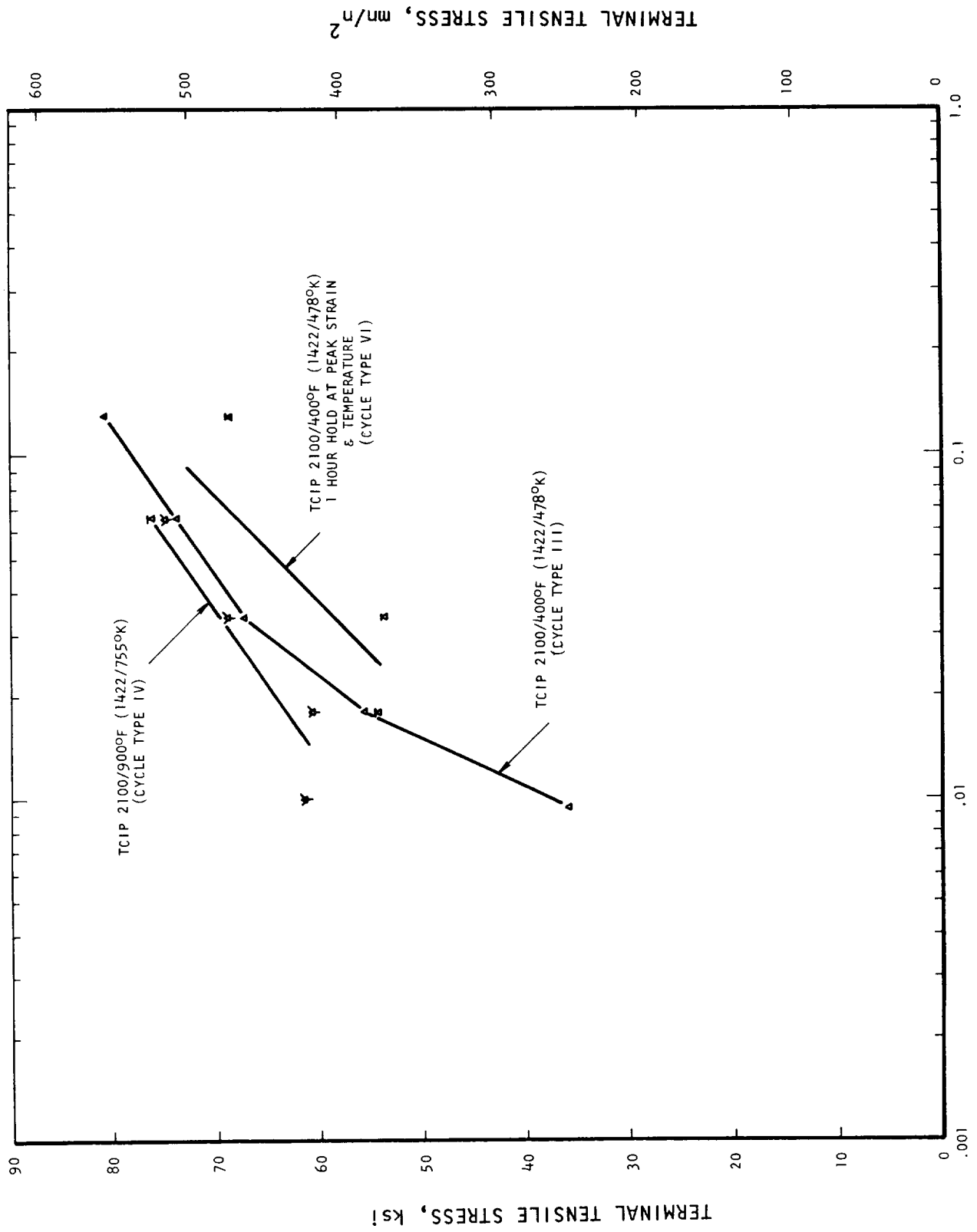

Figure 46. Influence of variations in TCIP test parameters on the 2100°F (1422°K) terminal tensile stress in ASTAR 811C alloy.

Out-of-phase thermal cycling reduced the fatigue life of the ASTAR 811C alloy for both the TCOP and TCOPS types of cycles. The out-of-phase effect was significantly smaller than the in-phase effect in both cases (Figure 47). As with the in-phase type of cycle, the square wave reduction was larger than the reduction with TCIP cycling. The out-of-phase results for the ASTAR 811C alloy were more consistent than those from the T-111 alloy in that the life reduction for the ASTAR 811C material occurred over the entire range of strain amplitudes studied, rather than just at the higher strain ranges. S-N curves for the TCOP and TCOPS cycles both fell above the corresponding TCIP and TCIPS curves (Figure 48). The TCOP S-N curve was essentially parallel to the two in-phase curves, while the TCOPS curve had a lower slope, being more nearly parallel to the isothermal curve.

The cyclic strain hardening behavior produced by out-of-phase testing of the ASTAR 811C alloy was significantly different than that observed for the in-phase tests. For in-phase testing of the ASTAR alloy, both the TCIP and TCIPS hardening curves were above the corresponding isothermal curves, with the square wave cycle causing more hardening than the TCIP cycle (Figure 41). TCOP cycling caused about the same amount of additional hardening over the isothermal cycling as did the TCIP cycling; however, the TCOPS cycle caused less cyclic hardening than the isothermal cycling (Figure 49) which is in sharp contrast to the in-phase results, where the TCIPS cycles caused more hardening than the TCIP cycle. This behavior also contrasted sharply with the T-111 behavior, where out-of-phase testing caused significantly more cyclic hardening than in-phase testing (Figure 36).

5. Summary and Comparison of Test Materials

To summarize the thermal fatigue behavior of the two tantalum alloys, both materials showed significant effects of thermal cycling on fatigue life, with in-phase cycling (tension hot, compression cold) causing large reductions in fatigue life, while out-of-phase cycling (tension cold, compression hot) both increased and decreased the fatigue life, depending on the material and strain range. Notched tests showed that premature crack initiation was not the cause of the thermal effects in either material, while variations in the cycle parameters showed that changes in the thermal cycle which increased the potential for creep effects also increased the magnitude of the thermal cycled life reductions.

The most significant difference between the two alloys was the higher level of fatigue resistance possessed by the ASTAR 811C alloy, both with respect to the isothermal fatigue strength and with respect to the in-phase thermal cycled life degredation effect (Figure 50). The improved fatigue resistance of the carbide strengthened ASTAR 811C over the solid solution strengthened T-111 alloy was thought to be associated with the previously noted higher tensile and creep strength of this material. Specific strengthening mechanisms in the ASTAR alloy which improved the fatigue strength will be discussed in the following section on structural analysis.

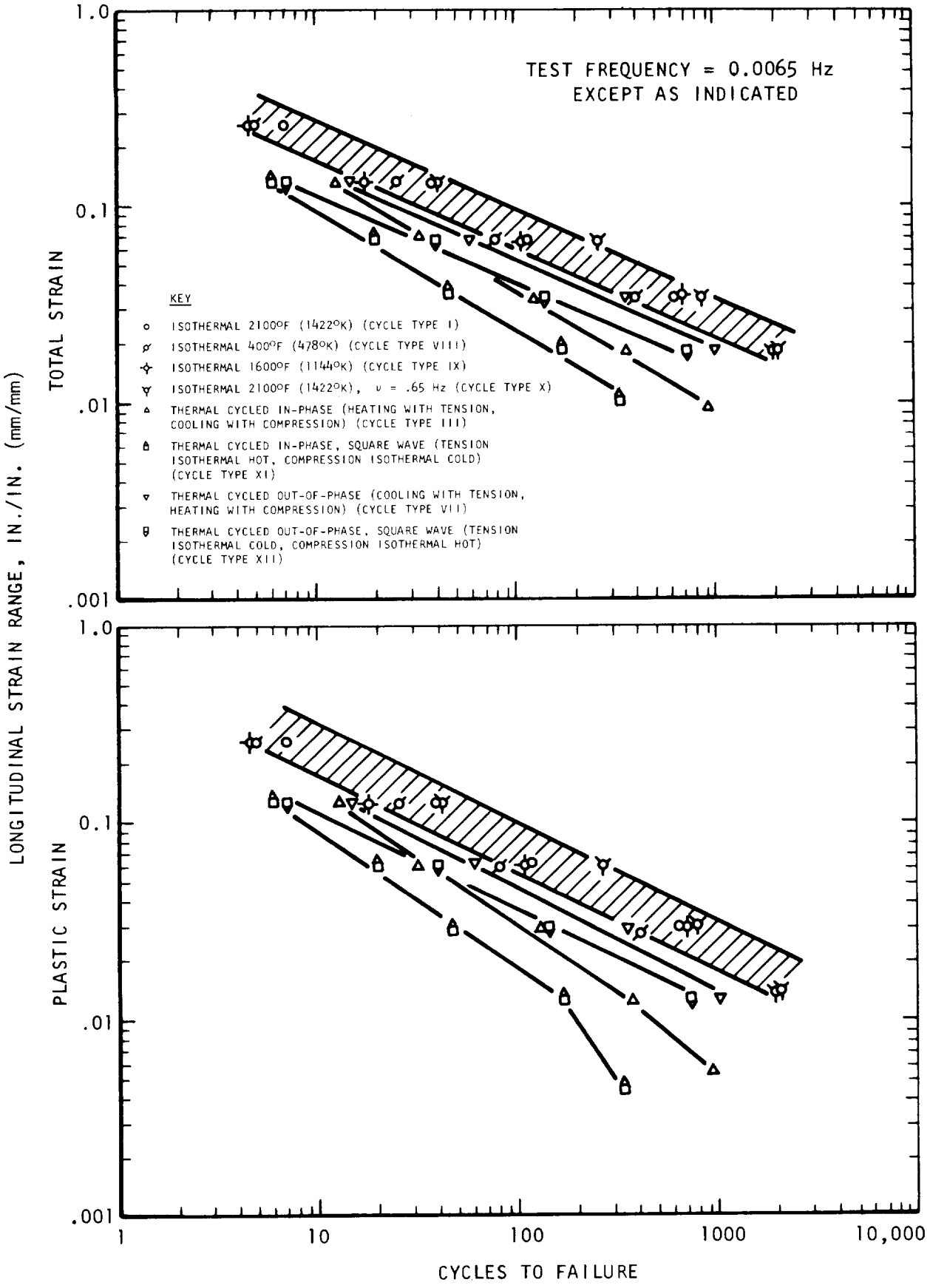

Figure 47. Influence of strain range on the fatigue life of ASTAR 811C alloy tested with the indicated types of thermal-mechanical cycling.

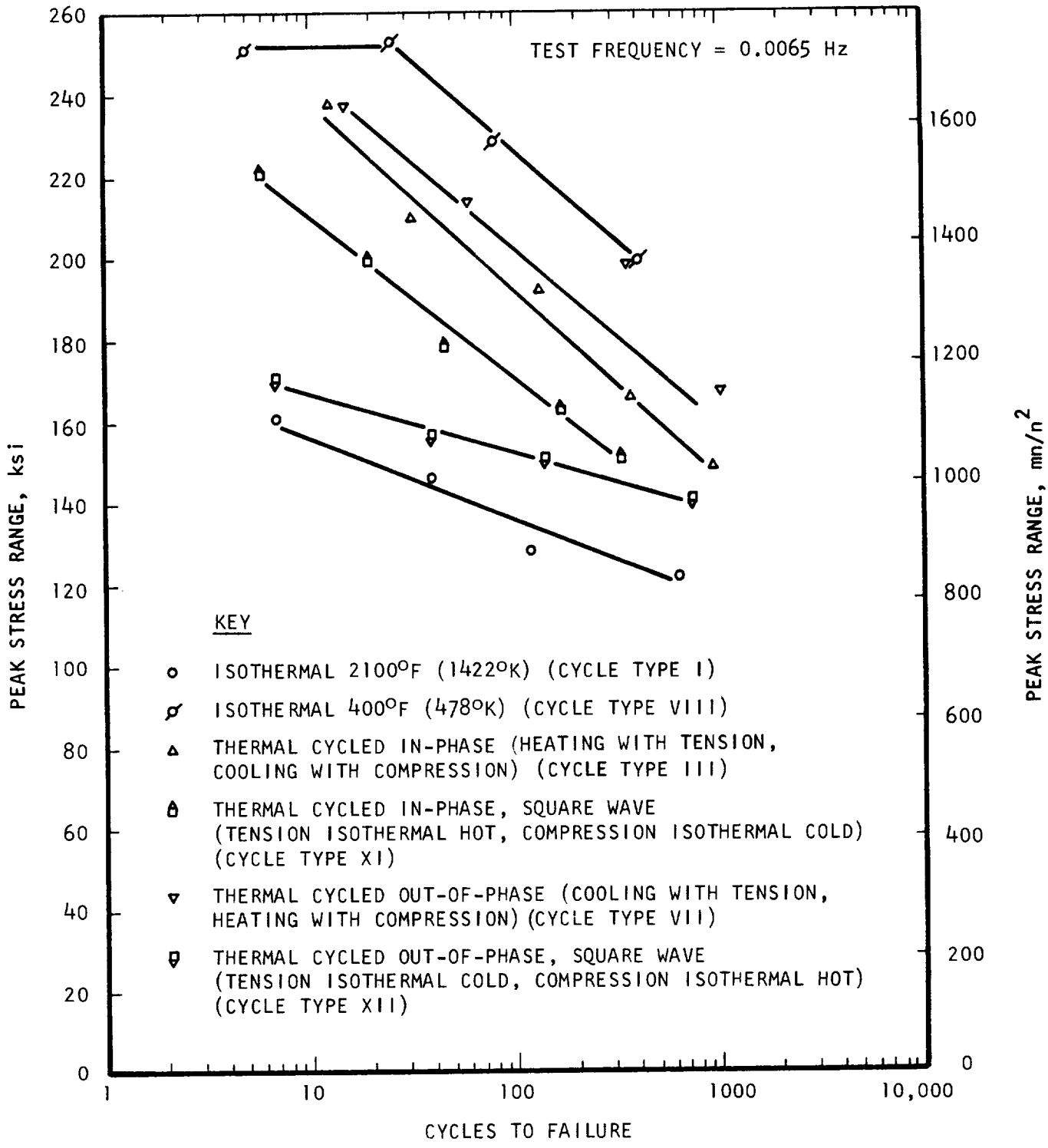

Figure 48. S/N curves for ASTAR 811C alloy tested with the indicated types of thermal-mechanical cycling.

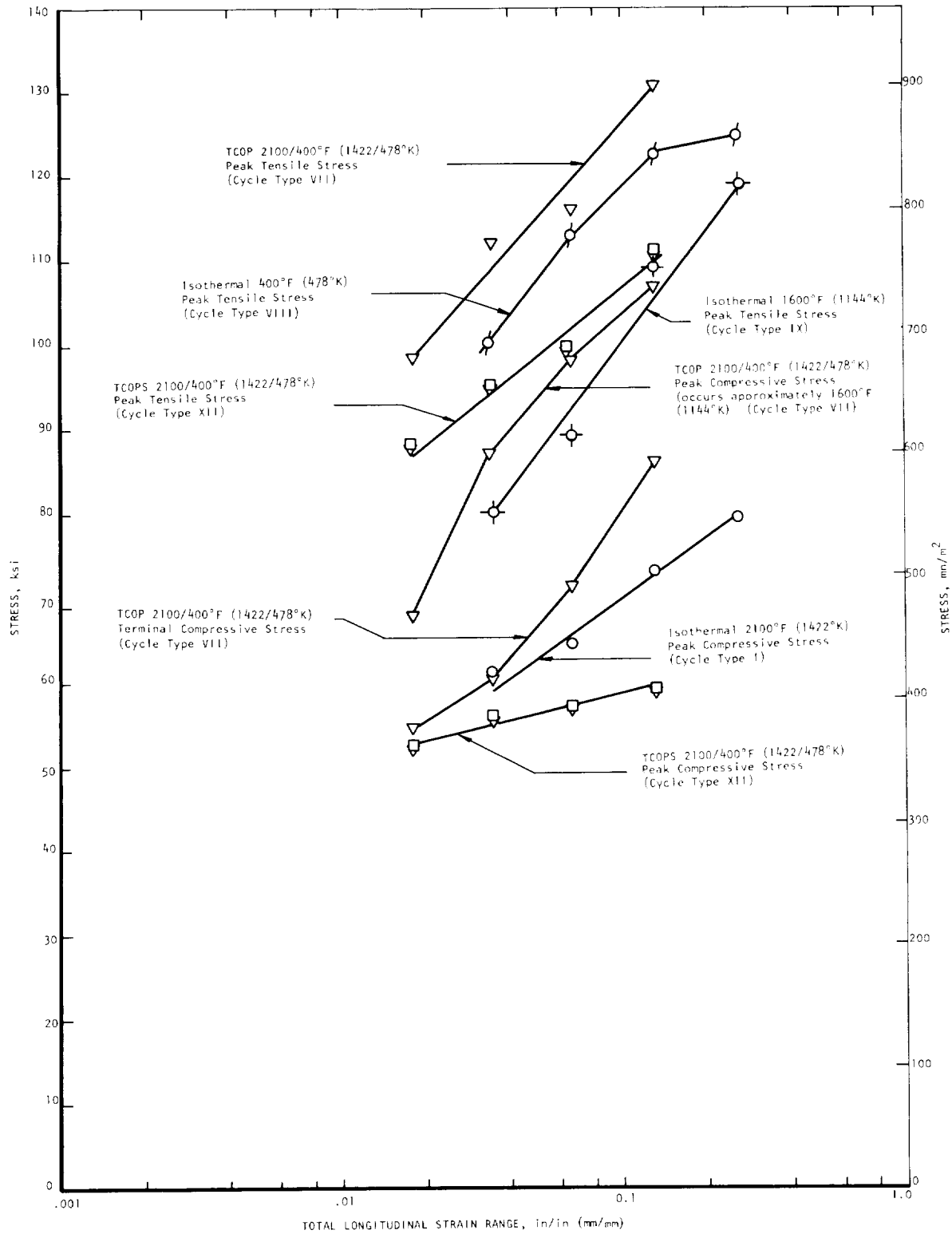

Figure 49. Comparison of cyclic strain hardening behavior for ASTAR 811C alloy tested with isothermal TCOP, and TCOPS types of thermal-mechanical cycles.

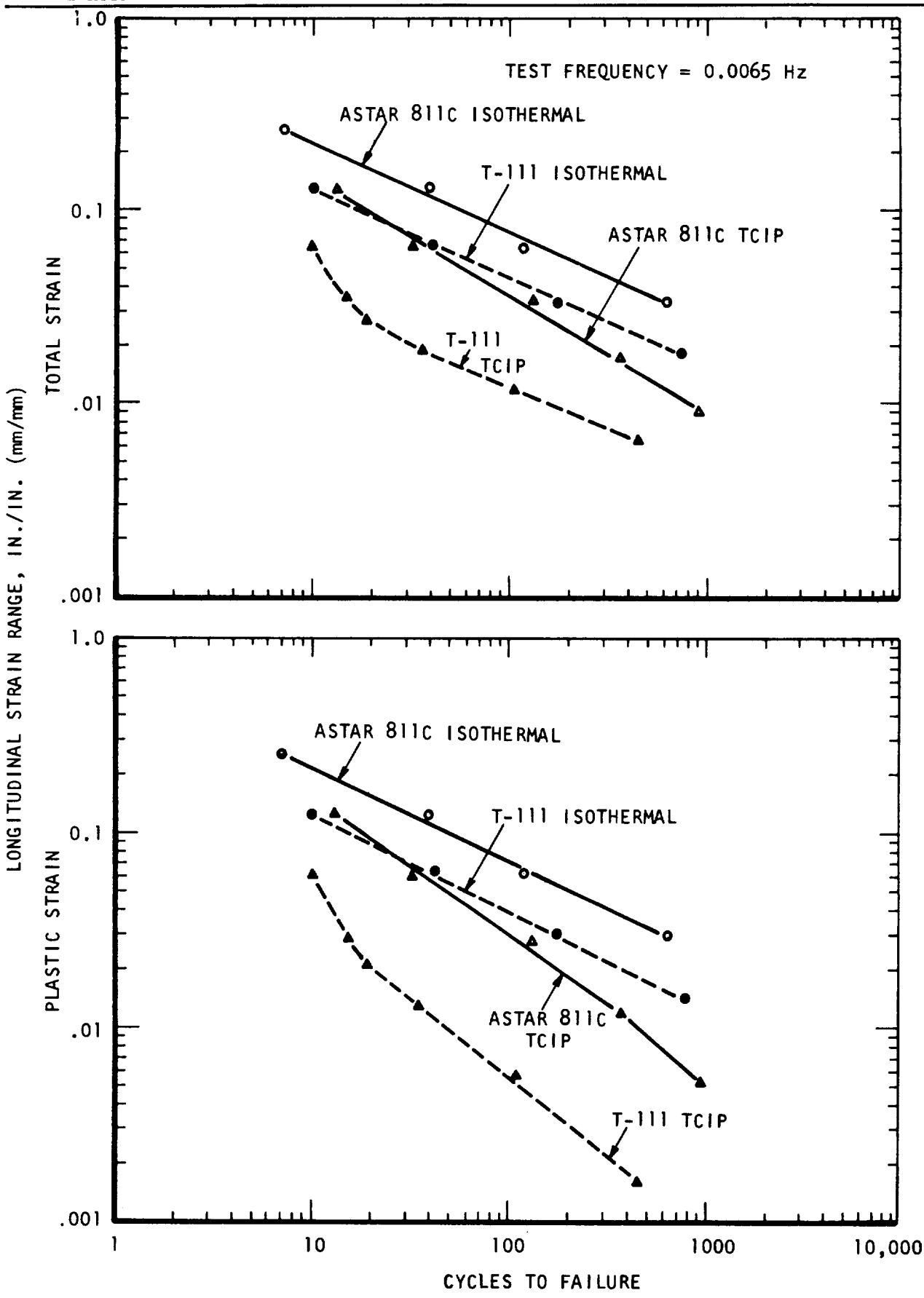

Figure 50. Comparison of isothermal 2100°F (1422°K) and TCIP 2100/400°F (1422/478°K) fatigue behavior of T-111 and ASTAR 811C alloys.

C. Structural Analysis of Tested Specimens

Thermal mechanical fatigue testing caused significant changes in specimen geometry, which in some cases influenced the observed fatigue life. Extensive microstructural damage was also seen in the majority of specimens subjected to fatigue cycling. Both effects depended strongly on the type of thermal-mechanical cycle applied. For a given cycle type the changes were similar in both materials, differing more in the degree than in the nature of the damage. The ultrahigh vacuum exposure also caused minor compositional changes in both alloys, which were not thought to have a significant influence on fatigue behavior.

1. Specimen Geometry Changes

Two basic types of specimen geometry change were observed, as illustrated in Figure 51. The more common type of change was associated with the isothermal and the in-phase cycles, and was characterized by an increase in specimen diameter adjacent to the center of the original hourglass configuration (Figure 51a). This type of geometry change was also observed by Coffin in diametral strain controlled isothermal fatigue testing of 304 stainless steel (5), and was rationalized as a ratchetting effect caused by the development of a mean compressive stress above and below the minimum diameter of an hourglass specimen tested with completely reversed plastic strain (6). Similar arguments can be applied to the isothermal tests reported in this study, and also to the in-phase thermal cycled tests where a mean compressive stress existed because of the asymmetrical hysteresis loop. Specific examples of fractured specimens exhibiting this type of shape change are shown in Figure 52. Because of the fact that this type of change left the location of maximum stress, strain and temperature unchanged during testing, it was assumed to have little effect on the fatigue life.

The second type of geometry change observed (Figure 51b) was associated exclusively with out-of-phase testing and was thought to be responsible for the observed reduction of fatigue life caused by this type of thermal cycling. Similar effects of geometric instability on fatigue life were observed by Carden and Slade in the thermal fatigue testing of Hastelloy X (7). According to Carden, the susceptability to instability effects was a function of strain range, with a threshold level existing below which instability did not occur and above which instability effects were significant (8).

The out-of-phase geometry change was characterized by a reduction of specimen diameter both above and below the original minimum diameter (Figure 51b), so that as testing proceeded the areas of the maximum stress and strain in the specimen shifted away from the location of the original minimum diameter, which was the point of cyclic strain control.

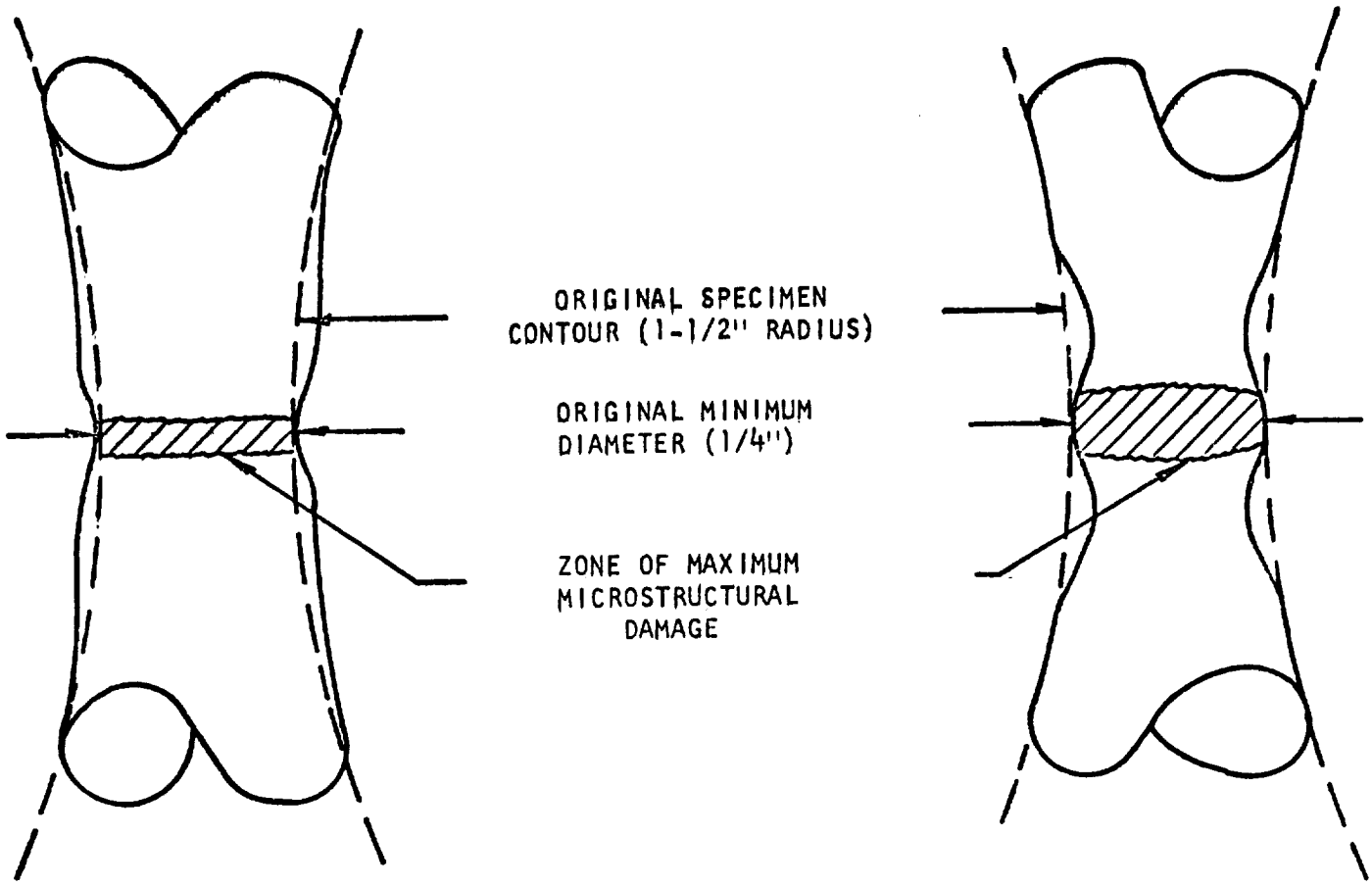

Figure 51. Schematic illustration of specimen geometry changes produced by thermal-mechanical fatigue cycling.

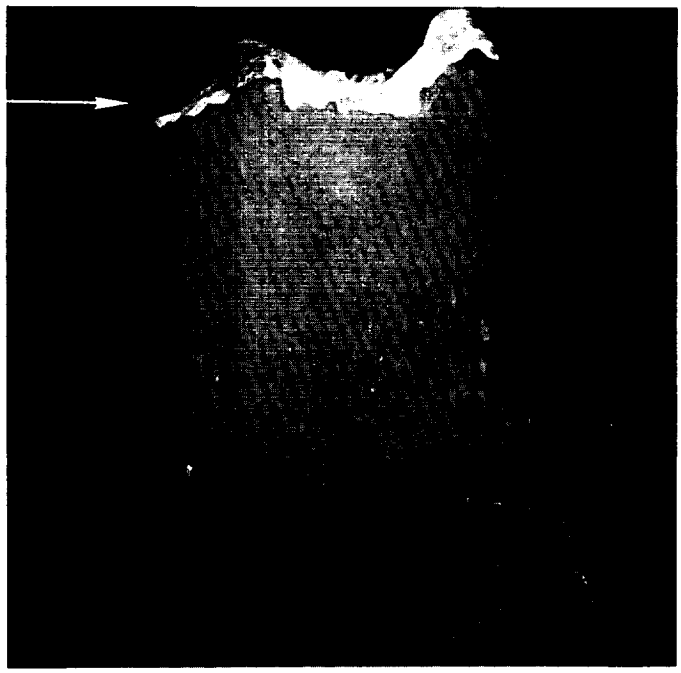

(a) ASTAR 811C-6 Isothermal Cycle
$\Delta\varepsilon$ = 0.344 in/in (mm/mm) Cycles to Failure = 628

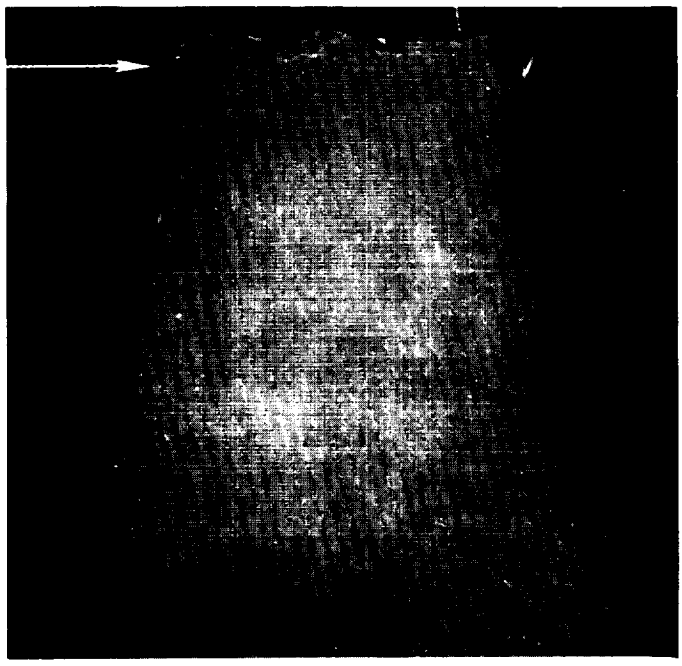

(b) ASTAR 811C-17 TCIP Cycle
$\Delta\varepsilon$ = .0094 Cycles to Failure = 939

Figure 52. Influence of isothermal and in-phase thermal cycling on specimen geometry. Fracture coincides with original minimum diameter. Approximate magnification 7X

This type of instability gave the appearance of necking, with the fatigue fracture occurring at one of the two necks rather than at the location of the original minimum diameter. For the T-111 alloy, the out-of-phase geometric instability was more pronounced at the higher strain ranges (Figure 53a), and in fact the effect appeared to essentially disappear at the smaller strain amplitudes (Figure 53b). This observation indicated that the threshold strain amplitude for instability in the T-111 alloy was within the range of experimentally applied strain, which was assumed to be the cause of the previously observed crossover of the isothermal and TCOP T-111 fatigue curves (Figure 34). It would thus appear that the intrinsic TCOP fatigue resistance of the T-111 alloy may be greater than the isothermal fatigue strength, but that this strength cannot be truly measured at large strain amplitudes because of geometric instabilities associated with the hourglass specimen configuration tested with out-of-phase thermal cycling.

The out-of-phase geometric instability was more pronounced in the ASTAR 811C alloy (Figure 54) and occurred consistently over the entire range of strain amplitudes applied. For a given strain range, the effect was larger in the square wave tests (Figure 55). These observations were consistent with the fact that the out-of-phase ASTAR 811C strain-range fatigue life curves were entirely below the isothermal results, with the TCOPS curve being lower than the TCOP curve (Figure 47). It would thus appear that the intrinsic out-of-phase low cycle fatigue resistance of the ASTAR 811C alloy cannot be measured with the present specimen geometry, as was the case with the T-111 alloy at the higher strain amplitudes.

2. Microstructural Effects

Microstructural damage was separated into three basic categories corresponding to the isothermal, in-phase, and out-of-phase cycle types. More damage was seen in the T-111 alloy, which was consistent with the lower fatigue resistance observed for this material. For a given cycle type, the damage generally increased with increasing test time rather than with increasing strain range. Failure was exclusively intergranular in the T-111 alloy. Intergranular cracking was also the predominent failure mode in ASTAR 811C, although some transgranular cracking was observed in this material. Specific examples of each of these general observations will be pointed out in the following discussions of damage for each basic category of thermal cycling.

a. Isothermal Damage

Isothermal fatigue damage in T-111 at 2100°F (1422°K) was restricted to the grain boundaries, with a tendency for the development of R type voids (Figure 56). The damage was highly localized at high strain amplitudes, but tended to spread to broad bands centered about the grain boundaries at the lower amplitudes (Figure 57). Cracking was intergranular

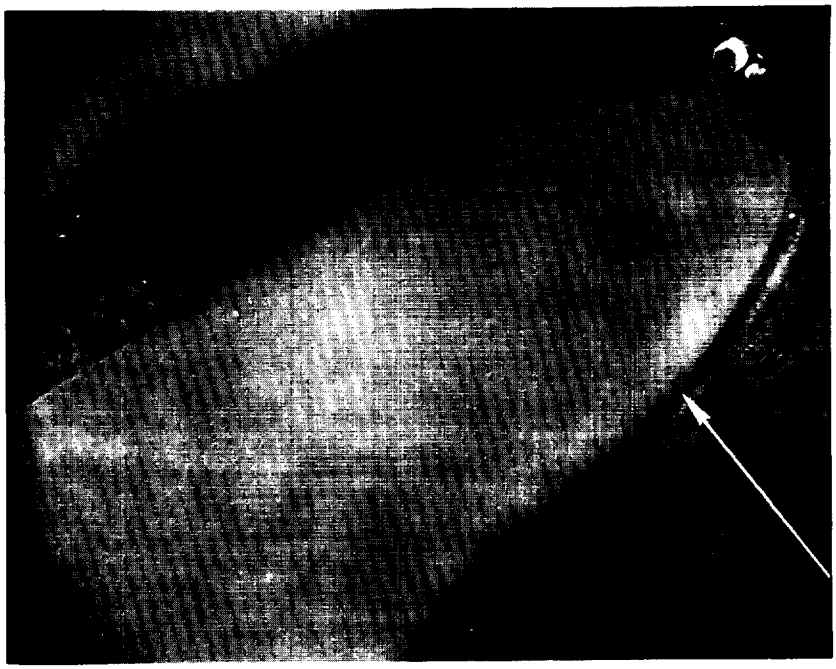

(a) T-111-33
$\Delta\varepsilon$ = .0997
TCOP Cycle
Cycles to Failure = 9

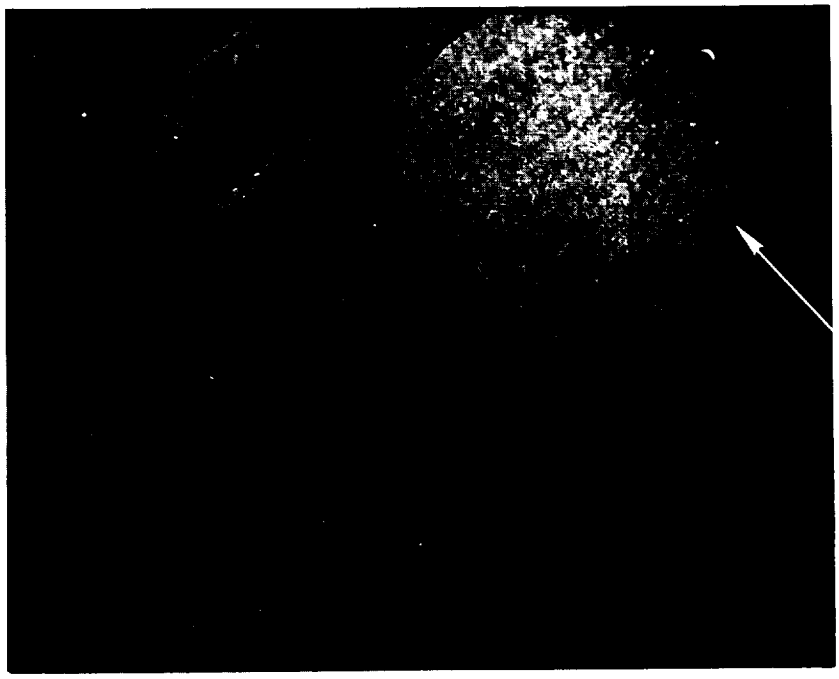

(b) T-111-30
$\Delta\varepsilon$ = .0354
TCOP Cycle
Cycles to failure = 567

Figure 53. Influence of strain range on the specimen geometry change caused by out-of-phase thermal cycling of T-111 alloy. Note that the neck corresponding to the fracture is significantly larger than the secondary neck on the opposite side of the minimum diameter. The majority of this additional necking occurred during the last half-cycle of testing. Approximate magnification 8X

ASTAR 811C-12
$\Delta\varepsilon$ = .0180

TCOP Cycle
Cycles to Failure = 1012

Figure 54. Influence of out-of-phase thermal cycling on specimen geometry of the ASTAR 811C alloy. Approximate magnification 6X

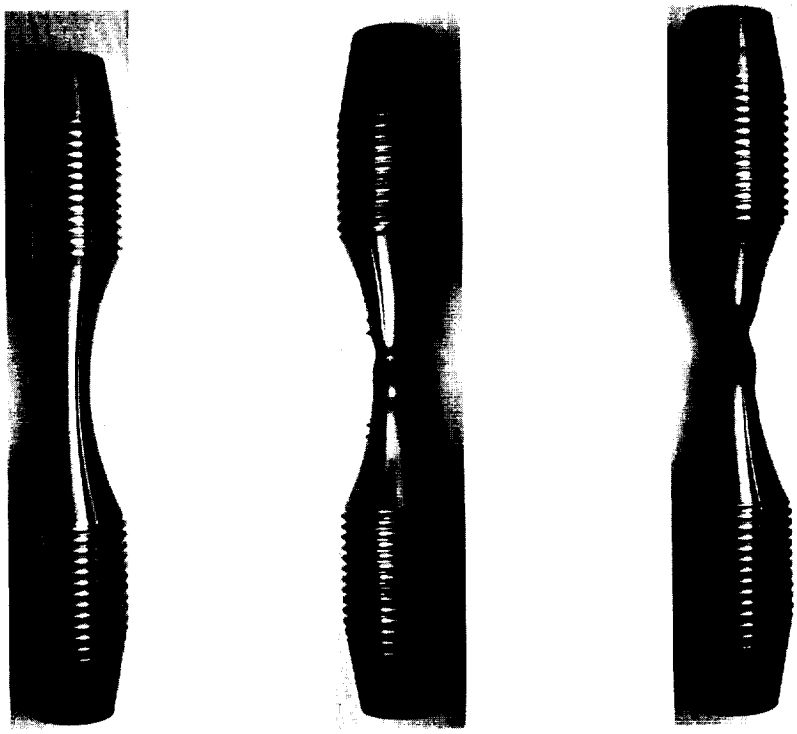

Pre-test | TCOP Test A-11 | TCOPS Test A-50

Figure 55. Relative geometry change for ASTAR 811C alloy tested with simultaneous and sequential (square wave) out-of-phase thermal cycling. Specimens shown actual size.

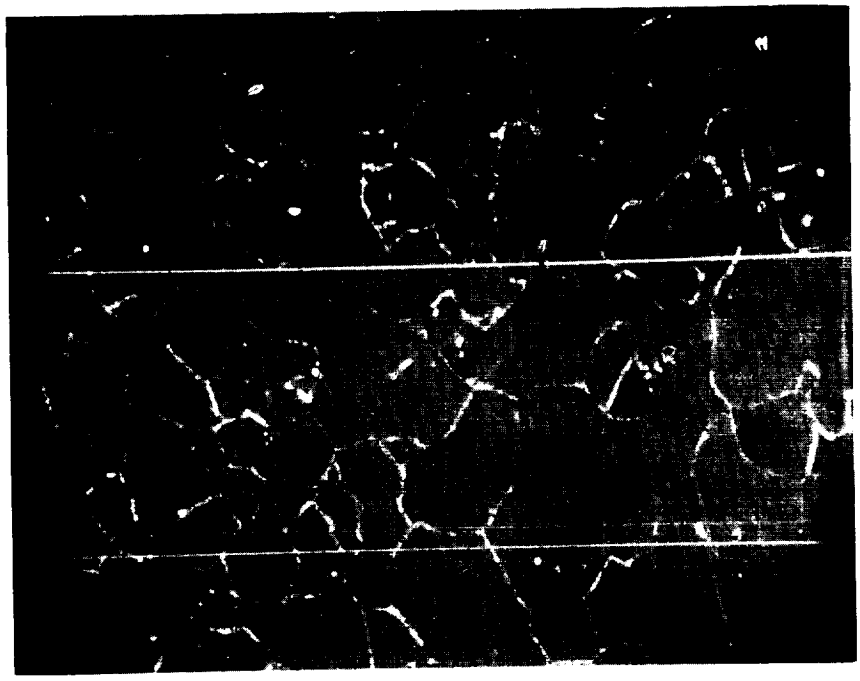

(a) 500X

Tensile Axis

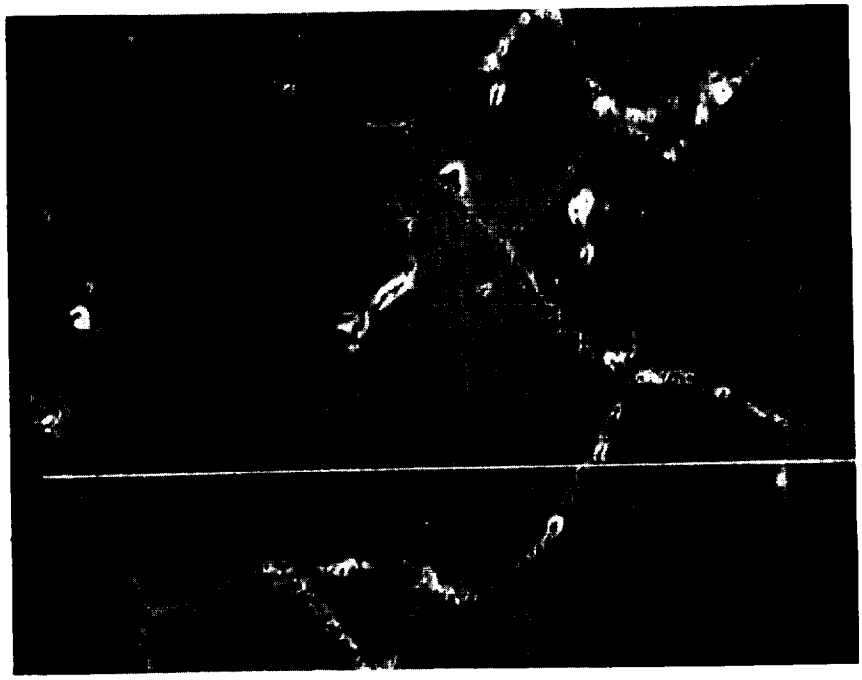

(b) 2000X

Figure 56. Fatigue damage in T-111 specimen No. 17 tested isothermally at 2100°F (1422°K) with a total longitudinal strain range of .131 in/in (mm/mm). Cycles to failure = 10. Area of observation approximately 1 mm below fracture surface.

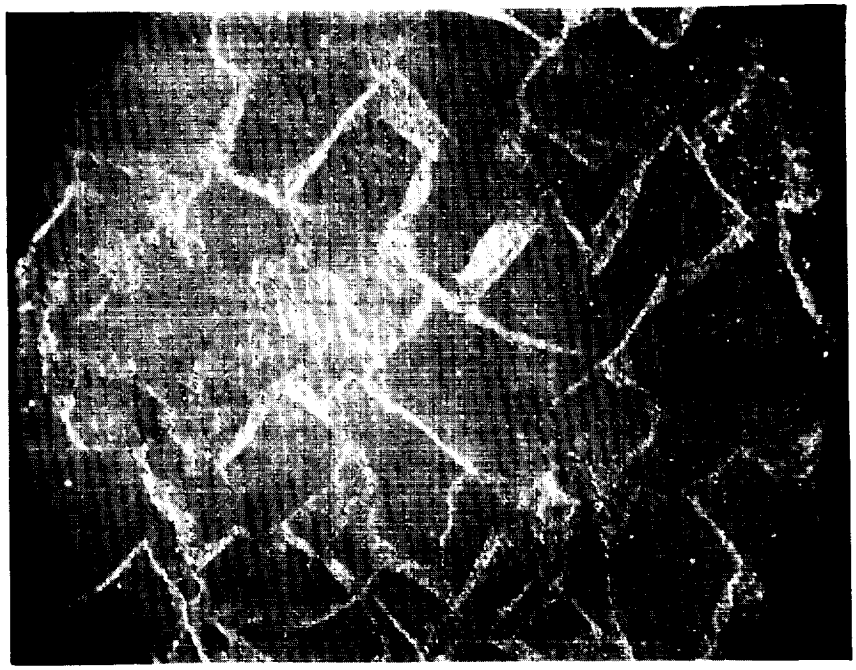

(a) 500X

Tensile Axis

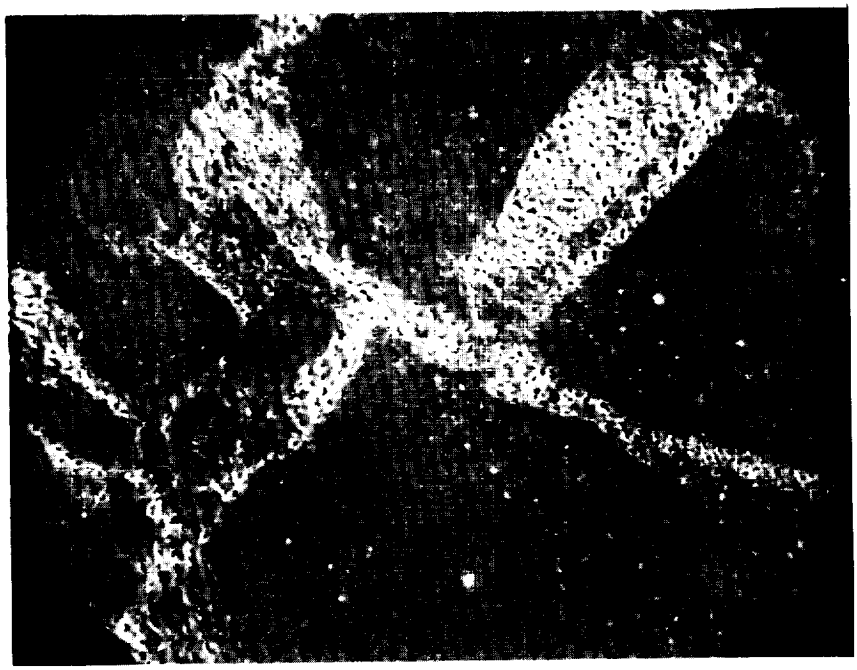

(b) 2000X

Figure 57. Fatigue damage in T-111 specimen No. 16 fatigue tested isothermally at 2100°F (1422°K) with a total longitudinal strain range of .018 in/in (mm/mm). Cycles to failure = 796. Area of observation was region of maximum damage in specimen interupted immediately prior to complete separation.

and appeared to occur by linking of the R-type voids generated by reversed grain boundary sliding (Figure 58).

Microstructural damage was minimal in the ASTAR 811C alloy tested at 2100°F (1422°K) (Figure 59). Both intergranular (Figure 60a) and transgranular (Figure 60b) fractures were observed, which indicated that the 2100°F (1422°K) test temperature was just at the threshold of significant creep effects in fatigue of the ASTAR 811C alloy. The observed difference in grain boundary damage between the two alloys was consistent with previous results which showed lower susceptability to grain boundary sliding in creep of the ASTAR alloy (1,2). This improved grain boundary strength was attributed to the presence of the grain boundary carbide (Figure 2), which provided a grain boundary pinning effect. It should be noted, however, that grain boundary sliding, though minimal, does occur in ASTAR 811C at 2100°F (1422°K) and that this sliding had a significant influence on the fatigue life of this alloy in the thermal cycled tests discussed below.

b. In-Phase Thermal Cycle Damage

The scanning electron micrographs presented in Figures 61 through 66 revealed the cause of the in-phase thermal cycled fatigue life degradation effect observed in both alloys (Figures 26 and 39). These photomicrographs showed that both alloys sustained massive grain boundary decohesion under the influence of thermal-mechanical cycles where the high temperature deformation occurred in tension and the low temperature deformation in compression. Examples of this effect in T-111 alloy are shown in Figures 61 through 64. Comparison of Figures 61 and 62 shows that the amount of in-phase damage in T-111 increased with increasing cycles to failure. A stereographic pair of the triple point crack seen in the center of the field of view in Figure 62b clearly shows the almost continuous nature of the grain boundary voids developed by in-phase cycling (Figure 63). Fracture of in-phase cycled T-111 alloy occurred by link-up of the grain boundary cracks and was thus intergranular in nature (Figure 64). Similar grain boundary damage was found in ASTAR 811C (Figure 65). Because of the higher resistance to grain boundary sliding in this alloy, the amount of damage was lower, which was assumed to be the reason for the higher resistance to the thermal-cycled life degradation effect noted in Figure 50. As with the isothermal cycling, in-phase thermal cycled fracture of the ASTAR 811C occurred by a mixed mode, with intergranular fracture caused by the link-up of grain boundary voids providing the majority of observed cracking (Figure 66).

It is assumed that the massive grain boundary decohesion seen with in-phase testing is caused by unreversed grain boundary sliding. It is relatively easy to envision how this effect could occur in a square wave test in which all of the tensile deformation takes place at a high temperature where grain boundary sliding occurs and all of the compressive deformation takes place at a low temperature where grain boundary sliding does not occur. With this type of test cycle, every tensile excursion causes

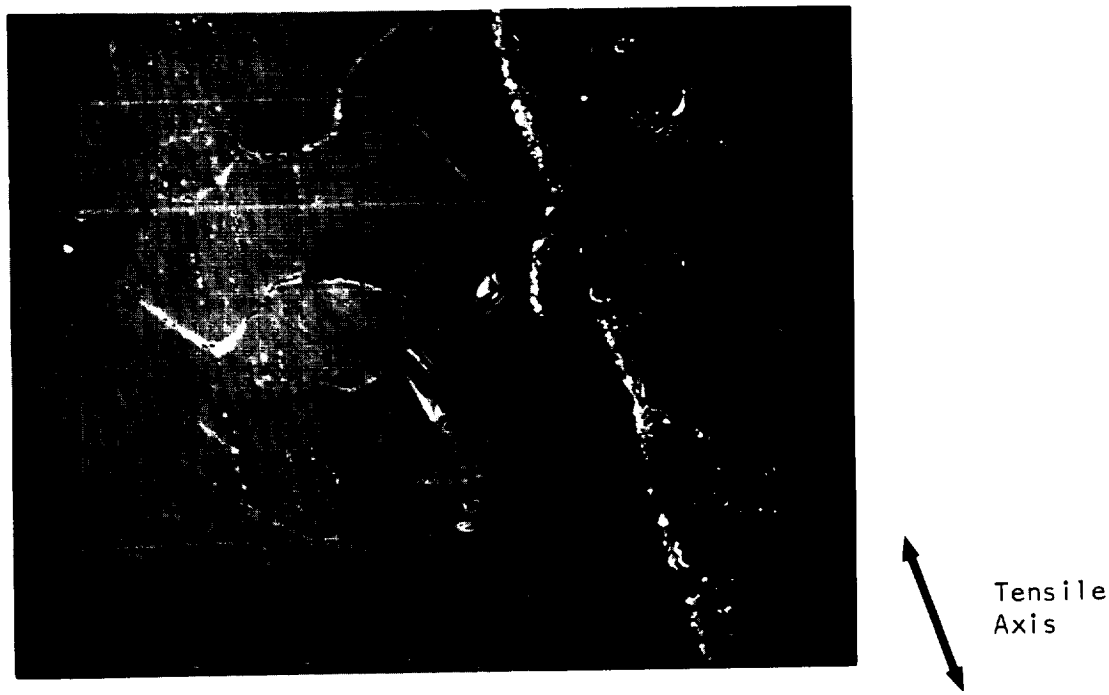

Figure 58. Secondary crack in T-111 specimen No. 17 fatigue tested isothermally at 2100°F (1422°K) with a total longitudinal strain range of .131 in/in (mm/mm). Cycles to failure = 10. Area of observation approximately .1 mm below fracture surface.

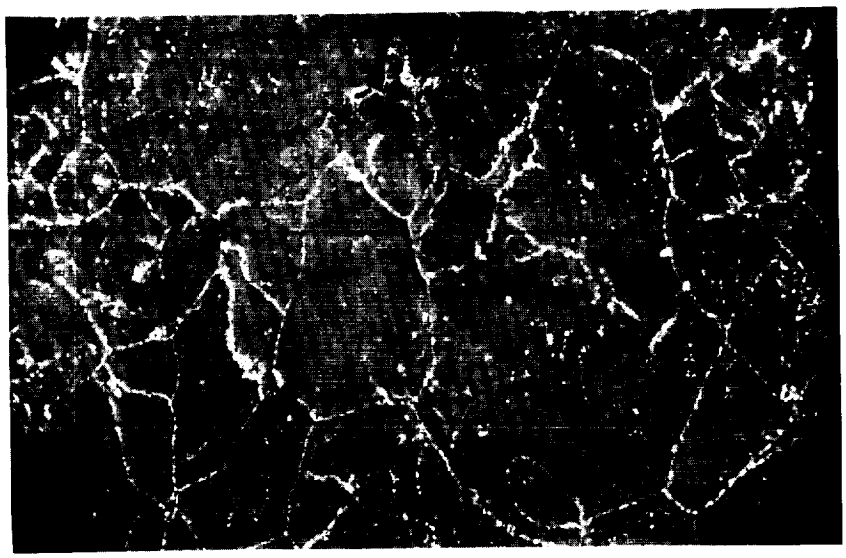

(a) 500X

Tensile Axis

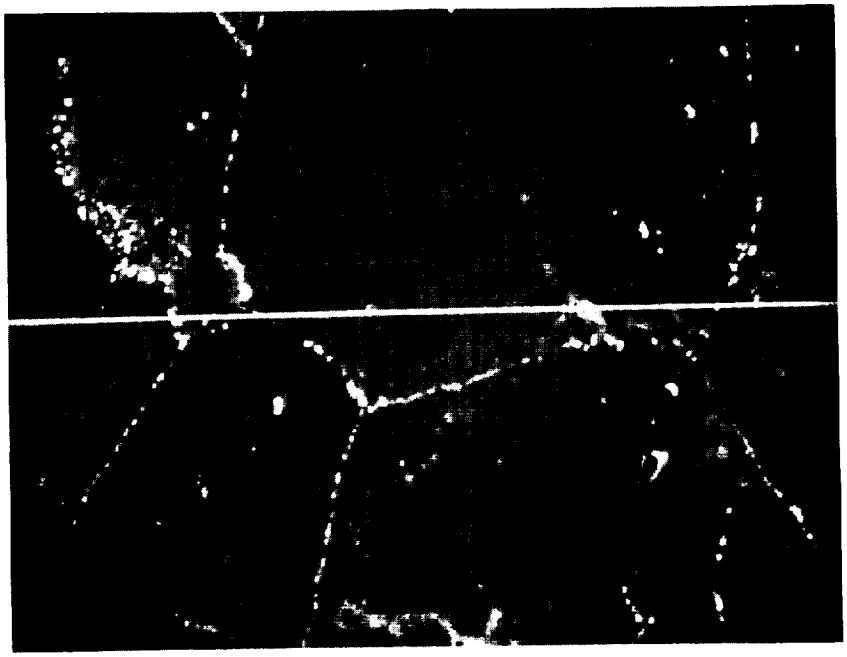

(b) 2000X

Figure 59. Microstructure of ASTAR 811C fatigue specimen No. 6 fatigue tested isothermally at 2100°F (1422°K) with a total longitudinal strain range of .034 in/in (mm/mm). Cycles to failure = 628. Area of observation immediately adjacent to fracture surface.

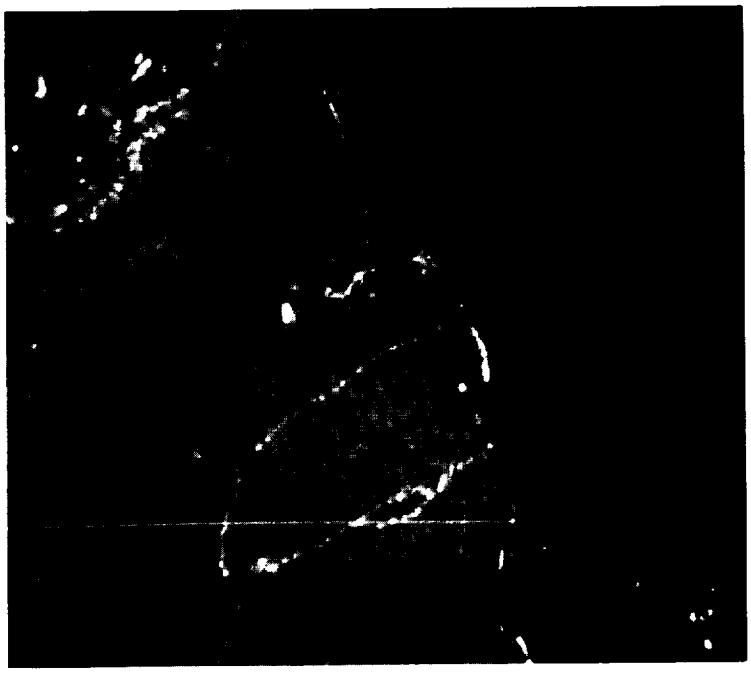

(a) Intergranular crack initiation 500X

Tensile Axis

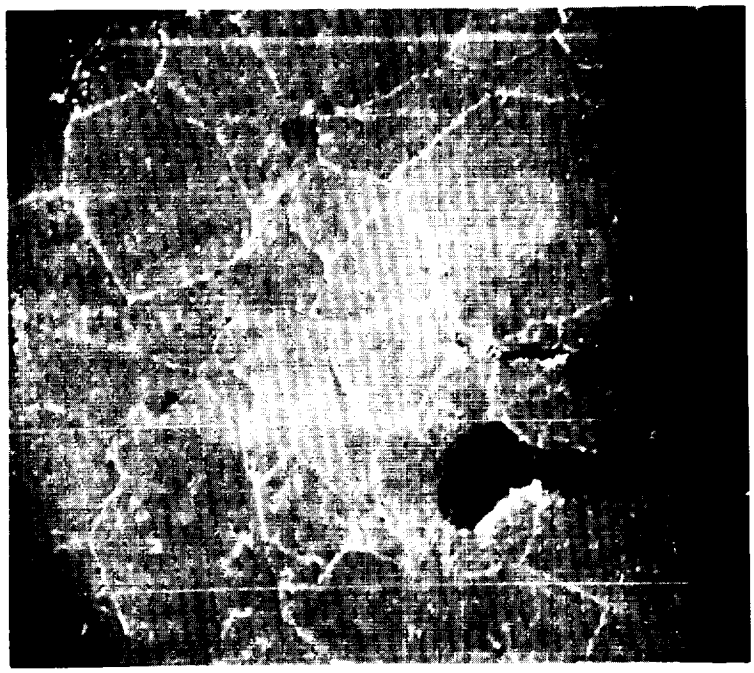

(b) Transgranular Crack Initiation 2000X

Figure 60. Secondary crack initiation in ASTAR 811C specimen No. 6 fatigue tested isothermally at 2100°F (1422°K) with a total longitudinal strain range of .034 in/in (mm/mm). Cycles to failure = 628

(a) 500X

Tensile Axis

(b) 2000X

Figure 61. Grain boundary decohesion in T-111 specimen No. 23 fatigue tested with in-phase thermal cycling (heating with tension, cooling with compression) at a total longitudinal strain. range of .035 in/in (mm/mm). Cycles to failure = 15. Area of observation approximately 1 mm below fracture surface.

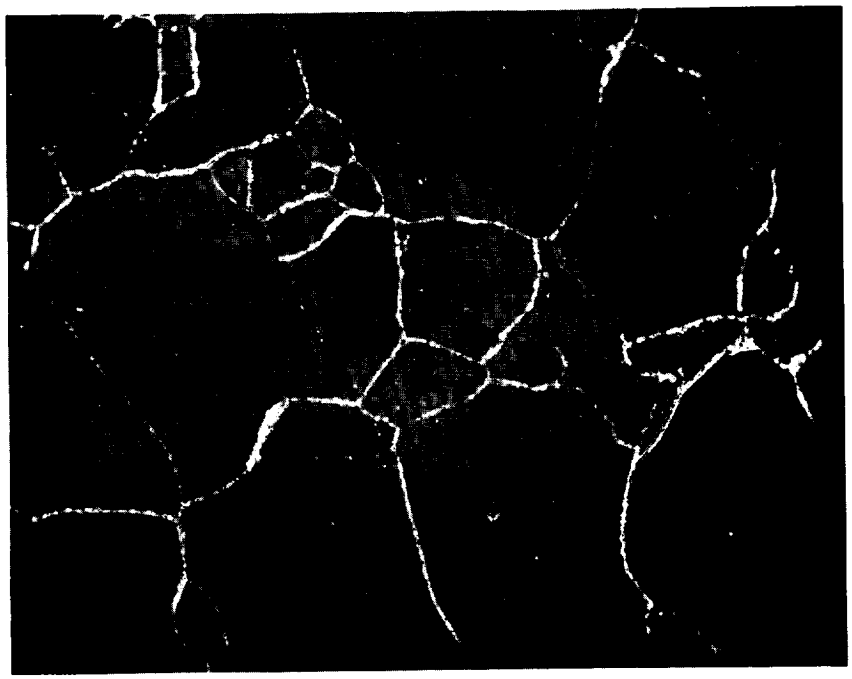

(a) 500X

Tensile Axis

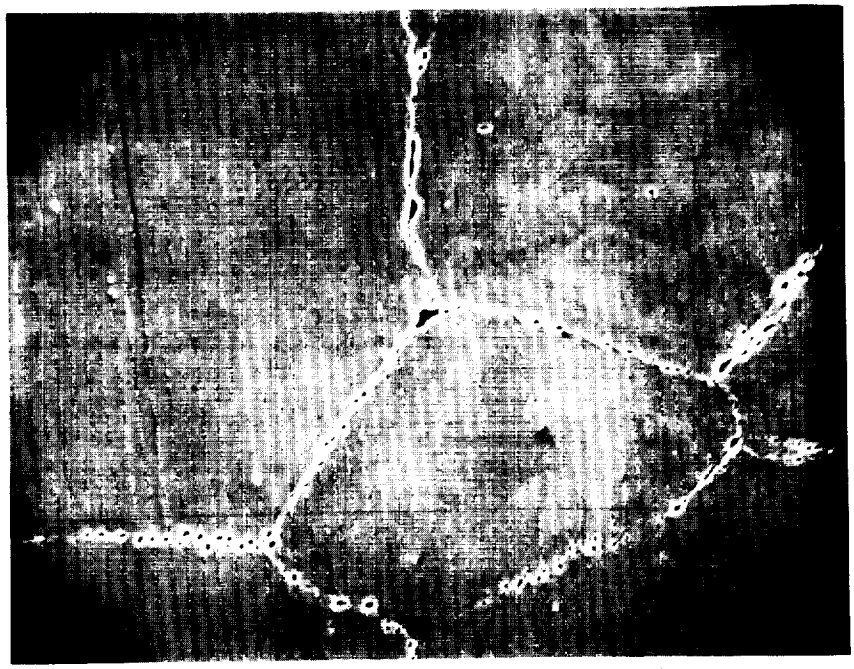

(b) 2000X

Figure 62. Grain boundary decohesion in T-111 specimen No. 28 fatigue tested with in-phase thermal cycling (heating with tension, cooling with compression) at a total longitudinal strain range of .0064 in/in (mm/mm). Cycles to failure = 456. Area of observation approximately 1 mm below fracture surface.

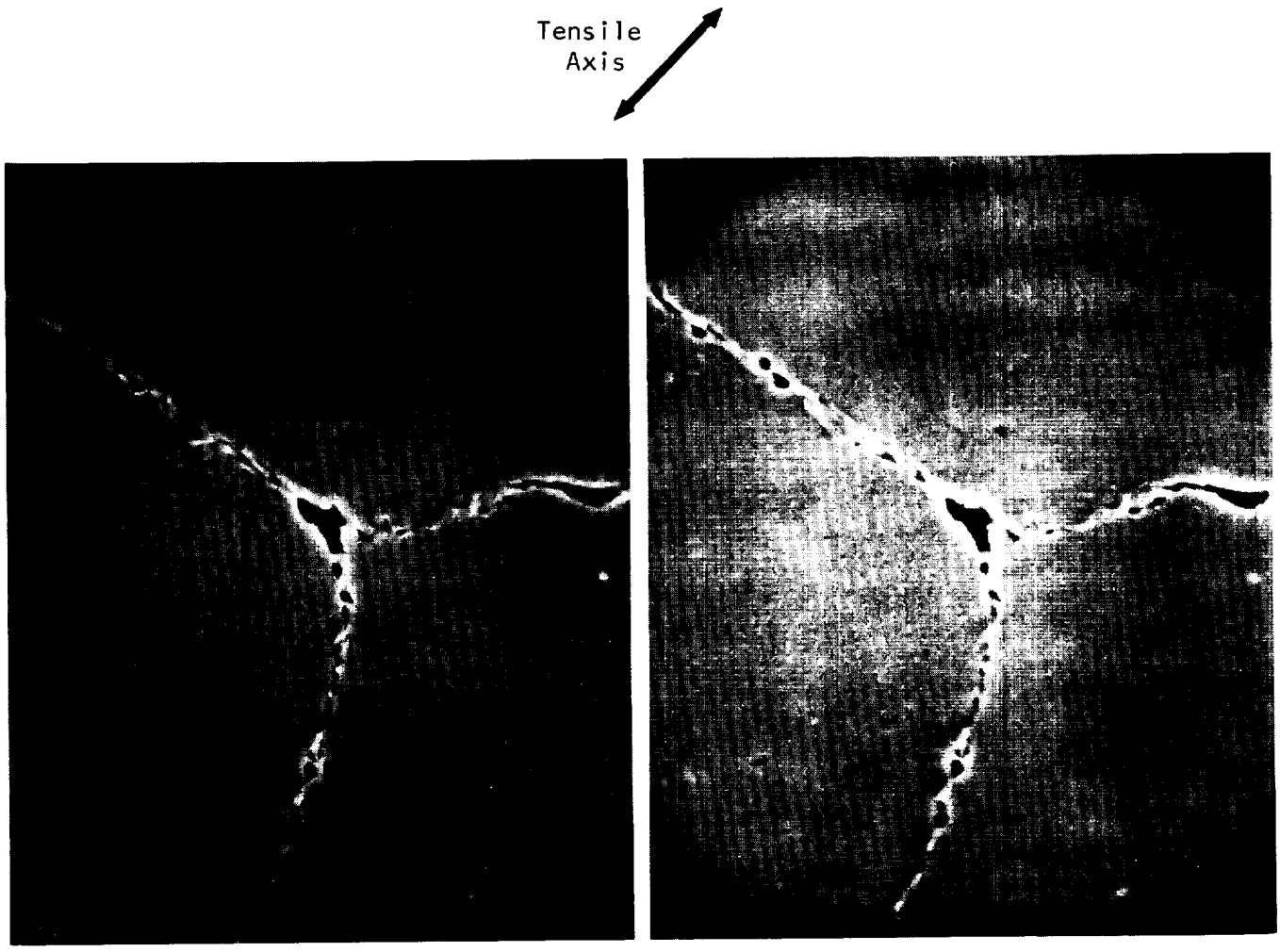

Figure 63. Stereo pair showing detail of grain boundary damage in T-111 specimen No. 28 fatigue tested with in-phase thermal cycling (heating with tension, cooling with compression) at a total longitudinal strain range of .0064 in/in (mm/mm) Cycles to failure = 456. Magnification 5000X

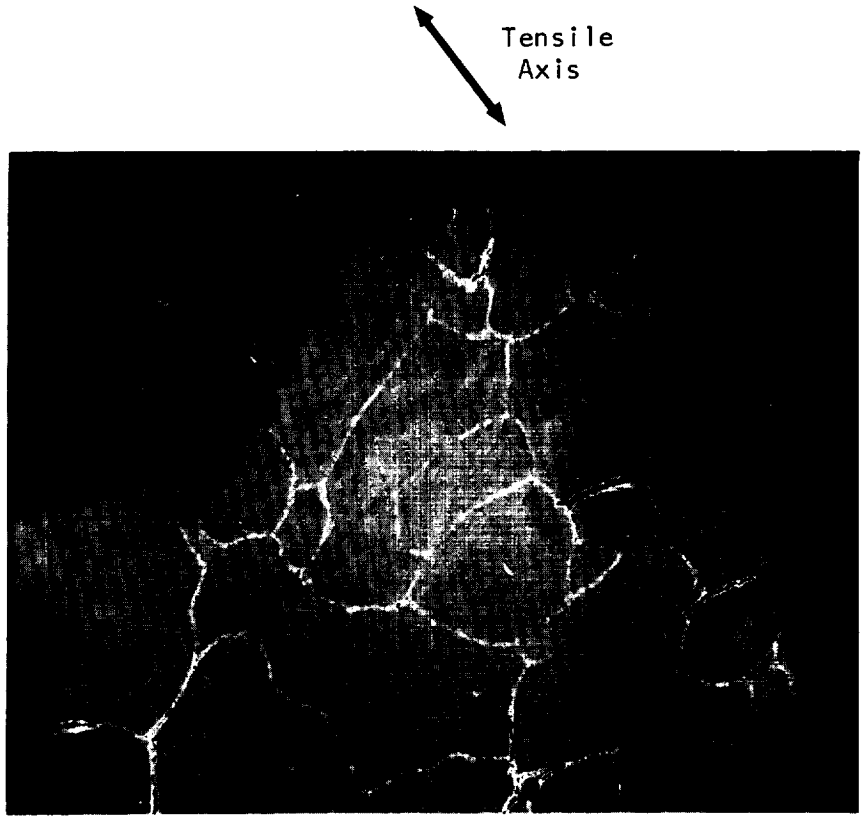

Figure 64. Primary and secondary fractures in T-111 specimen No. 28 fatigue tested with in-phase thermal cycling (heating with tension, cooling with compression) at a total longitudinal strain range of .0064 in/in (mm/mm). Cycles to failure = 456. Magnification 500X

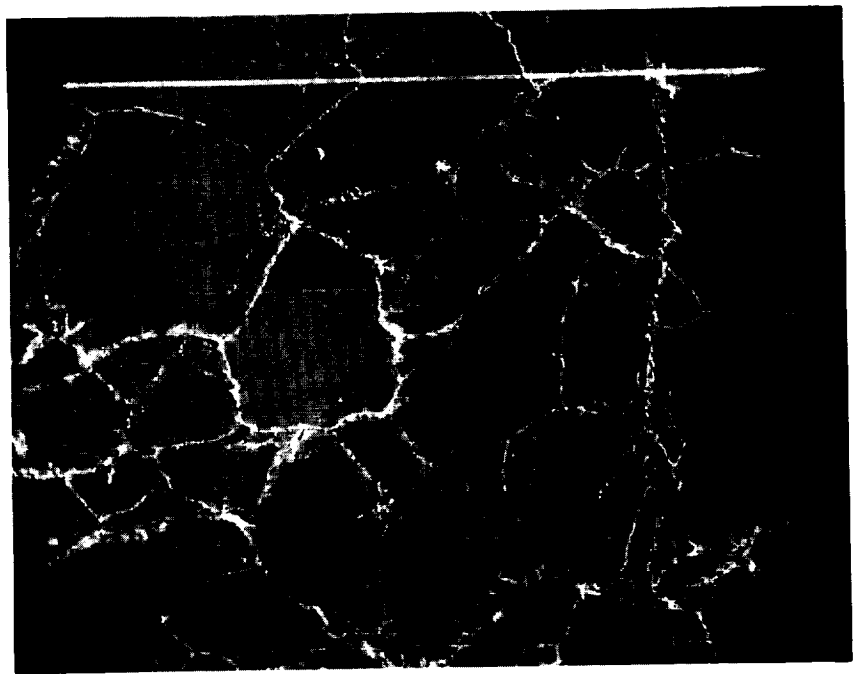

(a) 500X

Tensile Axis

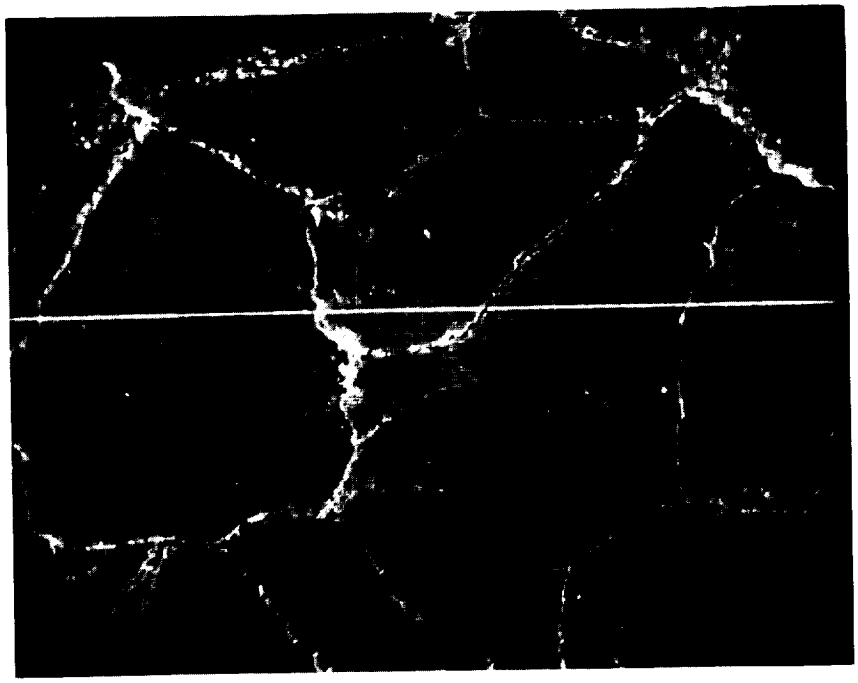

(b) 1000X

Figure 65. Grain boundary decohesion in ASTAR 811C specimen No. 17 fatigue tested with in-phase thermal cycling (heating with tension, cooling with compression) at a total longitudinal strain range of .0096 in/in (mm/mm). Cycles to failure = 939. Area of observation approximately 1 mm below fracture surface.

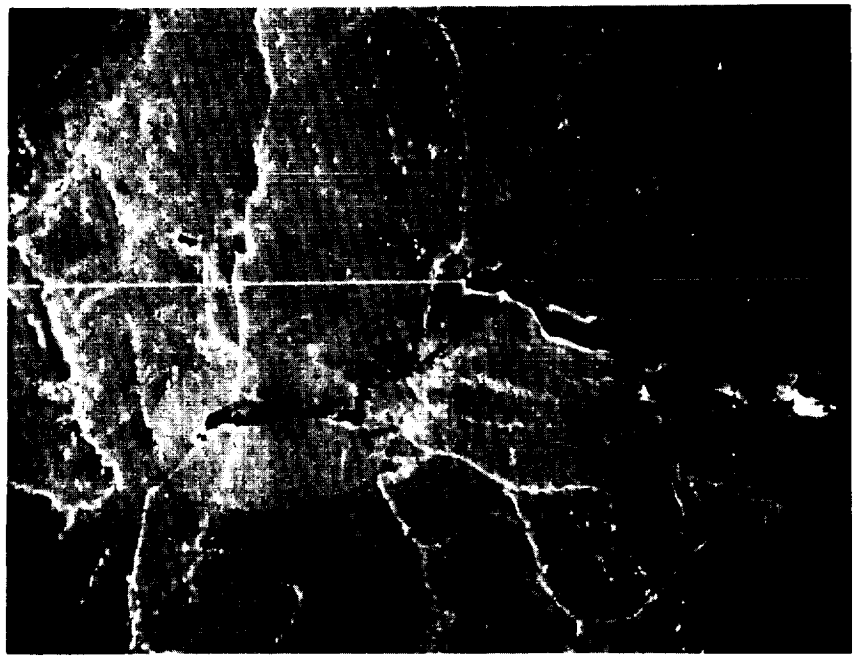

Figure 66. Illustration of mixed-mode cracking in ASTAR 811C specimen No. 17 fatigue tested with in-phase thermal cycling (heating with tension, cooling with compression) at a total longitudinal strain range of .0096 in/in (mm/mm). Cycles to failure = 939. Area of observation approximately .2 mm below primary fracture surface. Magnification 1000X

a small grain boundary displacement which is not reversed in compression, and these individual increments accumulate to cause the gross cavity formation and decohesion seen in the scanning electron micrographs. It is more difficult to explain unreversed grain boundary sliding in the TCIP type test, where temperature and strain vary simultaneously. However, the occurrence of this phenomenon can be understood by analysis of the relationship between temperature and plastic strain, which does not vary linearly with temperature as does total strain. This point is illustrated in Figure 67, which shows the tensile and compressive elastic and plastic strain components which occur at or above the equicohesive temperature. This figure shows that all of the tensile deformation which occurs above the equicohesive temperature is plastic, while a significant part of the compressive deformation above this temperature is elastic. This analysis thus shows how a net difference can exist between the tensile and compressive components of plastic strain which occur above the equicohesive temperature, and how this type of thermal cycling can cause unreversed grain boundary displacements in exactly the same way as the square wave type of cycle. However, because the amount of unreversed creep strain is less in the TCIP type of cycle than in the square wave cycle, the fatigue life degradation should be smaller, as was observed to be the case experimentally (Figure 39).

Manson, Halford, and Hirshberg have recently developed the above arguments in a formalized analysis which they call a method of Partitioned Strain Ranges (9,10,11). This method seeks to evaluate in a quantitative way the amount of unreversed creep deformation in a particular fatigue cycle, and to correlate data from different cycle types on this basis. A more detailed description of this analysis is presented in a later section of this report, where the method is applied to the ASTAR 811C data generated on this program.

c. Out-Of-Phase Thermal Cycle Damage

Significant microstructural damage was found in both alloys tested with out-of-phase thermal cycling as shown in Figures 68 and 69. The damage was more extensive near the center of the "bulge" which developed in this type of test, as illustrated in Figure 51b, and as shown by comparing Figure 68 with Figure 70. The damage increased with increasing cycles to failure, as shown by comparing Figures 68 and 71. Failure was intergranular in the T-111 alloy (Figure 72) while both intergranular and transgranular cracking were observed in the ASTAR 811C alloy (Figure 73), with intergranular fracture being the predominant mode. While microstructural damage undoubtedly contributed to failure in the out-of-phase tests, the fact that failure occurred at the zone of reduced cross-sectional area rather than at the location of maximum microstructural damage supports the previous argument that the geometric instability was the primary cause of the life reductions which occurred in the majority of these tests.

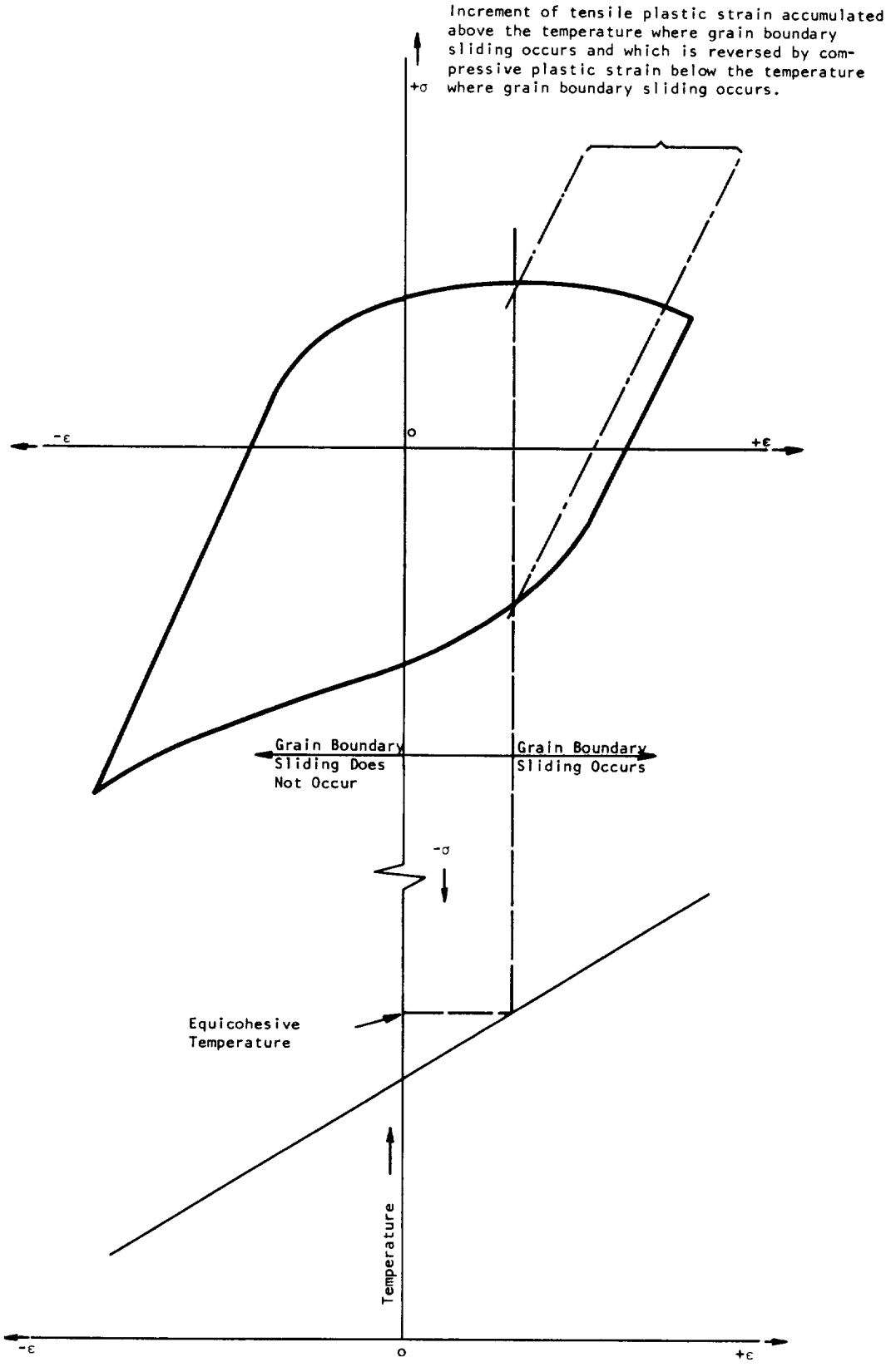

Figure 67. Schematic illustration of the relationship between temperature, plastic strain, and total strain which shows how unreversed grain boundary sliding can occur in a test where temperature and strain vary simultaneously in a linear, in-phase relationship. (TCIP type cycle).

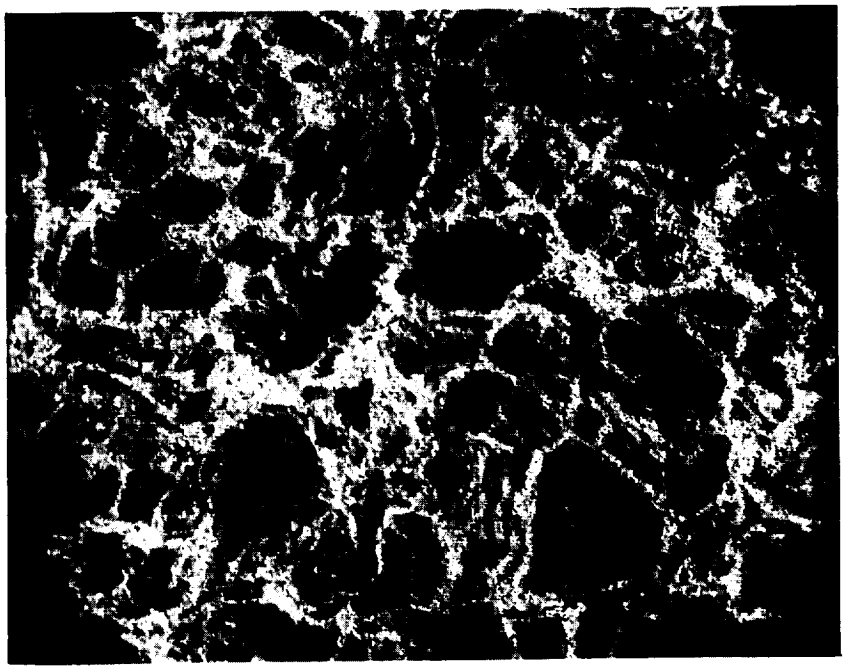

(a) 500X

Tensile Axis

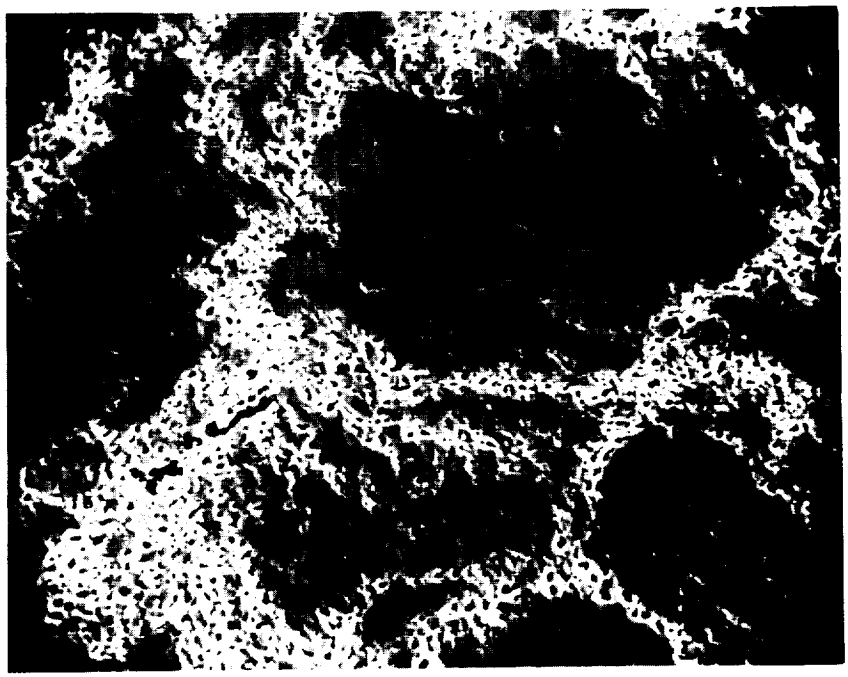

(b) 2000X

Figure 68. Microstructural damage in the center of the "bulge" developed in T-111 specimen No. 30 tested with out-of-phase thermal cycling at a total longitudinal strain range of .035 in/in (mm/mm). Cycles to failure = 567.

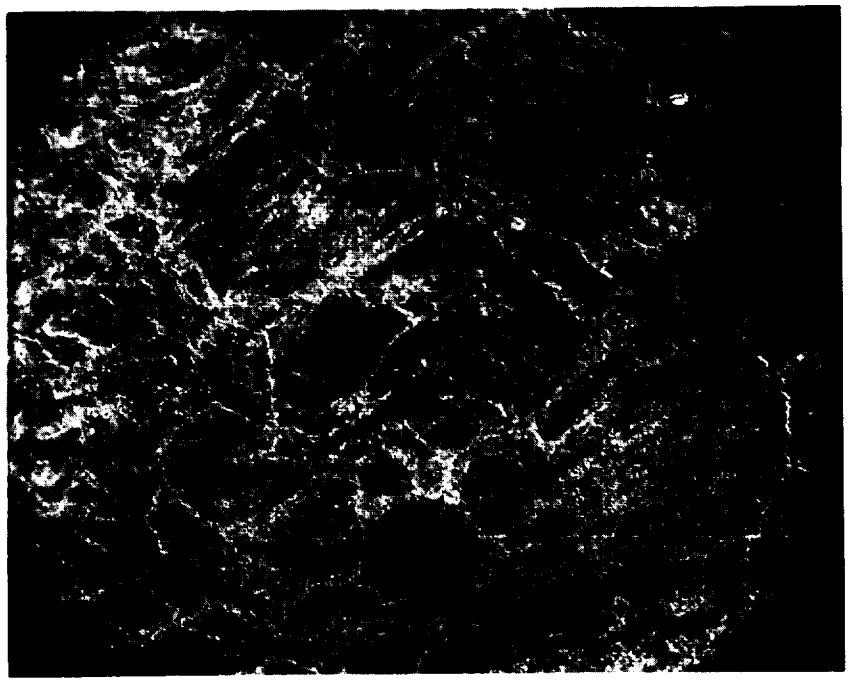

(a) 500X

Tensile Axis

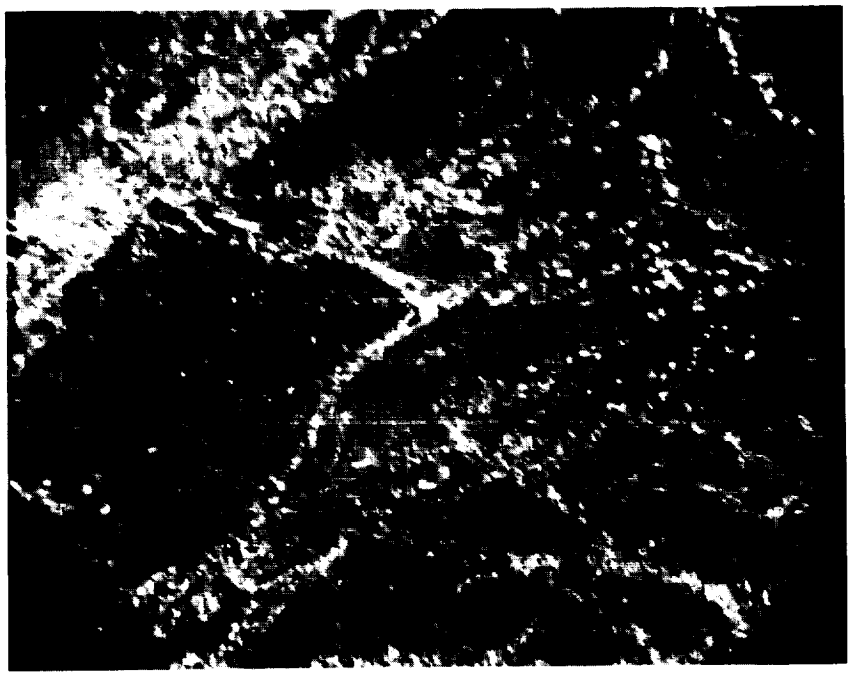

(b) 2000X

Figure 69. Microstructural damage in the center of the "bulge" developed in ASTAR 811C specimen No. 12 tested with out-of-phase thermal cycling at a total longitudinal strain range of .018 in/in (mm/mm). Cycles to failure = 1012.

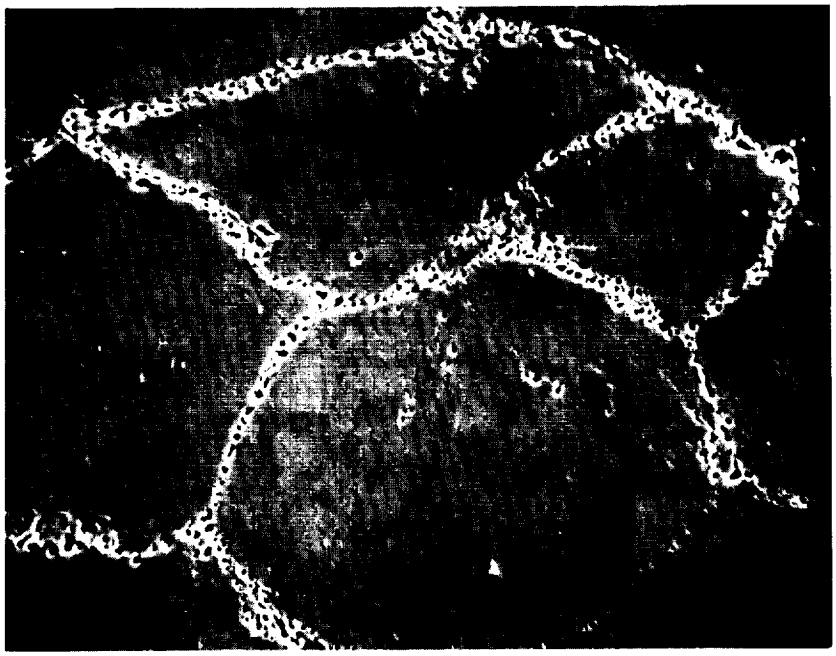

Tensile Axis

2000X

Figure 70. Microstructural damage in the center of the secondary "neck" developed in T-111 specimen No. 30 tested with out-of-phase thermal cycling at a total longitudinal strain range of .035 in/in (mm/mm). Cycles to failure = 567.

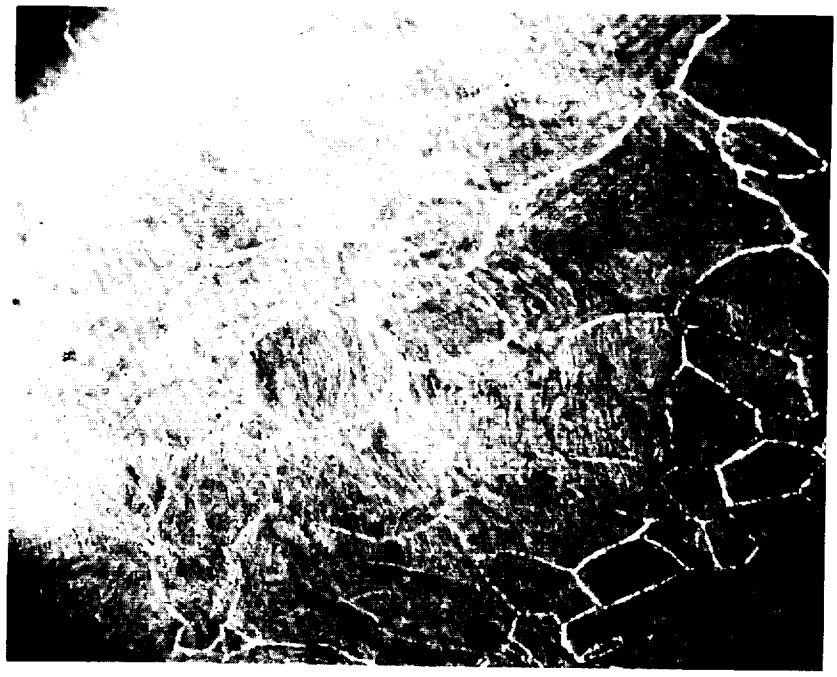

(a) 500X

Tensile Axis

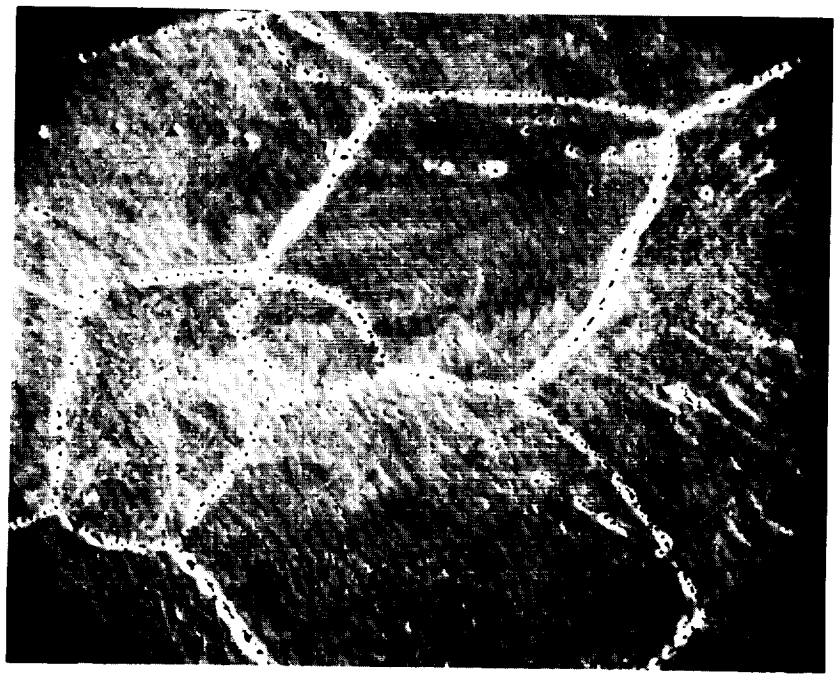

(b) 2000X

Figure 71. Microstructural damage in the center of the "bulge" developed in T-111 specimen No. 33 tested with out-of-phase thermal cycling at a total longitudinal strain range of 0.100 in/in (mm/mm). Cycles to failure = 9.

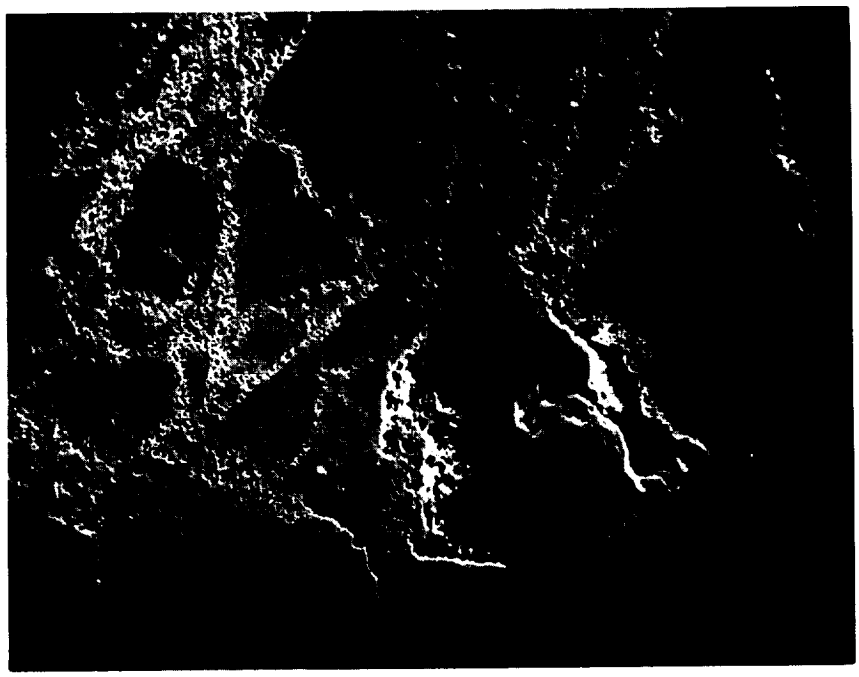

Tensile Axis

1000X

Figure 72. Secondary cracking in T-111 specimen No. 30 tested with out-of-phase thermal cycling at a total longitudinal strain range of 0.035 in/in (mm/mm). Cycles to failure = 567.

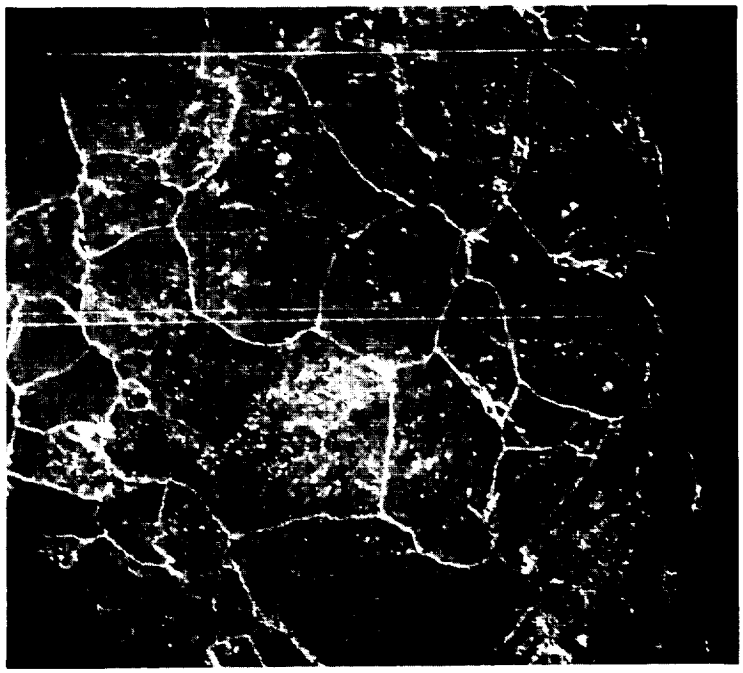

Tensile Axis

500X

Figure 73. Secondary cracking in ASTAR 811C specimen No. 12 tested with out-of-phase thermal cycling at a total longitudinal strain range of 0.018 in/in (mm/mm). Cycles to failure = 1012.

3. Chemical Analysis of Tested Specimens

Chemical analysis of selected test specimens for the interstitials carbon, oxygen, nitrogen, and hydrogen showed minor changes in composition during testing (Tables 12 and 13). Both alloys experienced a drop in the oxygen and nitrogen levels and a slight increase in the hydrogen level. The T-111 showed a possible slight carbon decrease while the ASTAR 811C showed no consistent change in carbon level. Because of the fact that these compositional changes were observed over the entire range of basic cycle types studied, it was assumed that they were not associated with the observed variations of fatigue life with varying thermal cycles.

D. Analysis by the Method of Partitioned Strain Ranges

In the previous discussion of unreversed grain boundary sliding reference was made to a new approach for the characterization of cyclic plasticity which was recently developed by Manson, Halford, and Hirshberg (9,10,11). This section of the report will describe this approach, which is called the method of partitioned strain ranges, and its application to the ASTAR 811C fatigue results from this program.

The method of strain range partitioning is based on separation of the reversed plastic strain range into components which represent both the direction and the nature of the deformation; that is, whether it is tensile or compressive and whether it occurs by a creep or a plastic flow mechanism. The critical point of the argument involves not the nature of the deformation as such, but how the deformation is reversed in the fatigue cycle. Four types of reversed strain are defined; they are plastic strain reversed by plastic strain (PP), creep strain reversed by creep strain (CC), tensile creep strain reversed by compressive plastic strain (CP), and tensile plastic strain reversed by compressive creep strain (PC). PP strain is experienced at low temperatures, where creep does not occur, or at a high temperature and frequency where thermally activated flow is prohibited. CC deformation occurs in a low frequency, high temperature cycle where the strain rate is low enough that essentially all of the inelastic strain occurs by creep. Pure CP and PC types of deformation would be found in cycles such as the square wave tests applied in this program, where all of the deformation in one direction occurs at a low temperature and all of the reverse deformation takes place at a high enough temperature and low enough strain rate so that all of the reversed strain occurs by a thermally activated flow mechanism. Another test where this type of deformation might occur would be an isothermal cycle where the tensile and compressive strain rate are not equal so that one half of the cycle sustains more creep deformation than the other half. On the basis of the present study, which showed that the primary effects of high temperature fatigue deformation were associated with grain boundary sliding, it appears that the more relevant separation of plastic strain might involve homogeneous and inhomogeneous (grain boundary) flow

Table 12

Influence of Vacuum Fatigue Exposure on Interstitial Contamination in T-111 Alloy

Specimen No.	Test Cycle	Analysis, ppm C	O	N	H
As Received					
Vendor	-	<30	<50	17	1.3
TRW	-	80	33	35	5
T-111-14	ISOT	15	3	3	*
T-111-16	ISOT	23	2	3	5
T-111-17	ISOT	53	2	3	*
T-111-18	ISOT	32	1	4	8
T-111-22	TCIP	18	2	3	8
T-111-23	TCIP	20	3	3	11
T-111-28	TCIP	49	2	5	9
T-111-30	TCOP	38	2	4	*

* Insufficient tested material available to perform analysis.

Table 13

Influence of Vacuum Fatigue Exposure on Interstitial Contamination in ASTAR 811C Alloy

Specimen No.	Test Cycle	Analysis, ppm C	O	N	H
As Received					
Vendor	-	230	100	12	1.4
TRW	-	290	22	9	3
ASTAR 811C-3	ISOT	260	.3	3	*
ASTAR 811C-6	ISOT	230	.8	5	*
ASTAR 811C-8	ISOT	220	.5	3	9
ASTAR 811C-9	TCOP	250	.5	4	*
ASTAR 811C-12	TCOP	230	.6	8	10
ASTAR 811C-15	TCIP	260	.9	4	*
ASTAR 811C-17	TCIP	200	1.0	6	9
ASTAR 811C-24	TCIP	240	.6	7	7

* Insufficient tested material available to perform analysis.

rather than thermally activated non-thermally activated deformation. However, this is a relatively fine point in the argument, since the equicohesive temperature for most materials is generally not much above the minimum temperature for significant creep to occur, and grain boundary sliding is therefore almost always associated with creep deformation.

The basic hypothesis of the method of partitioned strain ranges is that each of the four types of reversed strain defined above will provide a different fatigue life for a given material at a given strain amplitude. Thus, it should be possible to generate a plot of strain range versus cycles to failure for each type of reversed strain, from which the life of a more complicated hysteresis loop involving more than one reversed strain component might be determined. The equation proposed by Manson for relating the life provided by each type of strain component to the life anticipated in a test involving two or more types of reversed strain is a simple linear summation of reciprocal life fractions (11). For example, with a test involving both PP and CP deformation, the equation would be:

$$\frac{f_{pp}}{N_{pp}} + \frac{f_{cp}}{N_{cp}} = \frac{1}{N_f}$$

where f_{pp} and f_{cp} are the fractions of PP and CP type deformation present in the experimental hysteresis loop, N_{pp} and N_{cp} are the fatigue lives of the material tested with pure PP and CP deformation, and N_f is the predicted fatigue life.

An example of a hysteresis loop which contains more than one type of reversed strain has already been presented in Figure 67 which illustrated how unreversed grain boundary sliding could occur in a TCIP type cycle. Actually, this particular example involved three of the four reversed strain components defined in the partitioning method, as shown in Figure 74 where the hysteresis loop used in the previous example has been reproduced with the assumption that the equicohesive temperature coincides with the minimum temperature for significant creep. The three reversed strain components present in this loop are the PP, CC, and CP types, as indicated in Figure 74. An analogous partitioning can be performed to show that PP, CC, and PC types of deformation are present in the TCOP type of cycle applied in this program.

Application of the method of partitioned strain ranges to the ASTAR 811C alloy fatigue results involved several assumptions. First, it was assumed that at the 0.0065 Hz frequency all of the deformation which occurred below 1600°F (1144°K) was plastic, and all of the deformation above that temperature was thermally activated. This sharp cut-off temperature is somewhat arbitrary, but in general, it represents a good estimate of the minimum temperature where creep may be anticipated in this alloy (1).

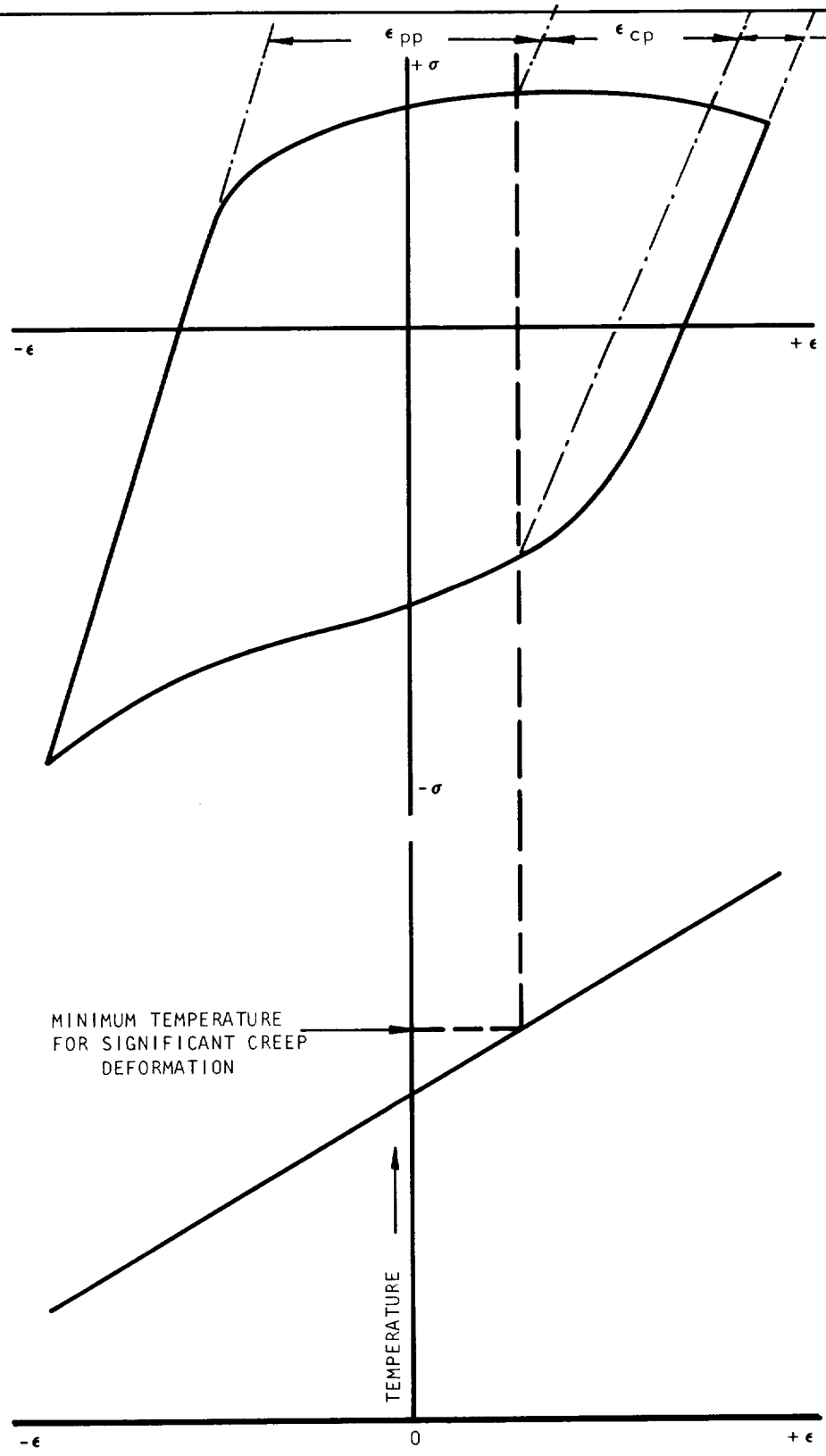

Figure 74. Schematic illustration of the PP, CP, and CC strain components present in a typical TCIP hysteresis loop.

Based on this assumption, the 2100°F (1422°K) isothermal test results should represent pure CC deformation, while the in-phase and out-of-phase square wave test results should represent respectively pure CP and PC deformation. Both the 400°F (478°K) and 2100°F (1422°K) isothermal high frequency (0.65 Hz) cycles should provide a reasonable representation of the PP fatigue life. Actually, these two cycle types produced somewhat different lives, with the low temperature tests falling near the bottom of the isothermal scatter band, while the high frequency results were near the top of the band except at the lowest strain amplitude. Because of this uncertainty in the location of the PP line, and also because of the relatively narrow band into which all of the isothermal results fell when compared to life differences caused by thermal cycled testing, it was decided to use the scatter band itself as representative of both the PP and CC types of deformation. In order to provide the most conservative possible predictions with respect to design applications, the bottom rather than the center of the band was used to obtain the required PP and CC lives.

Using the above assumptions, the pure CP, PC, and CC/PP data were used to calculate predicted lives for each of the 2100/400°F (1422/478°K) TCIP and TCOP tests conducted on the ASTAR 811C alloy. These calculations were simplified by the assumption of a coincident CC/PP line, since it eliminated the need to separate the CC and PP components in the TCIP and TCOP loops. Furthermore, at all but the lowest strain amplitudes all of the high temperature elastic strain occurred above 1600°F (1144°K), which meant that calculation of the percentage of unreversed creep strain for each test was reduced to a simple calculation of the total amount of elastic strain experienced between the high temperature strain reversal and 1600°F (1144°K). These strain values were calculated directly from load ranges measured from the experimental hysteresis loops using the high temperature modulus data from Figure 4.

The percentages of unreversed creep strain calculated by the above method are listed in Table 14 together with the pure fatigue life values for the relevant strain components and the observed and predicted fatigue lives for each test analyzed. The observed and predicted life values are compared graphically in Figure 75, where the predicted results have been represented by a smooth curve drawn through the calculated data points. The representations show excellent agreement between predicted and experimental lives for the out-of-phase tests, with somewhat poorer agreement being achieved for the in-phase results. It would thus appear that the microstructure of damage caused by the in-phase testing makes a somewhat more than linear contribution to the fatigue process in this material. This synergistic interaction between creep and fatigue is not surprising in view of the gross grain boundary damage caused by the in-phase cycling.

Table 14

Results of Strain Range Partitioning Calculations

Test No.	Cycle Type	Percentage of Unreversed Creep Strain	Fatigue Life with 100% Unreversed Creep Strain Cycles	CC/PP Fatigue Life Cycles	Predicted Fatigue Life Cycles	Experimental Fatigue Life, Cycles
A-12	TCOP	22.6	775	1800	1150	1012
A-21	TCOP	11.8	160	380	327	365
A-11	TCOP	6.0	34	76	70	61
A-9	TCOP	3.1	17	17	16	15
A-17	TCIP	29.4	280	13,000*	909	939
A-16	TCIP	22.6	170	2100	588	367
A-15	TCIP	10.9	52	380	225	132
A-14	TCIP	6.0	18	78	65	32
A-24	TCIP	3.3	6	18	16	13

* Estimated from extrapolated curve.

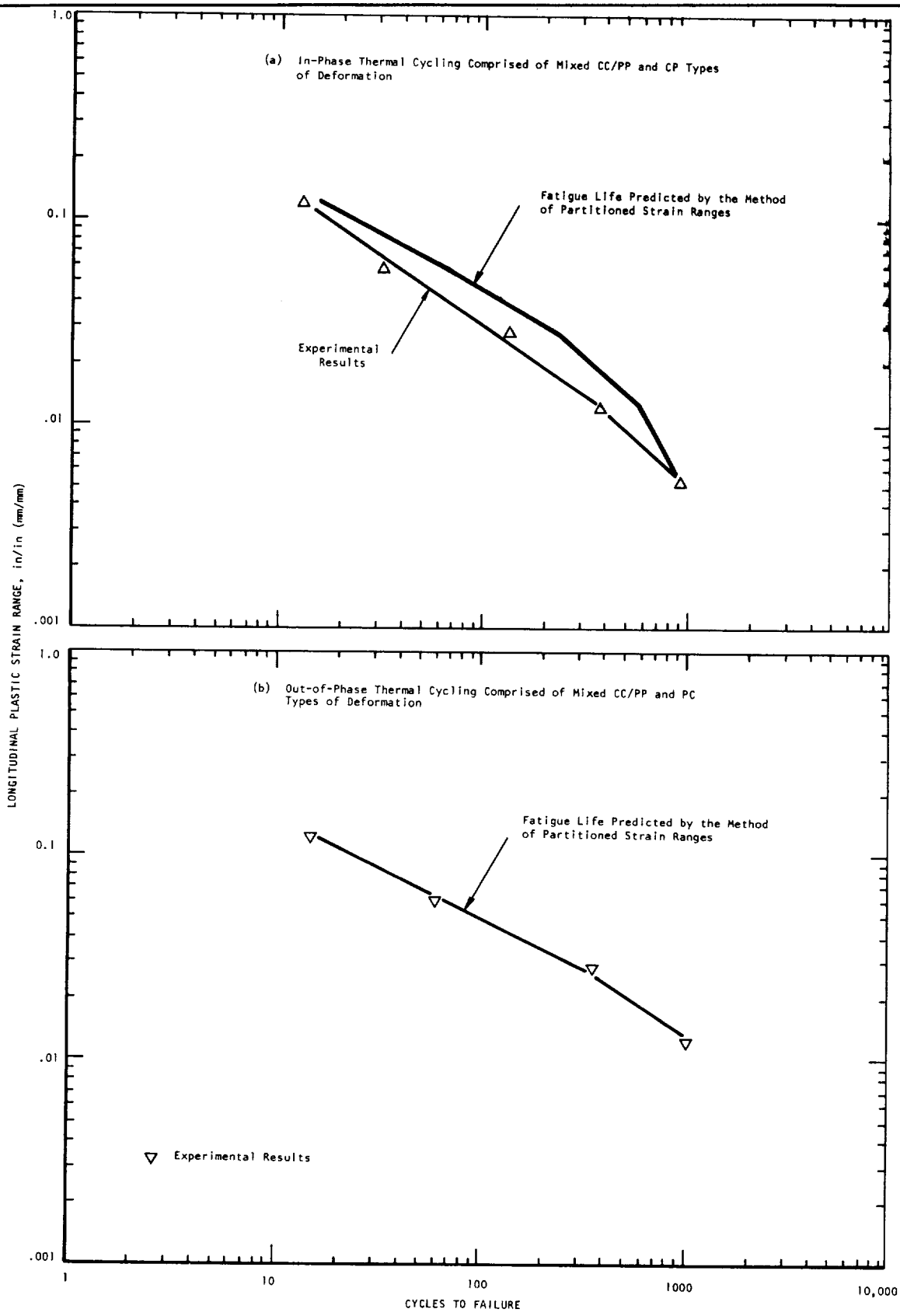

Figure 75. Comparison of fatigue life predictions based on the method of partitioned strain ranges with experimental results for ASTAR 811C alloy tested with simultaneous thermal cycling.

V CONCLUSIONS

The major conclusions obtained from this program concerned the relative influence of isothermal, in-phase, and out-of-phase thermal cycling on the fatigue life of the T-111 and ASTAR 811C alloys. In-phase thermal cycling (tension hot, compression cold) consistently reduced the fatigue life with respect to the isothermal life within the range of the thermal cycle, while out-of-phase cycling had both a beneficial and a detrimental effect, depending on the material and strain range. Analysis of the tested specimens showed that the in-phase life reduction was caused by massive grain boundary decohesion which resulted from unreversed grain boundary sliding. The ASTAR 811C alloy was less susceptable to this effect because of improved resistance to grain boundary sliding provided by grain boundary carbide precipitates. The out-of-phase life variations were found to be associated with a geometric instability which occurred in the hourglass specimens. Analysis of the fatigue results by the method of partitioned strain ranges showed that out-of-phase results could be predicted very accurately by this technique, with the in-phase predictions being somewhat less accurate.

The results of this study are considered extremely important because the observed life reductions were caused by an unreversed grain boundary sliding mechanism which should be operative in any material where the service temperature is cycled through the equicohesive temperature in-phase with a mechanical strain. Significant fatigue life reductions may thus be anticipated in any material which is exposed to this type of thermal cycling.

VI REFERENCES

1. K. D. Sheffler and R. R. Ebert, "Generation of Long Time Creep Data on Refractory Alloys at Elevated Temperatures," Semi-Annual Report, Contract NAS-3-15554, TRW ER-7567, NASA-CR-120867, January 1972. See also Contractor reports on NASA Contracts NAS-3-13469, NAS-3-9439, and NAS-3-2545, listed in Appendix I of CR 120867.

2. K. D. Sheffler, J. C. Sawyer, and E. A. Steigerwald, "Mechanical Behavior of Tantalum Base T-111 Alloy at Elevated Temperature," Trans. ASM, Vol. 62, 1969, p. 749.

3. S. S. Manson and G. R. Halford, "A Method of Estimating High-Temperature Low-Cycle Fatigue Behavior of Materials." Thermal and High-Strain Fatigue, the Metals and Metallurgy Trust, London, 154, 1967.

4. K. D. Sheffler, "Interaction Between Creep, Fatigue, and Strain Aging in Two Refractory Metal Alloys," Met. Trans., Vol. 3, 1972, p. 167.

5. L. F. Coffin, Jr., "Fatigue at Elevated Temperature," Keynote Address, The 1972 Symposium on Fatigue Elevated Temperatures, Storrs, Conn., June 18, 1972, In press.

6. L. F. Coffin, Jr. Private communication.

7. A. E. Carden and T. B. Slade, "High Temperature Low-Cycle Fatigue Experiments on Hastelloy X," Symposium on Fatigue at High Temperature," San Francisco, California, June 1968, ASTM STP 459.

8. A. E. Carden, Private communication.

9. S. S. Manson, G. R. Halford, and M. H. Hirshberg, "Creep-Fatigue Analysis by Strain Partitioning," NASA TMX-67838, May 1971.

10. G. R. Halford, M. H. Hirshberg, and S. S. Manson, "Temperature Effects on the Partitioned Strain-Range-Life Relationships for Creep-Fatigue Analysis," The 1972 Symposium on Fatigue at Elevated Temperature," Storrs, Connecticut, June 1972, In press.

11. S. S. Manson, "Fatigue at Elevated Temperature-Summizing Up," Summary Lecture, The 1972 Symposium on Fatigue at Elevated Temperatures," Storrs, Connecticut, June 1972, In press.

BELFOUR, A J
BELFOUR STULEN
13919 W BAY SHORE DR
TRAVERSE CITY, MI 49684

BOESCH, W
SPECIAL METALS
NEW HARTFORD, NY 13413

BOETTNER, R C
P&W AIRCRAFT
400 MAIN ST
E HARTFORD, CT 06108

BRINKMAN, DR C R
AEROJET NUCLEAR
BOX 1845
IDAHO FALLS, ID 83401

BROPHY, J
INTNL NICKEL
STERLING FOREST
SUFFERN, NY 10901

BUNTIN, W R
MAIL ZONE T 35
GENERAL DYNAMICS
BOX 748
FORT WORTH, TX 76101

CAMPBELL, R D
LIQUID METAL ENG CTR
BOX 1449
CANOGA PARK, CA 91304

CARDEN, A E
MET DEPT
UNIV OF CONN
STORRS, CT 06268

COFFIN, JR, DR L F
R&D CTR
G E
BOX 8
SCHENECTADY, NY 12301

COLES, A
M 88
G E
EVENDALE, OH 45125

CONRAD, DR HANS
HEAD, DEPT MET ENG
UNIV OF KENTUCKY
LEXINGTON, KY 40506

CONWAY, DR J B
MAR-TEST
45 NOYNER DRIVE
CINCINNATI, OH 45215

COOPER, R
ROCKETDYNE DIV
N AMER ROCKWELL
CANOGA PARK, CA 91304

CORE, J E
ATOMIC POWER EQUIP
G E
175 CURTNER AVE
SAN JOSE, CA 95125

DANEK, G J
CODE A 813
ANNAPOLIS DIV
NAVAL SHIP R&D
ANNAPOLIS, MD 21402

DIETER, DR G E
HEAD, DEPT OF MET ENG
DREXEL INST OF TECH
32ND & CHESTNUT ST
PHILADELPHIA, PA 19112

DUNN, R G
ALLOY STEEL DEV
CLIMAX MOLY
1270 AVE OF THE AMERICAS
NEW YORK, NY 10020

ELLIS, R
GULF GENERAL ATOMIC
BOX 608
SAN DIEGO, CA 92112

ESZTERGAR, E P
7993 PROSPECT PL
LA JOLLA, CA 92037

FINNIE, PROF I
COLLEGE OF ENG
UNIV OF CAL
BERKELEY , CA 94720

FORNEY, D M
STRENGTS & DYN
AFML
WPAFB, OH 45433

GOLDHOFF, DR R M
G E
55 NORTH AVE
SCHENECTADY, NY 12305

GRANT, PROF N J
MET DEPT
RM 8-307, M I T
CAMBRIDGE, MA 02139

GRIFFIN, DR D S
WESTINGHOUSE
BETTIS ATOMIC POWER LAB
BOX 79
WEST MIFFLIN, PA 15122

GROSSKREUTZ, DR J C
NBS

WASHINGTON, DC

HANCOCK, J R
MIDWEST RES INST
425 VOLKER BLVD
KANSAS CITY, MO 64110

HANINK, D K
MATLS LAB
ALLISON DIV
G M
INDIANAPOLIS, IN 46206

HELLER, R A
DEPT OF ENG MECH
VPI
BLACKSBURG, VA 24061

HOWES, DR M
METALS RES DIV
ITT RES INST
CHICAGO, IL 60616

HUNKELER, F J
REACTIVE METAL PROD
HOMET
555 BENSTON RD
WHITEHALL, MI 49461

JAHNKE, L P
BLDG 200
G E
BOX 15132
EVENDALE, OH 45215

JAKUB, M T
L 514
GULF GENERAL ATOMIC
BOX 608
SAN DIEGO, CA 92112

Mr E H Kemp 49-2
Composites Branch
NASA-Lewis Research Ctr
21000 Brookpark Rd
Cleveland, OH 44135

Dr H B Probst 49-2
Alloys Branch
NASA-Lewis Research Ctr
21000 Brookpark Rd
Cleveland, OH 44135

Mr W D Klopp 105-1
Refract Met & Corr Br
NASA-Lewis Research Ctr
21000 Brookpark Rd
Cleveland, OH 44135

Dr D A Spera 49-1
Fatigue Research Br
NASA-Lewis Research Ctr
21000 Brookpark Rd
Cleveland, OH 44135

Mr S S Manson 49-1
Chief, M&S Division
NASA-Lewis Research Ctr
21000 Brookpark Rd
Cleveland, OH 44135

Mr J S Weeton 49-2
Composites & Metallurgy
NASA-Lewis Research Ctr
21000 Brookpark Rd
Cleveland, OH 44135

Library - Acquisitions
Jet Propulsion Lab
4800 Oak Grove Dr
Pasadena, CA 91102

Library
NASA
Goddard Space Flight Ctr
Greenbelt, MD 20771

Library
NASA
Flight Research Ctr
P O Box 273
Edwards, CA 93523

Mr C C Deutsch / RW
NASA Headquarters
Washington, DC 20546

Mr N Rekos / RL
NASA Headquarters
Washington, DC 20546

Technology Utilization
NASA MS 3-19
Lewis Research Ctr
21000 Brookpark Rd
Cleveland, OH 44135

Report Control Office
NASA MS 5-5
Lewis Research Ctr
21000 Brookpark Rd
Cleveland, OH 44135

Patent Council
NASA MS 500-311
Lewis Research Ctr
21000 Brookpark Rd
Cleveland, OH 44135

Library (2)
NASA MS 60-3
Lewis Research Ctr
21000 Brookpark Rd
Cleveland, OH 44135

Contracts Sect B
NASA MS 500-313
Lewis Research Ctr
21000 Brookpark Rd
Cleveland, OH 44135

Mr W F Brown 105-1
Fracture Branch
NASA-Lewis Research Ctr
21000 Brookpark Rd
Cleveland, OH 44135

Mr J C Freche 49-1
Assist Chief, M&S Div
NASA-Lewis Research Ctr
21000 Brookpark Rd
Cleveland, OH 44135

Mr S J Grisaffe 49-2
Surface Protection Br
NASA-Lewis Research Ctr
21000 Brookpark Rd
Cleveland, OH 44135

Mr R W Hall 105-1
Assist Chief, M&S Div
NASA-Lewis Research Ctr
21000 Brookpark Rd
Cleveland, OH 44135

WALL, F J
HIGH TEMP LAB
WESTINGHOUSE
LESTER P O
PHILADELPHIA, PA 19113

WEEKS, DICK
MATLS SCI DIV
ARGONNE NAT LAB
9700 SO CASS AVE
ARGONNE, IL 60439

WEI, B
RDT
U S AEC
WASHINGTON, DC 20545

WELLS, DR C H
P&W AIRCRAFT
ADV MATLS R&D LAB
MIDDLETOWN, CT 06458

CHIEF MS 49-1
Nuclear Systems Div
NASA-Lewis Research Ctr
21000 Brookpark Rd
Cleveland Oh 44135

WOODFORD, DR D A
MATL & PROCS LAB
55 NORTH AVE
G E
SCHENECTADY, NY 12305

ZAMRIK, PROF S
ENG MECH DEPT
PENN STATE UNIV
UNIVERSITY PARK, PA 18708

Nat Tech Info Ser (40)
Springfield, VA 22151

NASA Rep (2)
Sci & Tech Info Facility
Box 33
College Park, MD 20740

Defence Documentation Ctr
Cameron Station
5010 Duke St
Alexandria, VA 22314

MCIC
Battelle Memorial Inst
505 King Ave
Columbus, OH 43201

Tech Reports Library (3)
U S Atomic Energy Comm
Washington, DC

Tech Info Service (3)
U S Atomic Energy Comm
P O Box 62
Oak Ridge, TN

A J Nachtigall MS 49-1
Project Manager (3)
NASA-Lewis
21000 Brookpark Rd
Cleveland, OH 44135

Library
NASA
Marshall Space Flight Ctr
Huntsville, AL 35812

Tech Library JM6
NASA
Manned Spacecraft Ctr
Houston, TX 77058

JASKE, C
BMI
505 KING AVE
COLUMBUS, OH 43201

JOHNSON, R
MAIL DROP M87
G E
CINCINNATI, OH 45215

KENNEDY, DR C R
MET & CERAMICS DIV
ORNL
BOX X
OAK RIDGE, TN 37831

KOCKS, U F
MET DIV
ARGONNE NAT LAB
ARGONNE, IL 60439

KREMPL, E
DEPT OF MECHS
R P I
TROY, NY 12181

LAIRD, PROF C
SCHOOL OF MET & MET SCI
UNIV OF PENN
PHILADELPHIA, PA 19104

LIBERTINY, DR G Z
FORD MOTOR CO
20000 ROTUNDA
DEARBORN, MI 48121

LOHMEIR, AL
WESTINGHOUSE
BOX 19218
TAMPA, FL 33616

LUND, C
MARTIN METALS
250 NO 12TH ST
WHEELING, IL 60090

MCEVILY, PROF A J
MET DEPT
UNIV OF CONN
STORRS, CT 06268

MERCKX, K R
BLDG 326
HANFORD ATOMIC
G E
RICHLAND, WA 99352

MILLER, J
BLD 2-46
G E
1000 WESTERN AVE
WEST LYNN, MA 01905

MOEN, R A
WADCO
BOX 1970
RICHLAND, WA 99352

MORROW, PROF J
321 TALBOT LAB
UNIV OF ILL
URBANA, IL 61801

MOWBRAY, D F
BLDG 55-203
G E
SCHNECTADY, NY 12305

NIEH, L C S
RES & ENG CTR
UNITED NUCLEAR
GRASSLANDS RD
ELMSFORD, NY 10523

O'DONNELL, DR W J
O'DONNELL & ASSOC
3611 MAPLEVUE DR
BETHEL PARK, PA 15102

PARRY, G W
NUCLEAR SYS DIV
WESTINGHOUSE
BOX 355 FORREST HILLS STA
PITTSBURGH, PA 15230

POPP, H G
M 88
G E
BOX 15132
CINCINNATI, OH 45215

RICHARD, C E
AIRESEARCH
9851 SEPULVEDA
LOS ANGELES, CA 90045

ROSTOKER, DR W
MET DEPT
UNIV OF ILLINOIS
BOX 4348
CHICAGO, IL 60680

SANDOR, PROF B
COLLEGE OF ENG
UNIV OF WISC
MADISON, WI 53706

SEMCHYSHEN, DR M
CLIMAX MOLY
1600 HURON PARKWAY
ANN ARBOR, MI 48105

SHANK, DR M E
P&W AIRCRAFT
MIDDLETOWN, CT 06457

SHERBY, DR O D
DEPT OF MATLS SCI
STANFORD UNIV
STANFORD, CA 94305

SINCLAIR, PROF G M
321 TALBOT LAB
UNIV OF ILL
URBANA, IL 61801

STEPHENS, PROF R I
205 MECH ENG LAB
UNIV OF IOWA
IOWA CITY, IA 52240

SULLIVAN, C P
AMRDL
P&W AIRCRAFT
MIDDLETOWN, CT 06458

SWANSON, DR S R
MTS SYSTEMS
BOX 6112
MINNEAPOLIS, MN 55424

SWINDEMAN, R W
ORNL
BOX X
OAK RIDGE, TN 37831

TACKETT, J W
TECH DEPT
MATLS SYS DIV
CABOT CORP
KOKOMO, IN 46901

TAGART, S W
G E
NUCLEAR ENERGY DIV
175 CURTNER AVE
SAN JOSE, CA 92125

TOCIN, P R
WESTINGHOUSE
RES LABS
PITTSBURGH, PA 15235

TRAPP, W J
STR & DYN BR
AFML
WPAFB
OH 45433